Antenna Designs and Channel Modeling for Terahertz Wireless Communications

by

Zheng Xu
B.Sc., Jilin University, China, 2008
M.Sc., Beijing University of Posts and Telecommunications, China, 2011

A Dissertation Submitted in Partial Fulfillment of the
Requirements for the Degree of

DOCTOR OF PHILOSOPHY

in the Department of Electrical and Computer Engineering

University of Victoria

Antenna Designs and Channel Modeling for Terahertz Wireless Communications

by

Zheng Xu
B.Sc., Jilin University, China, 2008
M.Sc., Beijing University of Posts and Telecommunications, China, 2011

Supervisory Committee

Dr. Xiaodai Dong, Supervisor
(Department of Electrical and Computer Engineering)

Dr. Jens Bornemann, Co-Supervisor
(Department of Electrical and Computer Engineering)

Dr. Sudhakar Ganti, Outside Member
(Department of Computer Science)

Supervisory Committee

Dr. Xiaodai Dong, Supervisor
(Department of Electrical and Computer Engineering)

Dr. Jens Bornemann, Co-Supervisor
(Department of Electrical and Computer Engineering)

Dr. Sudhakar Ganti, Outside Member
(Department of Computer Science)

ABSTRACT

In this dissertation, channel modeling for Terahertz (THz) channels and designs of nano devices for THz communications are studied. THz communication becomes more and more important for future wireless communication systems that require an ultra high data rate, which motivates us to propose new nano device designs based on graphene and new system models for the THz channel. Besides, the multiple-input multiple-output (MIMO) antenna technique is well known to increase the spectral efficiency of a wireless communications system. Considering THz channels' particular characteristics, MIMO systems with reconfigurable antennas and distributed antennas are proposed. We compare the differences between MIMO systems in the GHz and THz bands, and highlight the benefits of using multi antennas in the THz band.

The work on nano device designs provides two antenna designs with single walled carbon nanotubes (SWCNTs) and graphene nano ribbon (GNR). First, we analyse the spectral efficiency of an SWCNT bundled dipole antenna based MIMO system in the Terahertz band. Two scenarios are considered: the large scale MIMO and the conventional scale MIMO. It is found that, in order to get the maximum spectral efficiency, the CNT bundle size should be optimized to obtain a tradeoff between the antenna efficiency and the number of antennas for a given area. We also discuss the random fluctuation in the bundle size during the CNT bundled antenna fabrication which reduces the system spectral efficiency. Then, we propose reconfigurable directional antennas for THz communications. The beamwidth and direction can be controlled by the states of each graphene patch in the antenna, and the states can be easily configured by changing the electrostatic bias voltage on each element.

The work on reconfigurable MIMO system proposes a new antenna array design for MIMO in the THz band. First, the path loss and reflection models of the THz channel are discussed. Then, we combine the graphene-based antenna and the THz channel model and propose a new MIMO antenna design. The radiation directions of the transmit antennas can be programmed dynamically, leading to different channel state matrices. Finally, the path loss and the channel capacity are numerically calculated and compared with those of the GHz channel. The results show that for short range communications, the proposed MIMO antenna design can enlarge the channel capacity by both increasing the number of antennas and choosing the best channel state matrices.

The work on MIMO channels proposes a statistical model for the MIMO channel with rough reflection surfaces in the THz Band. First, our analysis of scattering from a rough surface indicates that the reflection from a single surface can be a cluster of rays. Secondly, a new MIMO model for THz communications is proposed. In this model, the number of multipaths is highly dependent on the roughness of the reflecting surfaces. When the surface is ideally smooth, the MIMO channel is sparse and as a result, the capacity is sub-linear with the MIMO scale. On the other hand, when the surface is rough, more degrees of freedom are provided by the scattered rays. Finally, channel capacities with different surface roughness are numerically calculated and compared between different MIMO scales. The results show that in contrast to the GHz range, large scale THz multiple antennas may not provide as much multiplexing gain. Therefore, it is necessary to determine the antenna scale according to the actual propagation environment.

The work on distributed antenna systems (DAS) proposes a new DAS model in the THz band. First, the model of DAS in the THz frequency is discussed, which has fewer multipaths than that in the GHz band. Then, we analyze the characteristics of the DAS model and point out that the channel is very sparse if the number of antennas on the base station (BS) is very large. Besides, we provide reasons for the fact that DAS can have a large number of degrees of freedom. We compare the capacities of MIMO systems with DAS and without DAS. The results show that for THz channels, increasing the number of antenna units (AUs) is much more important than increasing the number of antennas in one AU. Finally, we propose an antenna selection and precoding scheme which has very low complexity.

Contents

List of Tables

List of Figures

Notations

Unless stated otherwise, boldface upper-case and lower-case letters denote matrices and vectors respectively.

$\mathbf{X}^*$	the conjugate of matrix $\mathbf{X}$
$\mathbf{X}^{\mathrm{T}}$	the transpose of matrix $\mathbf{X}$
$\mathbf{X}^{\mathrm{H}}$	the conjugate transpose (Hermitian) of matrix $\mathbf{X}$
$\mathbf{I}_M$	the identity matrix of dimension $M \times M$
$\mathbf{0}$	a zero vector or matrix
$\lvert x \rvert$	the absolute value of a real scalar x or magnitude of a complex scalar x
$\mathrm{E}\left[\cdot\right]$	the expectation operator
$\mathrm{Var}\left[\cdot\right]$	the variance operator
$\mathbb{R}$	the real number set
$\mathbb{C}$	the complex number set
$\mathbb{C}^m$	a set of complex column vectors with size m
$\mathbb{C}^{m\times n}$	a set of complex matrices with size $m \times n$
$\sim$	distributed according to
$\mathcal{CN}(\mathbf{m}, \mathbf{\Sigma})$	complex Gaussian distribution with mean $\mathbf{m}$ and covariance matrix $\mathbf{\Sigma}$
$\triangle$	distance normalized to wavelength
max	maximize
min	minimize

ACKNOWLEDGEMENTS

First of all, I would like to express my greatest appreciation to my supervisors, Prof. Xiaodai Dong and Prof. Jens Bornemann, for their continuous support of my Ph.D study and research. I am grateful for their patient guidance, inspired instructions and thesis revision every time, and providing me with an excellent research atmosphere. Without their guidance and persistent help this dissertation would not have been possible.

I would like to thank my committee member, Prof. Sudhakar Ganti, for his meticulous guidance, suggestions and advice on improving the quality of this dissertation.

I would like to thank Prof. Tao Lu, for his insightful suggestions on my papers, especially on antenna designs, but also for the comments which caused me to widen my research from various perspectives.

I thank my fellow classmates in the whole laboratory: Binyan Zhao, Leyuan Pan, Yongyu Dai, Guang Zeng, Ming Lei, Yi Shi, Ping Cheng, Biao Yu, Tong Xue, Youjun Fan, Yunlong Shao, Lan Xu, Le Liang, Congzhi Liu, Weiheng Ni, Yiming Huo, Farnoosh Talaei, Jun Zhou, Hongrui Wang, Yuejiao Hui, Guowei Zhang, Wanbo Li, Tianyang Li, for the research discussions and for all the fun we had in the last several years.

Last but not least, I would like to express my endless gratitude to my wife, Lei Jing, for her unconditional support, help, patience, sacrifices and love. She stands by me through the good times and the bad. And my parents, who are always supporting me and encouraging me through my whole life.

Zheng Xu, Victoria, BC, Canada

DEDICATION

To my parents,
My wife,
And all my friends,
For everything.

Chapter 1

Overview

1.1 Research Areas Overview

In order to meet the demand of ultra high data rate, the only promising way is to shift the carrier frequencies to the Terahertz (THz) band. Large amounts of idle spectrum ranging from 0.1 THz to 10 THz with wavelengths of 30-3000 μm are available. For such high frequencies, new devices are needed to adapt to the THz channel. This research is focused on the design of new devices for THz wireless communications as well as modeling the THz channel. Graphene, as one of the most novel materials suitable for THz communications, has attracted tremendous interest since it was first isolated in 2004. We will first analyse the properties of graphene and, with its particular characteristics, new receiver and antenna designs will be proposed. Then the THz channel will be modeled and compared with those of the Gigahertz (GHz) channel. The combination of the graphene-based devices and the new channel model will be studied. Finally, we will apply the graphene-based devices to massive multiple-input multiple-output (MIMO) which is supposed to be one of the key techniques in the 5G standard.

1.1.1 Graphene and Graphene-based Devices

Graphene and its derivatives, such as carbon nanotube (CNT) and graphene nanoribbon (GNR), have attracted tremendous interest in manufacturing novel nano devices due to their exceptional mechanical and electrical properties. Based on the graphene's unique properties, we propose two antenna designs for wireless communications. The first antenna design is based on single walled CNTs (SWCNTs) and bundled SWCNTs. The efficiency and size of the antenna are controlled by the number of SWCNTs in the bundle, and there is a tradeoff between size and efficiency. The second antenna design is based on GNR. As the resistivity of graphene decreases rapidly with the increase of the electrostatic bias voltage, the states of the graphene can be easily controlled. This motivates us to propose a reconfigurable antenna array with variable radiation patterns [6, 7]. In another aspect, graphene's other electric properties can also be used for wireless communications. Graphene is an extremely low noise material with high conductivity, which makes it suitable for molecule sensing. We design a graphene based gas sensor which has a very high sensitivity. We propose a simple and efficient detection method for the molecule communications based on this sensor, which can not only enlarge the communication range, but also has low complexity.

1.1.2 Terahertz Channel Model and Reconfigurable MIMO System

When the frequency is in the THz regime, the channel model is different from that of the GHz range. On one hand, a signal in the THz band suffers both spreading loss and molecular absorption loss, which is different from that in the GHz band in which molecular absorption loss can be ignored. On the other hand, the reflection properties in the THz range are also different from those in the GHz band. For objects (e.g., plaster or wallpaper) in indoor environments, the surface variations are on the order of several hundred microns to millimeters [5, 8], which are comparable to the THz wavelength λ (e.g., the wavelength at 1 THz is 300 μm). Therefore, the surfaces of indoor objects, which can be regarded as smooth surfaces at the GHz frequency, are now rough surfaces at the THz frequency. These differences motivate us to explore new channel models for THz channels.

The multiple-input multiple-output (MIMO) antenna technique is well known to increase the spectral efficiency of a wireless communications system [9]. If the transmit antennas can be distinguished by each receive antenna, then multiple data streams can be transmitted within the same time and frequency resources. In order to increase the spectral efficiency of a MIMO system, the number of degrees of freedom of the MIMO channel can be enlarged. If the amount of scattering and reflections in the multi-path environment is large enough, then more transmit and receive antennas result in more data streams and higher spectral efficiency. However, for real MIMO systems with limited area, the antenna size and antenna separation are the main obstacles to increasing the MIMO scale, which is difficult to solve when using traditional omnidirectional antennas. This motivates us to propose graphene-based directional antennas which can decrease the antenna size and reduce the antenna separation.

For THz MIMO systems, the GHz MIMO models are not suitable for several reasons. One is that in the GHz model, they assume all the reflections are specular reflections without considering the reflection loss. The other is that it is assumed that there are many multipaths in the environment, so that each fading factor is a Rayleigh variable. However, at the THz frequency, if the surface is rough, the scattering reflections are too large to be ignored. If the surface is smooth, then there will be very few multipaths. The channel may be divided into two parts, one is due to the specular multipaths, and the other is due to the scattering multipaths. This motivates us to study the model of the THz MIMO system with rough surfaces.

1.1.3 MIMO Channel with Rough Reflection Surfaces in the THz Band

In a GHz channel, it is usually assumed that the elements of a fading channel matrix $\mathbf{H}$ are independent and identically distributed (i.i.d.), which is based on the assumption of a rich scattering environment that has many multipaths. Under this assumption, the physical channel can be viewed as several parallel sub-channels, and the total capacity scales up linearly with the MIMO dimension. However, for some scenarios in the THz channel and with increasing MIMO dimension, MIMO systems show only beamforming gain but limited multiplexing gain improvement. This is due to the fact that the number of multipaths in the THz channel is limited since the path loss and reflection loss are so large that only the single bounce reflection rays are strong enough to link transmitters with receivers. Therefore, the models of the GHz channel cannot directly be applied to the THz channel, and new models for THz MIMO systems must be developed. It is generally agreed that THz MIMO systems have the following characteristics: i) The scenarios are mainly applied to indoor environments, for example, office buildings or malls [10]. For long distance outdoor communications, smart antennas with high power amplifiers must be applied [11]; ii) For indoor THz MIMO channels, few multipaths exist between the transmitting and receiving antennas if all the surfaces are smooth [12, 13]. The correlations between the received signals on different receive antennas are significantly higher than those in the GHz band. Therefore, the multiplexing gain will be low, and correlated signals have low diversity gain. This situation is very similar to the sparse MIMO channel that has been studied in some theoretical investigations [14, 15] as well as in experiments [16].

Most of the existing works on MIMO system models are in the GHz band or millimeter wave band, but very few papers study MIMO systems in the THz (frequencies higher than 300 GHz) band. Therefore, in this part, we study MIMO channel modeling for THz communications. Besides the different path loss factors, surface roughness is one of the most important differences between THz and GHz MIMO channels. For THz MIMO models, scattering analysis is far more important than in the GHz range. In [4, 5, 8, 11–13], the scattering from rough surfaces is studied for THz channels. When the carrier frequency is very high, the surfaces of reflecting objects can no longer be regarded as smooth. For THz frequencies, the surfaces of indoor objects, such as wallpaper or carpet, are all sufficiently rough such that their scattering cannot be ignored. The authors of [8, 12] studied the scattering power from different reflection angles at 300 GHz and measured the multipath loss in an indoor scenario. We use the same method to investigate the reflection properties of THz frequencies and derive a new MIMO model for indoor nanocommunications. In this new model, the scattered rays are included and become increasingly important with rising frequency. When the frequency is high enough, the specular reflection is less dominant and becomes an ordinary ray with very low power gain. In our capacity analysis, we express the channel capacity as the sum of two parts, one is the capacity introduced by specular reflection, the other one is introduced by scattered rays. Since the specular reflection rays are weak in the THz band, the capacity is mainly contributed by scattered rays. Another very important difference between THz MIMO and GHz MIMO systems is that the antenna size is much smaller in the THz regime and, therefore, we can place hundreds of antennas on a single device, which necessitates the performance analysis of very large scale antenna arrays.

1.1.4 Distributed Antenna System Model in the THz Band

To relieve the high path loss problem and increase the channel capacity, and with an aim of covering the dead spots in indoor wireless communication systems, we propose a distributed antenna systems (DAS) model in the THz band. In this part, we analyze the performance of DAS in the THz band for indoor communications. For the GHz DAS, the traditional channel models all include a large scale fading model and a Rayleigh fading model. However, this is not the case in the THz channel. As the number of multipaths is very limited in the THz band, we cannot simply assume that the small scale fading is a Rayleigh distribution. We fully consider the number of multipaths and propose a model suitable for THz DAS.

DAS in the THz band has fewer multipaths than in the GHz band. Therefore, the characteristics of the DAS channel are quite different from those in the GHz band. The channel is very sparse if the number of antennas on the base station (BS) is very large. We compare the capacity of MIMO systems with DAS and without DAS. The results show that for THz channels, increasing the number of antenna units (AUs) is much more important that increasing the number of antennas in one AU. Besides, we propose an antenna selection and precoding scheme which has very low complexity.

1.2 Organization

In Chapter 2, some graphene-based nano devices are proposed and their performances are analysed. Chapter 3 discusses the characteristics of the THz channel and proposes a new channel model considering both molecular absorption loss and rough surface reflections. A new directional antenna-based MIMO system model is also proposed in this chapter. In Chapter 4, we propose a statistical model for the MIMO channel with rough reflection surfaces in the THz Band. We reveal when it is necessary to use a large MIMO scale in the THz band. In Chapter 5, a new distributed antenna system model in the THz is proposed. Finally, the research contributions on each topic are concluded in Chapter 6.

Chapter 2

Graphene-based Devices

2.1 Introduction

Graphene has attracted much interest since it was first isolated from High Ordered Pyrolytic Graphite (HOPG) in 2004 [17]. It is a true two dimensional material with a single planar atomic layer of carbon atoms. Many devices are rebuilt using graphene based on its unique electric properties. For example, for field effect transistors [18] and interconnects [19], high speed is achieved due to the special energy band structure and ultrahigh electron mobility in graphene [20, 21]. Chemical detectors with exceptional sensitivity are produced due to the fact that graphene is electronically an ultra low noise material [22]. Another promising research topic is graphene-based nano-antennas [6, 23–25]. Compared with metallic antennas, the graphene-based nano-patch antennas have many new characteristics which are more suitable for nano devices and THz communications.

The slow wave propagation along SWCNTs can reduce the size of an antenna significantly [24, 26]. Compared with classical metallic antennas, the SWCNT antenna is more suitable for nano communications as its size is about one hundred times smaller. Burke *et. al.* made some quantitative assessments of SWCNT's performance potential [27, 28]. It is pointed out that the SWCNT has conductivity several times larger than copper but has a very high resistance because of its small diameter. Due to the high resistance, the radiation efficiency of a SWCNT antenna is extremely low, which hampers its practical use. One approach to solve the resistance problem is to bind several SWCNTs as a bundle. Reference [1] studies the electrical properties of bundled CNTs, and [29] gives the performance prediction of SWCNT bundled dipole antennas. They showed that the antenna efficiency can increase 30-40 dB when the bundle size is several hundreds. Besides, as the resistivity of graphene decreases rapidly with the increase of the electrostatic bias voltage, the states of the graphene-based antennas can be controlled. Thus, a reconfigurable antenna array with variable radiation patterns is obtained based on this characteristic [6, 7].

2.2 Related Work

K. S Novoselov *et. al.* published the first paper about graphene in 2004 [17]. They use a very simple method (mechanical exfoliation of small mesas of highly oriented pyrolytic graphite) to prepare few layer graphene films up to 10 μm in size. G. W. Hanson investigates fundamental properties of dipole transmitting antennas formed by carbon nanotubes [30]. He suggests the possibility of using carbon nanotubes as antennas by analyzing the input impedance, current profile, efficiency and radiation pattern. References [6, 23–25] study graphene-based nano-antennas. Compared with metallic antennas, the graphene-based nano-patch antennas have a smaller size because of the slow wave property [24, 26] and also resonate with a higher radiation efficiency due to the higher electron mobility in a nano scale structure [25]. Besides, a reconfigurable antenna array with variable radiation patterns is obtained based on this characteristic [6, 7]. For molecular communications (MC), references [31, 32] model the physical channel and references [33, 34] analyze the channel capacity of MC, while others study the modulation and detection schemes [35].

2.3 Contributions

Most of the existing works investigate the properties and performance of SWCNTs as single dipole antennas. However, the performance of MIMO networks based on SWCNT antennas has not been well studied yet. For SWCNT antennas, the efficiency of antennas and the number of antennas in a given receiving array area are controlled by the SWCNT bundle size. There exists an optimal bundle size that makes the spectral efficiency largest.

For THz communications, new antenna designs are needed to adapt to the THz channel. Reference [36] studies the THz emission from interdigitated finger photomixers coupled to planar antenna structures and reveals that the performance can be improved by independently optimizing the photomixer and antenna. Georgiou et. al. have recently demonstrated experimentally a full all-optical generation of linear antennas at THz frequencies, indicating the possibility of inducing resonant phenomena by the structured illumination of a flat surface [37]. However, both of these antennas are not suitable for building reconfigurable directional antennas. Besides, for nano-devices, such as nano-sensors and nano-on-chip systems [10, 38], the space is limited and the sizes of the above antennas are too large (i.e., the size of the antenna in [37] is about several millimeters). As graphene has the aforementioned novel properties, it can satisfy our requirements in manufacturing reconfigurable directional antennas for THz communications.

Based on the aforementioned motivations, we analyze the relationship between the antenna efficiency and the SWCNT bundle size. In the following part of this chapter, we propose a Yagi-Uda antenna design based on an array of graphene patches, and analyse the radiation patterns of these directional antennas, which can be easily configured by changing the electrostatic bias voltage on each element. In the third part of this chapter, we propose a model for MC with graphene-based receivers. First, the characteristics of the graphene is analyzed. Then, we study the diffusion model of the MC system. Finally, as the MC model can be treated as an equivalent electromagnetic communication model with a different channel transfer function, we analyze the detection scheme and performance with methods similar to those of electromagnetic systems.

2.4 The SWCNT-based Dipole Antenna

2.4.1 Characteristics of SWCNT and SWCNT-based Antennas

SWCNT can be considered as a rolled up tube made of a graphene sheet which is formed by single layer carbon atoms. A circuit model of a SWCNT is shown in Fig. 2.1(a) [1, 27].

Ignoring the resistance due to impurities and defects, the intrinsic resistance of one SWCNT is given by [28]

$$R_{cnt} = \frac{h}{4e^2}\frac{L}{l_{mfp}}, \tag{2.1}$$

where L is the length of the SWCNT, h is Planck's constant, e is the electron charge and l_{mfp} is the mean free path in the SWCNT. R_c in Fig. 2.1(a) is the SWCNT contact resistance which can be ignored when L is large. Many experiments show that it is reasonable to take $l_{mfp} = 1$ μm and $R_{cnt} = 6$ kΩ/μm [28]. As shown in previous work [39], the quantum capacitance is $C_Q = 100$ aF$/\mu$m, the electrostatic capacitance C_E is in the same order as C_Q, and the kinetic inductance is $L_k = 16$ nH$/\mu$m. In this work, we mainly focus on very narrow SWCNTs which have four parallel channels: two spin-up channels and two spin-down channels. As

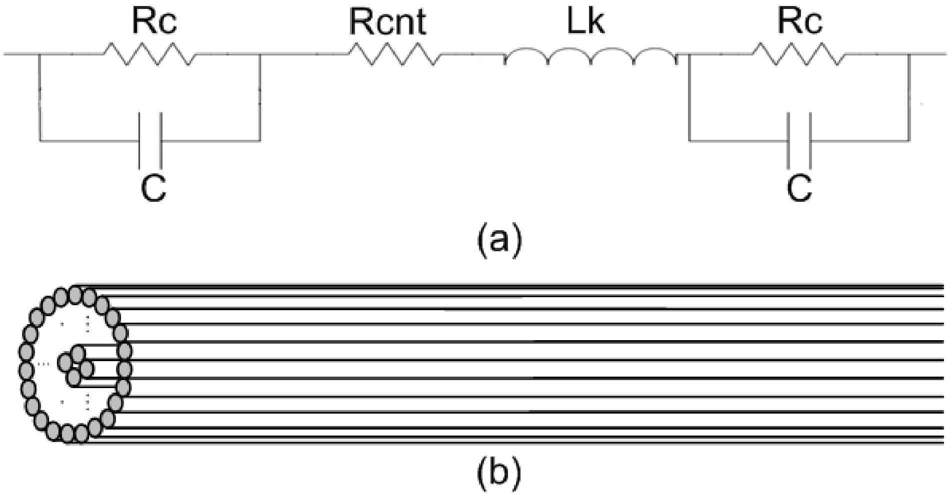

Figure 2.1: (a) Circuit model of one SWCNT [1]. (b) Several SWCNTs bound together as a bundle.

the diameter of a SWCNT increases, the number of channels increases, and hence the performance study of thick SWCNTs needs to take into account the diameter of the SWCNT. For a very narrow SWCNT, the total capacitance C is given by $C^{-1} = C_E^{-1} + 4C_Q^{-1}$. The wave propagation speed in an SWCNT is

$$v_s = \frac{1}{\sqrt{\frac{L_k C}{4} + \sqrt{\frac{L_k^2 C^2}{16} + \frac{C^2 R_{cnt}^2}{(2\pi f)^2}}}}, \tag{2.2}$$

where f stands for the wave frequency. When the frequency is high enough (i.e. 1 THz), v_s can be approximated as

$$v_s \approx \sqrt{2/(L_k C)}. \tag{2.3}$$

With the L_k and C values given above, $v_s = 1.26 \times 10^6$ m/s, which is much smaller than the speed of light in free space. Due to the low transmission speed, the wave number $k_p = 2\pi/\lambda_p = 2\pi f/v_s$ on SWCNT antennas is much larger than that of conventional metallic antennas of the same frequency, where λ_p is the wavelength of the current distribution on a SWCNT. This makes the radiation resistance of SWCNT dipole antennas quite low [27]

$$R_r = (k_0/k_p)^2 \eta \beta(k_p, L_a), \tag{2.4}$$

where k_0 is the wave number in free space, $\eta = 120\pi$ is the impedance of free space and function $\beta(k_p, L_a)$ is defined as

$$\beta(k_p, L_a) = \frac{1}{2\pi}\int_0^{\pi} \sin^3\theta [\frac{\cos(\frac{k_0 L_a}{2}\cos\theta) - \cos(\frac{k_p L_a}{2})}{1-(k_0/k_p)^2\cos^2\theta}]^2 d\theta, \tag{2.5}$$

where L_a is the length of antennas and θ is the radiation direction. For $L_a = \lambda_p$, the resistance is about $5.7 \times 10^{-3}\ \Omega$. As a consequence, the radiation efficiency can be below -60 dB [27]. The radiation efficiency is expressed as

$$\xi = P_r/(P_r + P_o) = R_r/(R_r + R_o), \tag{2.6}$$

where P_o is the ohmic loss power, P_r is the radiation power and $R_o = R_{cnt}$ is the ohmic resistance. Such low efficiency limits the use of SWCNTs as antennas. One way to solve this problem is to bind several SWCNTs into a bundle. By doing this, the propagation speed v_s increases while the ohmic resistance decreases. Reference [1] describes the properties of individual and bundled SWCNTs. Their measurements show that the impedance of the bundled SWCNT scales with the number of SWCNTs in the bundle. Reference [29] predicts the performance of SWCNT bundled dipole antennas as follows. Using the structure shown in Fig. 2.1(b), the resistance R_{cnt}^N and kinetic inductance L_k^N can be scaled down by the number of SWCNTs in the bundle while the capacitance C remains unchanged [29]. At a high frequency (THz), R_{cnt}^N, L_k^N , k_p^N and λ_p^N can be written as $R_{cnt}^N \approx R_{cnt}/N$, $L_k^N \approx L_k/N$, $k_p^N \approx \sqrt{(2\pi f)^2 L_k C/2N}$ and $\lambda_p^N = 2\pi/k_p^N$, respectively, where N is the number of SWCNTs in a bundle.

From (2.4), we can see that a small k_p^N leads to large radiation resistance. As a result, the radiation efficiency is improved. The efficiency of a bundled antenna with N SWCNTs is given by

$$\xi(N, L_a) = \frac{N^2}{N^2 + B(N, L_a)}, \tag{2.7}$$

where $B(N, L_a) = \frac{2R_{cnt}\pi^2 f^2 L_k C}{k_0^2 \eta \beta(k_p^N, L_a)}$. As shown in [27], for a fixed N, when $L_a = \lambda_p^N$, the antenna efficiency is the highest. Compared with single SWCNT dipole antennas, the simulation results in [29] show that the efficiency of a bundled antenna can increase about 30-40 dB when the bundle size is 400.

In real fabrication, by changing the catalyst particle size and the growth time, we can control the diameter and the length of SWCNTs, yet it is a challenge to control the bundle size [40]. Denote $\overline{N}$ as the target bundle size, then the real bundle size N obeys truncated normal distribution with the probability density

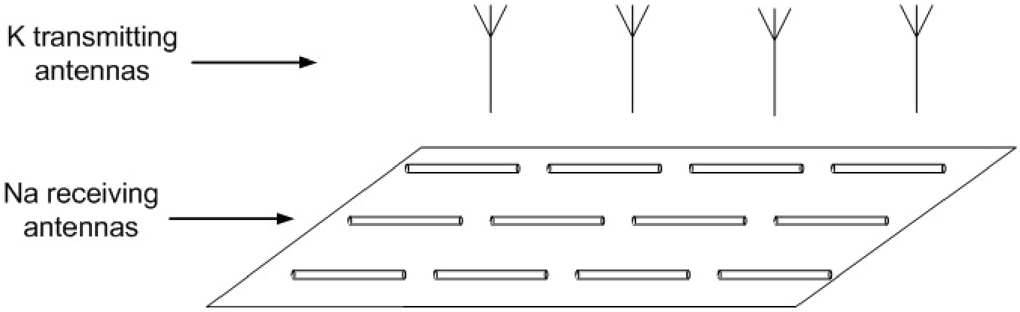

Figure 2.2: MIMO system based on SWCNT bundled antennas. There are N_a SWCNT bundled antennas using as receiving antennas and K transmitting antennas around the array.

function

$$\Phi(N) = \frac{1}{\sqrt{(2\pi)}\sigma} e^{-\frac{(N-\overline{N})^2}{2\sigma^2}} \qquad N \geq 1, \tag{2.8}$$

where σ^2 is the variance of N.

2.4.2 MIMO Models with the SWCNT-based Antennas

In our model, we use bundled SWCNTs to fabricate receiving dipole antennas. We set the length of the antenna as the full wavelength which has the highest efficiency [27]. The area effectively occupied by each antenna is denoted by A, where approximately $A \propto L_a^2$. For a fixed area S, the maximum number of antennas is $N_a(\overline{N}) = S/A$. Assume that there are K ideal transmitting antennas in this system, where K is on the order of several tens. Thus, we can model the MIMO system based on SWCNT bundled antennas as shown in Fig. 2.2. For classical metallic dipole antennas, the spectral efficiency depends on signal-to-noise ratio (SNR) and $N_a(\overline{N})$. Antenna efficiency is seldom considered since the ohmic resistance of a metallic antenna is much smaller than its radiation resistance and the efficiency of the antenna is almost unity. However, this is not true for SWCNT antennas as the antenna efficiency is much lower than unity. Besides SNR and $N_a(\overline{N})$, antenna efficiency must also be considered when calculating the spectral efficiency of SWCNT antenna systems. From (2.4) and (2.7), we can find that increasing the bundle size $\overline{N}$ improves the efficiency of a bundled antenna and hence enhances the spectral efficiency of the system. On the other hand, when $\overline{N}$ increases, $k_p^{\overline{N}}$ drops gradually leading to the rise of $\lambda_p^{\overline{N}}$. As a result, each bundled antenna length is larger and the number of antennas that can be placed in the area S is reduced, which has a negative effect on the spectral efficiency of the system. Therefore, there is a tradeoff between $N_a(\overline{N})$ and the efficiency of antennas. Next we analyse the model in two scenarios in detail.

a) Large scale MIMO: the array size is relatively large, and the number of antennas $N_a(\overline{N})$ goes up to hundreds or even thousands. Usually K is much less than $N_a(\overline{N})$. As the surfaces of the objects in the propagation environment are relatively rough compared to the wavelength in THz, this effect leads to many multi-path components. Thus, in this study we assume a Rayleigh fading channel, and the components of the channel matrix $\mathbf{H}$ are independent, identically distributed with zero mean and unit variance [41], although this has not been verified by any measurements to date. When using a zero-forcing (ZF) receiver to detect symbols, the pseudo inverse of $\mathbf{H}$ is needed. However, it is not easy to get the pseudo inverse of $\mathbf{H}$ with large size directly. Fortunately, from the Law of Large Numbers, we know that the effect of small-scale fading can be averaged out by increasing the number of receiving antennas [41]. From the receiver's perspective, we can simply use the transpose of the matrix instead of its inverse since it is almost true that $\mathbf{H}^T\mathbf{H} = \mathbf{I}$ for large size $\mathbf{H}$. The uplink spectral efficiency of the system is lower bounded by

$$R = \sum_{k=1}^{K} \log_2(1 + SNR_k \cdot \xi(\overline{N}, \lambda_p^{\overline{N}}) \cdot (N_a(\overline{N}) - K)), \tag{2.9}$$

where SNR_k is the nominal received SNR of the kth user when ideal antennas are used. For this scenario, there exists an optimal $\overline{N}$ that maximizes R given a fixed array area S. In real fabrication, the real bundle size N is not guaranteed to be identical with the target bundle size $\overline{N}$ which makes the $\xi(N, \lambda_p^{\overline{N}})$ lower. The expected spectral efficiency can be expressed as

$$R{=}\sum_{k=1}^{K} \int_1^{\infty} \log_2(1{+}SNR_k \cdot \xi(N, \lambda_p^{\overline{N}}) \cdot (N_a(\overline{N}){-}K)) \cdot \Phi(N) dN. \tag{2.10}$$

For the THz channel, SNR is affected by transmitting power, spreading and reflection loss, molecular absorption noise, antenna electronic noise and any other additional noise [42]. For SWCNT antennas, however, there are no clear models for the electronic noise at Terahertz frequencies. Hence, the realistic values of SNR still remain uncertain.

b) Conventional scale MIMO: the array size is small, and the number of antennas is only several tens. Since the size of $\mathbf{H}$ is not large, it is reasonable to use conventional receivers to detect symbols. When all K users have the same transmitting power, the largest uplink spectral efficiency is achieved for $K \geq N_a(\overline{N})$

as

$$\begin{aligned} R &= \mathbb{E}_\lambda[\sum_{m=1}^{N_a(\overline{N})} \log_2(1+SNR\cdot\xi(\overline{N},\lambda_p^{\overline{N}})\cdot\lambda_m^2)] \\ &\leq N_a(\overline{N})\log_2(1+SNR\cdot\xi(\overline{N},\lambda_p^{\overline{N}})\cdot\mathbb{E}_\lambda[\lambda_m^2]), \end{aligned} \tag{2.11}$$

where $\mathbb{E}_\lambda[\cdot]$ is the expectation over λ_m and $\lambda_1, \lambda_2, \cdots, \lambda_{N_a}$ are the singular values of the channel matrix $\mathbf{H}$, and SNR is the common SNR at each receive antenna. Since the MIMO channel can be treated as $N_a(\overline{N})$ single-input single-output (SISO) channels [9], the uplink rate increases as $N_a(\overline{N})$ increases and it decreases as $\xi(N, \lambda_p^{\overline{N}})$ decreases. For this case, there also exists an optimal $\overline{N}$ that maximizes R given a fixed array area S. In this scenario, the spectral efficiency with fabrication variations is modified to

$$\begin{aligned} R &= \mathbb{E}_\lambda[\sum_{m=1}^{N_a(\overline{N})}\int_1^\infty \log_2(1+SNR\cdot\xi(N,\lambda_p^{\overline{N}})\cdot\lambda_m^2)\cdot\Phi(N)dN] \\ &\leq N_a(\overline{N})\int_1^\infty \log_2(1+\overline{SNR}\cdot\xi(N,\lambda_p^{\overline{N}}))\cdot\Phi(N)dN, \end{aligned} \tag{2.12}$$

where $\overline{SNR} = SNR\cdot\mathbb{E}_\lambda[\lambda_m^2]$.

2.4.3 Performance Analysis

We consider the system working at frequency $f = 2.6$ THz which is one of the THz transmission windows, and in all results, the radius of one SWCNT is 0.339 nm. By numerical calculation, the length of SWCNT bundled full wavelength dipole antennas with respect to $\overline{N}$ is shown in Fig. 2.3(a). For example, when N is 2000, the optimal antenna length is about 20 μm and and the radius of the antenna is 15 nm. At the same frequency, the length of a perfect copper half wavelength dipole antenna is about 60 μm. This indicates that we can implement 9 times the number of antennas in the same area if we use SWCNT bundled antennas instead of copper antennas. In Fig. 2.3(b), the curve shows the number of antennas in an array $N_a(\overline{N})$ versus $\overline{N}$. As can be seen, $N_a(\overline{N})$ decreases when the SWCNTs bundle size gets larger. The relationship between efficiency and SWCNT bundle size is shown in Fig. 2.3(c). It can be seen from (2.7) that when $\overline{N}^2$ is much smaller than $B(N, L_a)$, it is roughly true that the efficiency $\xi(\overline{N}, \lambda_p^{\overline{N}})$ increases linearly with $\overline{N}^2$. As shown in Fig. 2.3(c), when $\overline{N}$ is 400, the efficiency is 38.8 dB higher than that of the SWCNT antennas which coincides with the results in [29]. When $\overline{N}$ increases to 2000, the efficiency reaches about 0.3, which is only 5.2 dB lower than an ideal

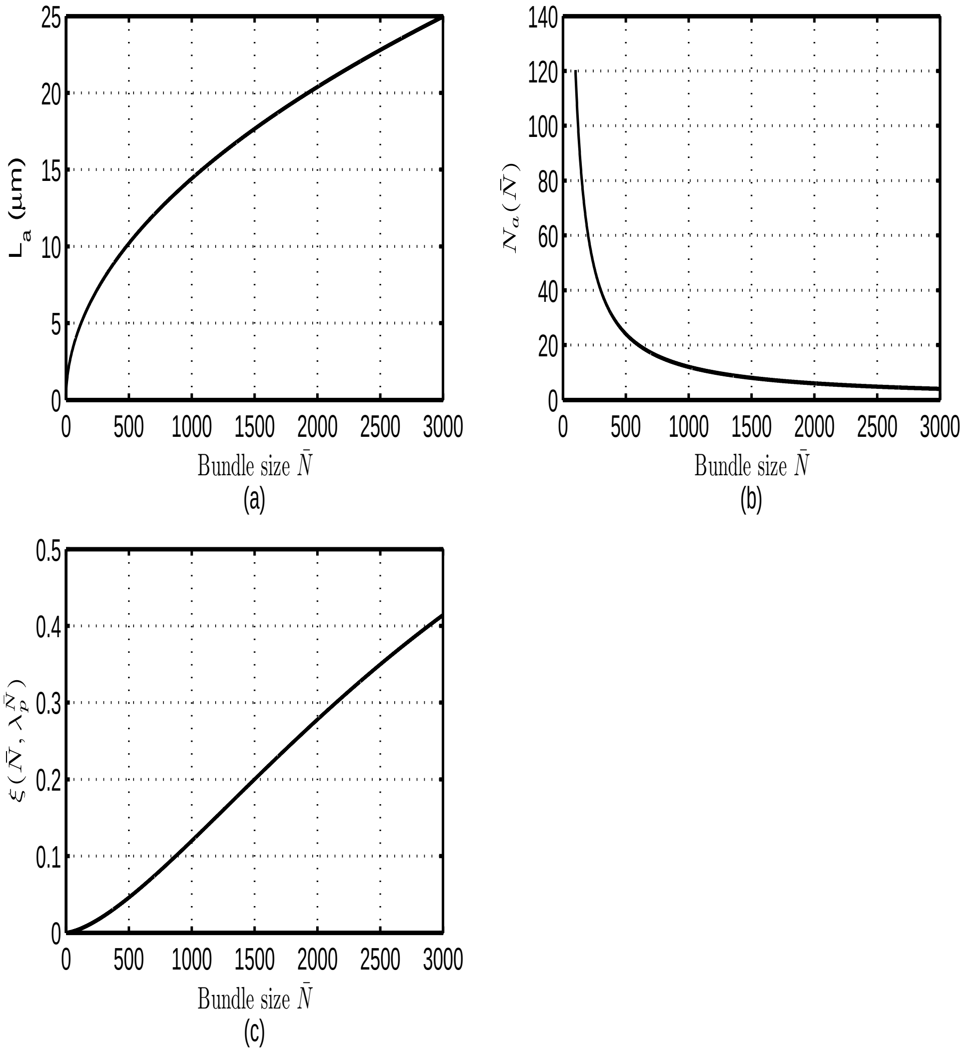

Figure 2.3: (a) The length of antennas L_a. (b) The number of antennas $N_a(\overline{N})$. (c) The efficiency of antennas $\xi(\overline{N}, \lambda_p^{\overline{N}})$. The array size $S = 1 \times 10^{-8}$ m^2, and $f = 2.6$ THz.

antenna. As shown in Fig. 2.3(b) and (c), we cannot increase the efficiency and the number of antennas simultaneously. Moreover, [30] gives the efficiency of copper dipole antennas with different diameters. By comparison, the efficiency of SWCNT bundled dipole antennas is more than 10 dB higher than that of copper dipole antennas of the same diameter. When the diameter gets smaller, the advantage of efficiency by using SWCNT bundled antennas becomes even larger. For copper antennas of the same length of SWCNT bundled antennas, the resonant frequency will be much higher than 2.6 THz.

In Fig. 2.4, the solid line shows the spectral efficiency of the large scale MIMO system for different $\overline{N}$. We set the number of transmitting antennas $K = 20$, and

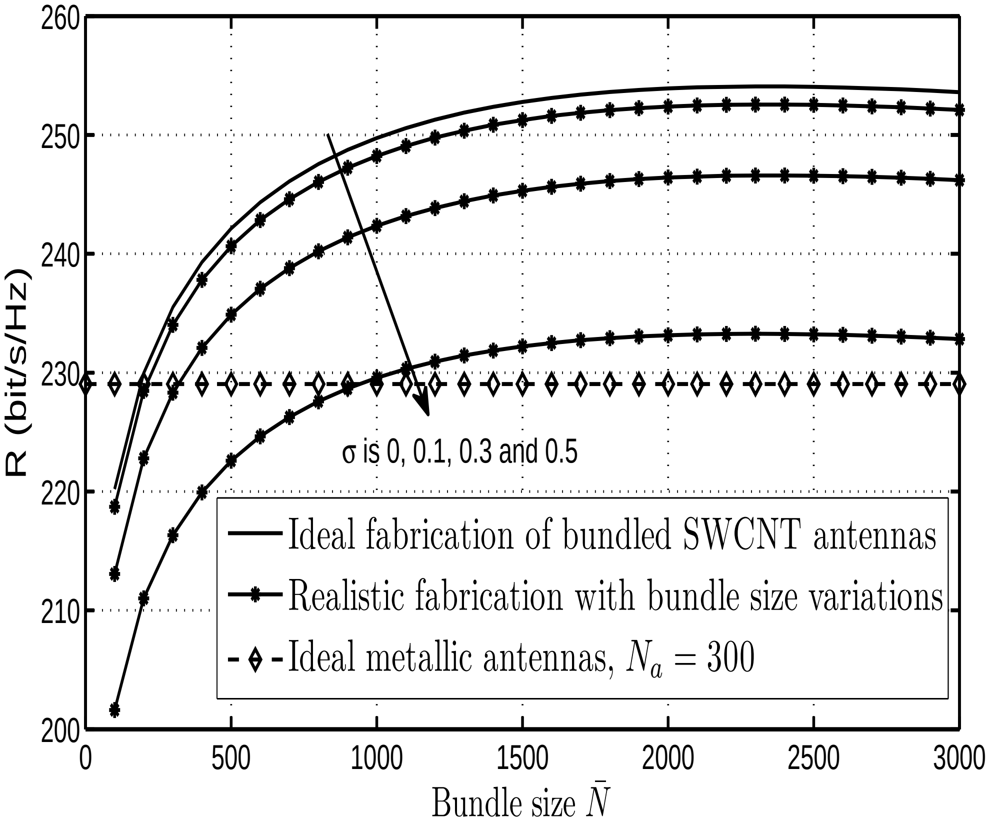

Figure 2.4: Uplink spectral efficiency for large scale MIMO, with $S = 1 \times 10^{-6}$ m^2, $K = 20$, $SNR_k = 10$ dB and $f = 2.6$ THz.

the antenna area size $S = 1 \times 10^{-6}$ m^2. When $\overline{N}$ is less than 1000, the spectral efficiency increases quickly as $\overline{N}$ gets larger. It indicates that in this region, the efficiency of antennas plays a more important role than the number of antennas in promoting spectral efficiency. From this figure, we can see that there is an optimal value $\overline{N}$ near 2000 which makes the spectral efficiency maximal. When $\overline{N}$ is larger than 2000, the spectral efficiency reduces slowly with the increase of $\overline{N}$. This implies that the effect of the number of antennas outweighs the efficiency of antennas gradually. The solid-star line shows the theoretical spectral efficiency when there exists fabrication variation. As the standard deviation σ increases from 0, 0.1, 0.3 to 0.5, the spectral efficiency decreases obviously. However, the optimal $\overline{N}$ is only slightly influenced. As a benchmark, the dashed line shows the performance of an ideal metallic antennas based MIMO system of the same S. The result indicates that when the fabrication variance is not large, the SWCNT bundled antenna based MIMO system has a higher spectral efficiency (by about 10%) than systems with ideal metallic antennas.

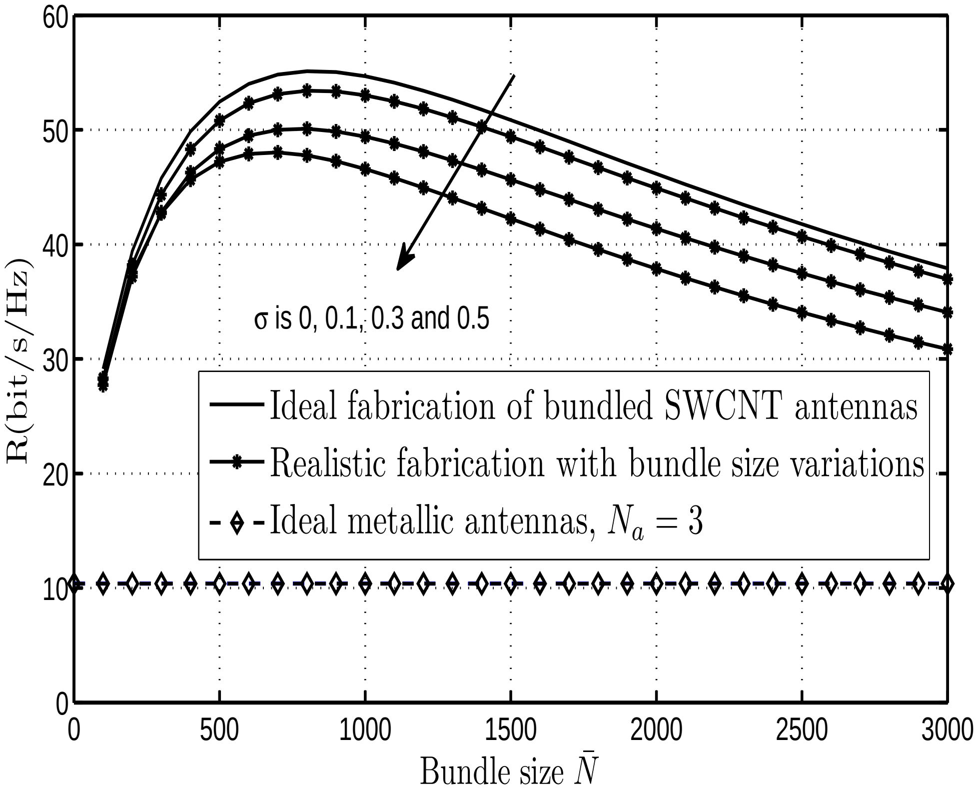

Figure 2.5: Uplink spectral efficiency for conventional scale MIMO, with $S = 1 \times 10^{-8}$ m^2, $K = 20$, $\overline{SNR}_m = 10$ dB and $f = 2.6$ THz.

For the conventional scale MIMO system, the spectral efficiency is shown in Fig. 2.5. We consider the same parameters as in Fig. 2.4, but choose the antenna area size as $S = 1 \times 10^{-8}$ m^2. These curves show similar behavior as those in Fig. 2.4. Compared with Fig. 2.4, the peaks are much more obvious and the spectral efficiency changes faster as $\overline{N}$ changes. The optimal value $\overline{N}$ is about 800 and when $\overline{N}$ is larger than 800, the efficiency decreases quickly. Therefore, we can conclude that the spectral efficiency is more sensitive to $\overline{N}$ than under scenario a. The dashed line has the same function as the line in Fig. 2.4. It shows that for a limited array size, the SWCNT bundled antenna based MIMO system has a higher spectral efficiency than ideal metallic antennas based MIMO systems.

2.5 Graphene-based Directional Antennas

2.5.1 Properties of Graphene

Graphene is a two-dimensional, infinitesimally thin sheet with a surface conductivity $\sigma(\omega, \mu_c, \Gamma, T)$, where ω is the radian frequency, μ_c is the chemical potential, Γ is the phenomenological scattering rate, and T is the temperature. Spatial dispersion effects may become significant under certain conditions, which modify the characteristics of graphene-based devices [43]. When the spectral wave number is extremely large, the full-k_ρ relaxation time approximation model is introduced to characterize the conductivity of graphene [44]. In this work, the normalized wave number (normalized with respect to the free space wave number) is between 50-100, and hence the spatial dispersion effect can be ignored [44]. Therefore, we can use the results from the Kubo formula [45]

$$\begin{aligned}&\sigma(\omega,\mu_c,\Gamma,T)\\&=\frac{je^2(\omega-j2\Gamma)}{\pi\hbar^2}[\frac{1}{(\omega-j2\Gamma)^2}\int_0^\infty\varepsilon(\frac{\partial f_d(\varepsilon)}{\partial\varepsilon}-\frac{\partial f_d(-\varepsilon)}{\partial\varepsilon})d\varepsilon\\&-\int_0^\infty(\frac{f_d(-\varepsilon)-f_d(\varepsilon)}{(\omega-j2\Gamma)^2-4(\varepsilon/\hbar)^2}d\varepsilon],\end{aligned}\tag{2.13}$$

$$n_s=\frac{2}{\pi\hbar^2v_F^2}\int_0^\infty\varepsilon[(f_d(\varepsilon)-f_d(\varepsilon+2\mu_c)]d\varepsilon,\tag{2.14}$$

where v_F is the Fermi velocity. The chemical potential μ_c is determined by the carrier density which can be controlled by application of a electrostatic bias voltage and chemical doping [46]. For a single layer graphene (SLG), suppose the bias voltage is V_g. Then, for each density of charged impurities n_{imp}, there exists a corresponding bias voltage $V_g = V_D$ that makes the conductivity of the graphene maximum. When $V_g = 0$, the conductivity of the graphene is minimized. In this work, the bias voltage $V_D = 15$ V [6]. If n_{imp} is large enough, the maximum conductivity of the highly doped graphene can be 10000 times larger than the minimum conductivity [6, 46]. Therefore, graphene has two modes: the low resistance mode when $V_g = V_D$, and the high resistance mode when $V_g = 0$.

2.5.2 Graphene-based Nano-patch Antennas

Graphene-based nano-patch antennas for THz communications usually have a dimension in the order of microns. As the width of the patches is finite, the edges of the graphene may modify the guiding properties of plasmons [47, 48]. In the THz range, there are two types of plasmon modes within the graphene patches: the waveguide mode and the edge mode. For the low frequency in our work (<2 THz), there is only one mode [47]. Besides, in this work, the width of the graphene patches is fixed, and therefore, the plasmon-light coupling angle is constant. We can directly synthesize different graphene patterns using chemical vapour deposition on thin nickel layers and transfer them to arbitrary substrates

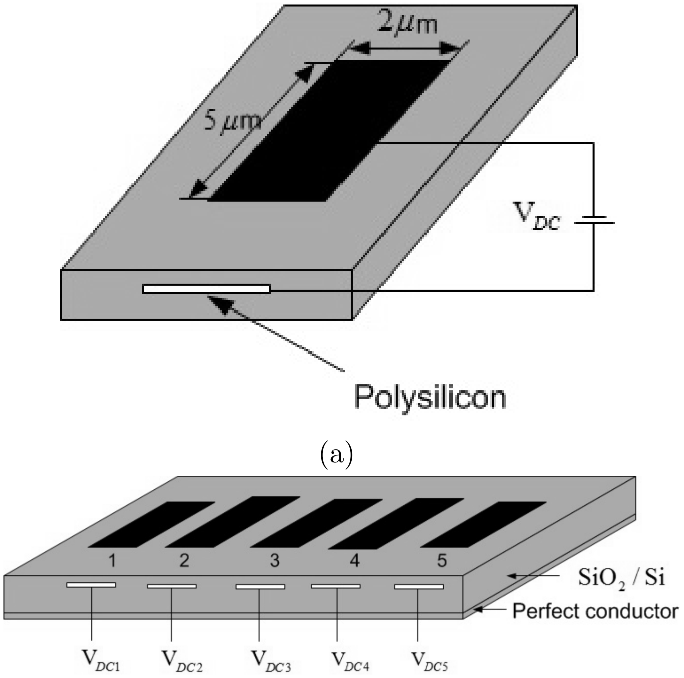

(a)

(b)

Figure 2.6: (a) A graphene-based nano-patch antenna element. (b) Graphene-based directional antenna with 5 elements, and each element has a similar size as the one in (a).

[49]. Although current technologies cannot fabricate graphene antennas with high efficiency, they might still be used in applications where low efficiency is tolerated and small antenna size is required. A nano-patch antenna sample made of graphene on SiO_2/Si substrate is shown in Fig. 2.6(a). In this example, the dimensions of the antenna are 2 μm × 5 μm which resonates at 1 THz [25]. This resonant frequency is much lower than that of the standard metallic dipole antennas of the same size. A photomixer is employed to couple the wave into graphene antennas, as explained in details in [50]. As an alternative, the wave can also be coupled by means of electric pumping [51, 52]. An electrostatic bias voltage is applied on the graphene to change its resistance modes. Suppose 1 THz is the resonant frequency at the low resistance mode. When the graphene changes to high resistance mode, the resonant frequency shifts away from 1 THz. For the fixed feeding frequency of 1 THz, the graphene patch resonates when $V_g = V_D$, and does not resonate when $V_g = 0$. Therefore, by changing the bias voltage, the radiation states can be configured dynamically.

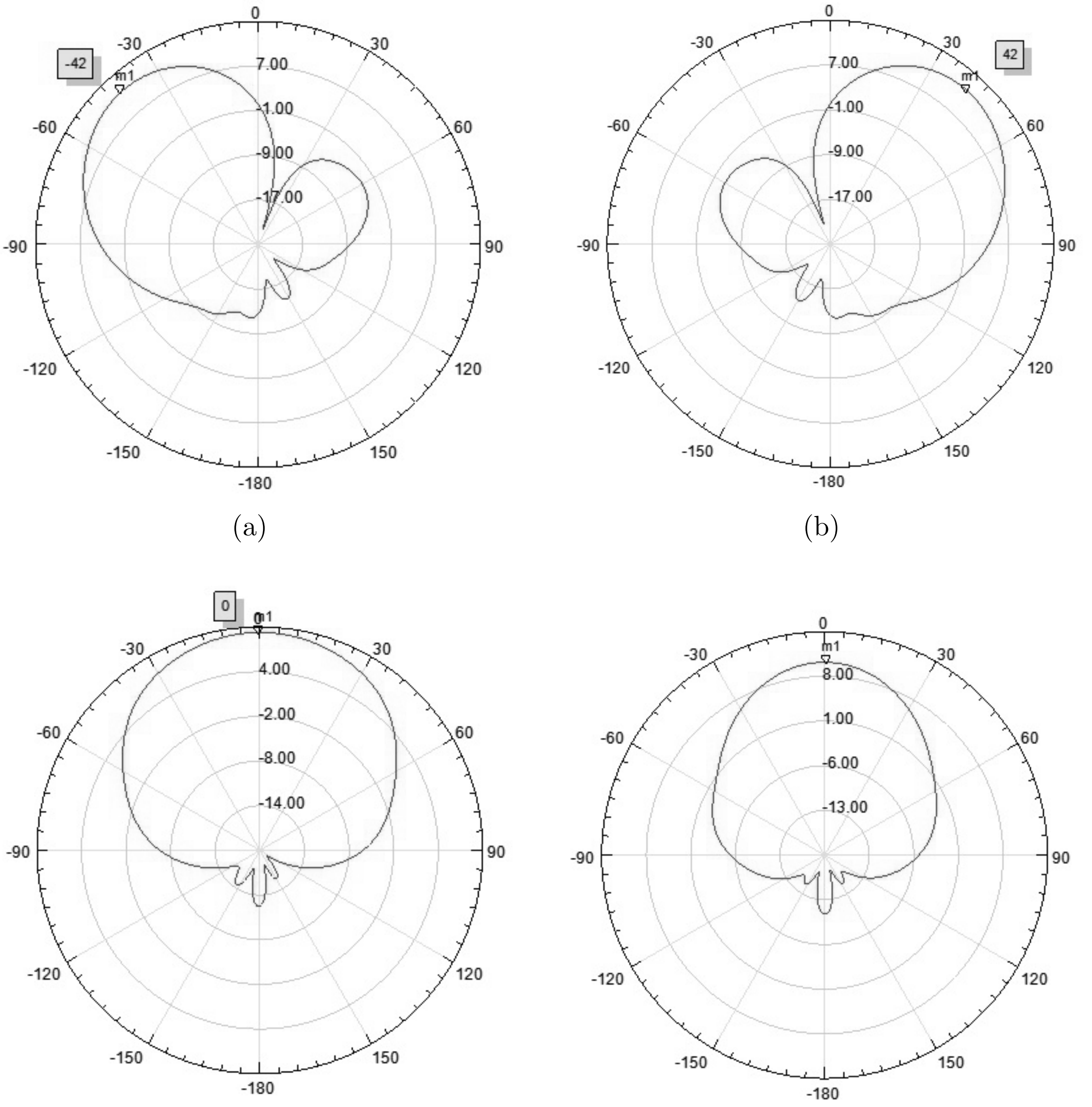

(a) (b)

(c) (d)

Figure 2.7: The radiation pattern of the antenna for $\mu_c = 1$ eV, $\Gamma = 1 \times 10^{12}$, T = 300 K, and the size of the driven element is 2μm × 5μm. The number of elements is (a-c) 5, and (d) 7. (a) Elements 1, 3 and 4 are in the low resistance state. (b) Elements 2, 3 and 5 are in the low resistance state. (c) Elements 1, 3 and 5 are in the low resistance state. (d) Elements 1, 4 and 7 are in the low resistance state. The operating frequency is $f = 1$ THz.

2.5.3 Graphene-based Reconfigurable Yagi-Uda Antenna

Recently, in order to adapt to the changing channels, reconfigurable antennas attract much interest in wireless communications [53]. In some scenarios, the length of the antenna can be dynamically changed so that the resonant frequency can vary. In some other cases, the reconfiguration features can be obtained by using phased antenna element arrays. Based on the aforementioned properties, we further consider a Yagi-Uda-based reconfigurable antenna with m patch elements, as shown in Fig. 2.6(b). The patch in the middle is used as the driven element, the two nearby patches (2, 4) are used as reflectors and all others are used as directors. The lengths of the reflectors are 7% longer than the driven element and the directors are 14% shorter than the driven element. There is a reflection sheet $\lambda/4$ below the antenna elements. Let c_i denote the mode of the ith graphene patch element and the mode set $[\mathbf{C}]_i = c_i$, where $\mathbf{C}$ is a vector. The commercial software Ansoft HFSS is used to simulate the radiation patterns of the antenna. By keeping some graphene patches in the low resistance mode while others are in the high resistance mode, different radiation patterns are produced. For example, when patches 1, 3, 4 are in the low resistance mode and 2, 5 are in the high resistance mode, the radiation pattern is shown in Fig. 2.7(a). In this case, the driven element (the 3rd patch) is excited by a 1 THz wave, and the reflector (the 4th patch) and the director (the 1st patch) are passive radiators and do not need feeding. At this stage, the significance of the coupling effects between two nearby graphene patches is not clear, and needs to be explored in future work. In this work, such coupling effects are assumed negligible. Fig. 2.7(b-c) show the radiation directions with other configurations which have a size of 5. Fig 2.7(a) and Fig. 2.7(b) indicate that the radiation direction has a dynamic range up to 80° and the beamwidth is 50°. Also, the beamwidth of the antenna can be modified by changing the number of elements. Fig. 2.7(d) shows the beamwidth of an antenna with 7 elements. In this case, the patches 1, 4, 7 are in the low resistance mode and 2, 3, 5, 6 are in the high resistance mode. Patch 4 acts as the driven element, and patches 1, 7 are the reflector and the director respectively. Similar to Fig. 2.7(c), the radiation direction is 0° as the reflector and the director have the same length. Obviously, the beamwidth is narrower and the gain is higher than those of 5. Fig. 2.7 indicates that we can get highly directional antennas with a narrow beamwidth by properly choosing the number of elements and the states of each element. Moreover, compared with the structure in [54], patches in high resistance mode do not introduce any interference to the desired patterns. Therefore, the graphene-based antenna has some distinctive properties suitable for THz communications systems. First of all, the size of antennas made of graphene is smaller which is important for devices in the THz band. Secondly, the radiation direction can be conveniently configured by changing the electrostatic bias voltage. Finally, the antenna is highly directional and with a high gain so that it can compensate the high attenuation loss in the THz band.

2.6 Graphene-based Gas Sensor

Molecular communication (MC) is regarded as a promising communication method in nanonetworks [55], especially for some scenarios for which electromagnetic communications are not suitable, such as communications in living organisms. Besides, the energy consumption of MC is much lower than that of electromagnetic based communications, which is essential to nano devices with limited energy. MC exchanges information by transmitting and receiving message-carrying molecules in a fluid environment. For example, calcium ions in water, NH_3 or CO_2 molecules in N_2 all can be used as carrier molecules. Due to the Brownian motion, molecules spread into free space spontaneously which changes the molecule concentration in a fluidic medium. After the diffusion, the concentration at the receive position can meet the sensitivity of the receiver. Then, the decoding can be done by chemical or biological reactions, depending on the properties of different information molecules.

Several papers model the physical channel [31, 32] and the channel capacity [33, 34] of MC, while others study the modulation and detection schemes [35]. Most of the existing papers focus on the propagation characteristics of the channel, but few of them analyze MC from a device's perspective. Paper [55] and [32] mention transmitters and receivers for MC, but none of them gives details of the devices or the performance. In one word, they assume that the receivers are ideal and can detect all the signals without error or delay. However, this is not true for MC. On the one hand, chemical or biological reactions are time consuming, thus the delay is usually larger than that of electromagnetic receivers; on the other hand, the performance of receivers deteriorates after every detection, especially for some irreversible chemical or biological reactions. Therefore, we can not ignore the performance of practical receivers, and new communication diagrams for MC should be studied.

2.6.1 Design of Graphene-based Gas Sensor

Graphene is an extremely low noise material with high conductivity, which makes it suitable for molecule sensing. When graphene is exposed to special gas molecules, molecules absorbed on its surface can act as donors (NH_3, CO)

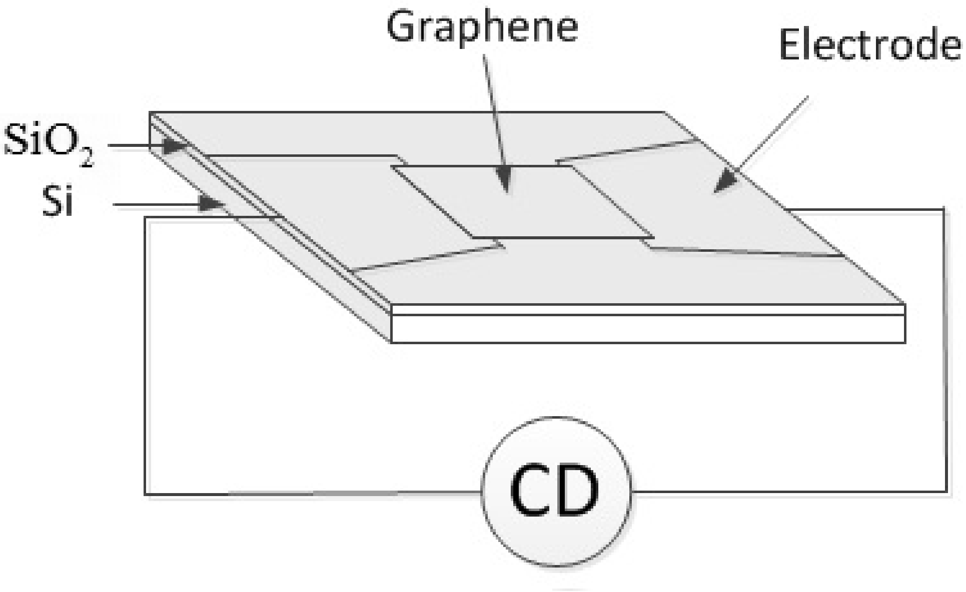

Figure 2.8: Sketch of a graphene-based receiver.

or acceptors (H_2O, NO_2), and the resistivity of graphene changes positively or negatively [56]. The graphene's unique properties make it able to detect the concentration change even as low as 1 part per billion (p.p.b). The high sensitivity is quite essential for long distance molecular communication (MC). Besides, different from other kinds of detectors, the graphene-based receiver can both absorb and desorb molecules, so it can easily return to its initial state, and the performance does not deteriorate after every detection.

The graphene-based receiver used in this work can be prepared by a stamping method [57, 58]. The sketch of the receiver is shown in Fig. 2.8. The graphene is deposited on a 300 nm thick SiO_2/Si substrate with two metal electrodes touching the edges. A voltage is applied across the two electrodes and a current detector (CD) records the slight current change through the graphene. According to the results in [2], the dimensions of the graphene layer are about 3 μm × 3 μm, and it is mostly uniform, which has a much simpler structure than other receivers [32]. When the voltage varies, the current changes linearly with the increase of the voltage, which means the resistance of the graphene is stable at the fixed temperature and humidity.

In this work, we use CO_2 molecules as the carriers and the CD detects the current change at room temperature. When the CO_2 concentration increases, more CO_2 molecules absorb on the graphene acting as acceptors. This kind of hole doping increases the resistivity of the graphene. When the CO_2 concentration is low, more molecules desorb from the graphene's surface, and the resistivity decreases correspondingly. Different from other molecules such as H_2O, CO, NO_2 [56], the

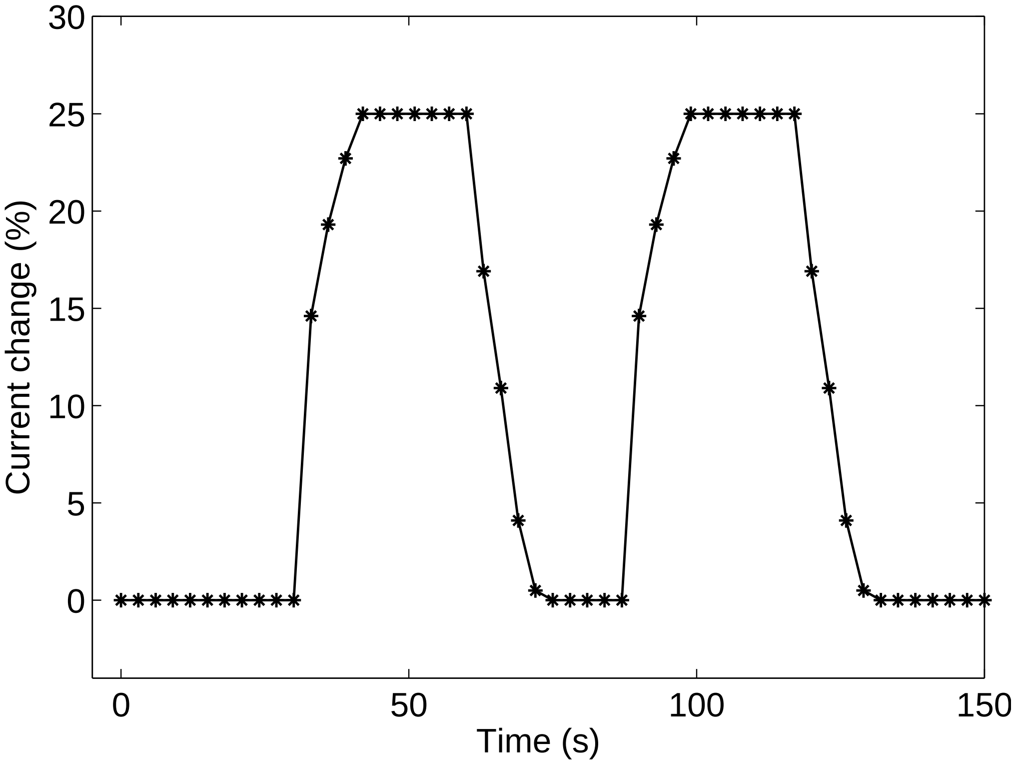

Figure 2.9: Time response of the graphene receiver. The temperature is 22 °C, and the CO_2 concentration is 100 p.p.m. Data from [2].

recovery time of CO_2 molecules is short as CO_2 only weakly interacts with graphene. The graphene receiver is tested with a CO_2 concentration of 100 parts per million (p.p.m). The time response of the graphene is shown in Fig. 2.9 [2]. From Fig. 2.9, we can see that both the response and recovery time are around 9 s, and the maximum current change can be as high as 25%. Besides, a higher molecule concentration can lead to a higher current change. Reference [2] estimates that the CO_2 sensitivity of graphene receivers is 0.17%/p.p.m.

According to the research on the properties of the graphene, some kinds of molecules have opposite effects on graphene. For example, NH_3 increases the conductivity of graphene while NO_2 decreases it. Therefore, we can use one kind of molecules and "silence" as the carriers of "1" and "0", or, we can use two kinds of molecules for better performance. Note that current technologies have not revealed two kinds of molecules who have perfectly opposite effects on graphene, thus the symbols using two kinds of molecules are not exactly orthogonal. Compared to other biochemical receivers, the graphene-based receiver has the following advantages:

- The sensitivity is much higher than that of other detectors, thus the receiver can detect molecules at a lower concentration, and the communication distance can be larger.

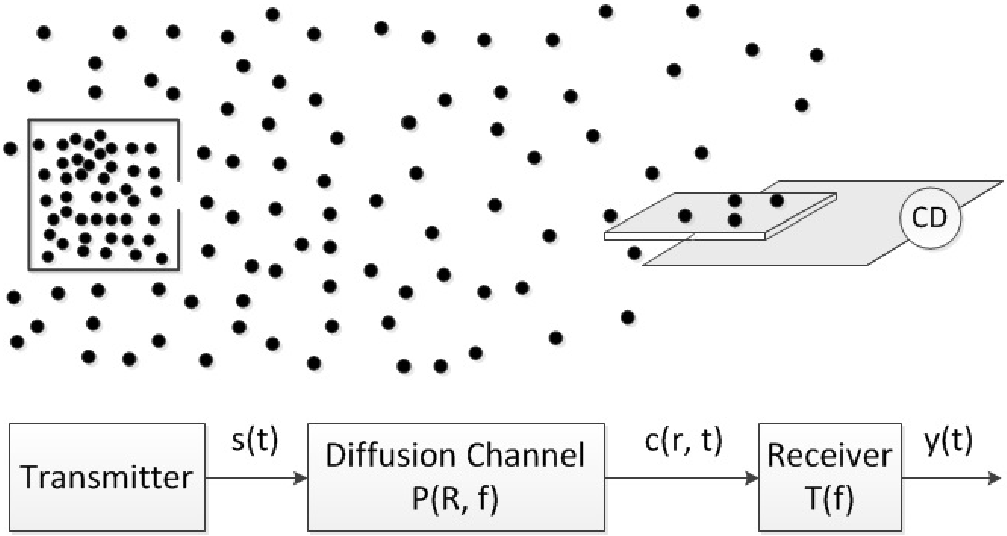

Figure 2.10: Sketch of a diffusion-based MC system with a graphene-based receiver.

- The detection and decoding are easier, as the graphene-based receiver translates the molecule concentration into the electrical signal.
- The conductivity of the graphene changes when molecules attach to or detach from its surface, thus the reaction is reversible.
- The graphene behaves differently to different kinds of molecules. Therefore, more modulation schemes can be adopted on the same receiver.

2.6.2 Molecular Communication System

Based on the aforementioned discussion, we analyze a communication system as shown in Fig. 2.10. The transmitter is a container with carrier molecules, which can release molecules under control. Compared to the entire system, the size of the transmitter is small enough and has no influence on the diffusion process. The diffusion channel is filled with a homogeneous concentration of gas molecules. The receiver is a graphene-based concentration detector and also small enough to be ignored. When Q molecules are released instantaneously, the molecular concentration in mol/cm^3 in space through time is given as [59]

$$c(r,t) = \frac{Q}{(4\pi Dt)^{3/2}} e(-r^2/Dt), \tag{2.15}$$

where r is the distance between the transmitter and the receiver, t is the time, and D is the diffusion constant in cm^2/sec. When the molecules are released at constant rate through time of Q molecules per second, the concentration function is given by [59]

$$c(r,t) = \frac{Q}{(2\pi Dr)} erfc(\frac{r}{\sqrt{4Dt}}), \tag{2.16}$$

where $erfc(x)$ is the complementary error function.

When the emission molecules are in a shape of $s(t)$ and the concentration after diffusion is denoted as $c(r,t)$, the transfer function of the channel in the frequency domain is

$$\mathbf{P}(R,f) = \frac{\mathbf{C}(R,f)}{\mathbf{S}(f)}, \tag{2.17}$$

where $\mathbf{S}(f)$ is the Fourier transform of $s(t)$, and $\mathbf{C}(R,f)$ is the Fourier transform of $c(r,t)$ at the position R from the transmitter. In this work, if $s(t)$ is a pulse with an energy of Q, then the transfer function is shown in Eq. (2.16). According to the relationship between the molecule concentration $c(t)$ and the current change $y(t)$, we can denote the response function of the graphene receiver as

$$\mathbf{T}(f) = \frac{\mathbf{Y}(f)}{\mathbf{C}(f)}, \tag{2.18}$$

where $\mathbf{Y}(f)$ and $\mathbf{C}(f)$ are the Fourier transforms of the current change and the molecule concentration at the receiver, respectively.

The responses of the channel and the graphene can be cascaded as a new channel response $\mathbf{H}(R,f) = \mathbf{P}(R,f) \cdot \mathbf{T}(f)$. Fig. 2.11(a) shows the transfer function of the diffusion channel. As the signal is an impulse signal, the transfer function of the channel can be obtained by Eq. (2.16) and Eq. (2.17). The pulse delay is proportional to r^2 and in this case is about 2 s. The amplitude is proportional to $1/r^3$ and is about 140 p.p.m. Due to the large delay and path loss, MC is more suitable for short range communications. In the same manner, the input in Fig. 2.9 can be regarded as a trapezoid wave signal $c(t)$, then the transfer function of the graphene is obtained by Fig. 2.9 and Eq. (2.18), as shown in Fig. 2.11(b). Note that this response is only the low frequency response. As shown in Fig. 2.11(c), $c(t)$ is a low frequency input signal. As a result, the high frequency part of the response cannot be obtained by the aforementioned method. Fortunately, in our model, the concentration signal $c(r,t)$ at position R is also a low frequency signal, as shown in Fig. 2.11(d). Therefore, the response of the model can still be perfect in spite of

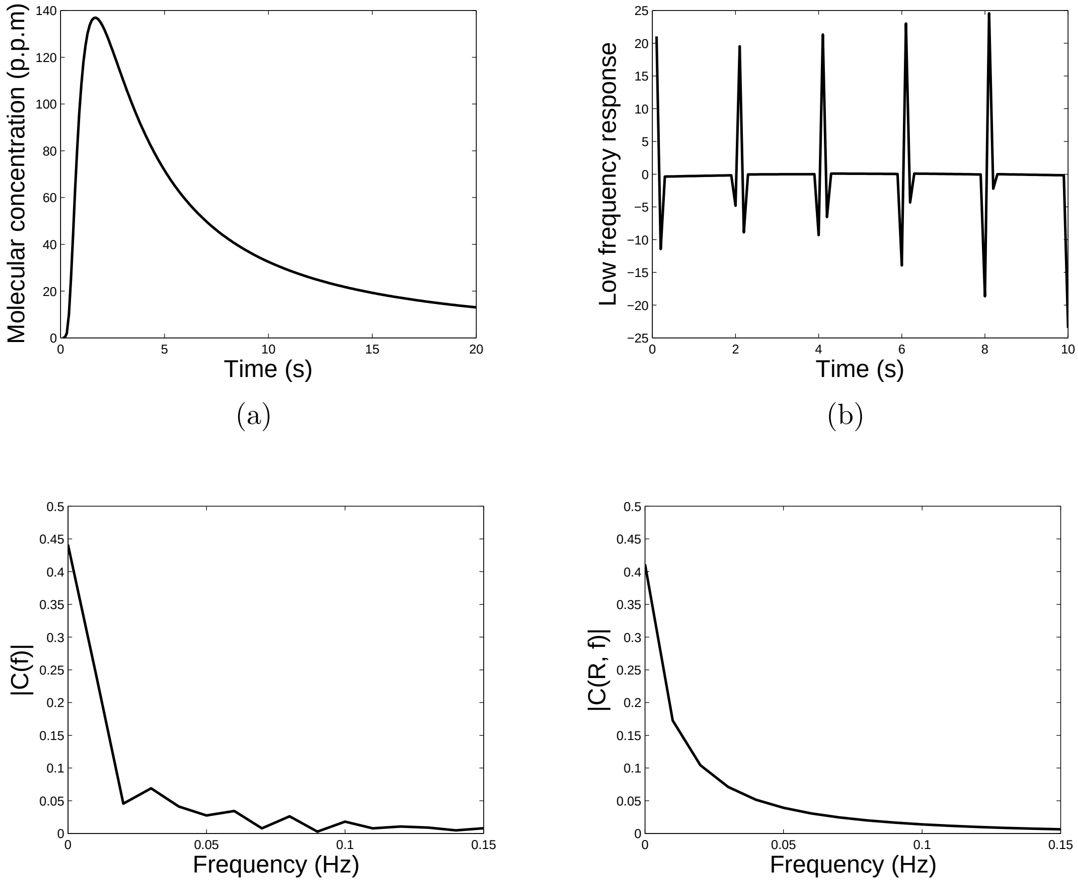

(a) (b)

(c) (d)

Figure 2.11: (a) The transfer function of the diffusion channel, (b) the low frequency response of the graphene, (c) the amplitude of the frequency spectrum of the molecule concentration $c(t)$ in Fig. 2.9, and (d) the amplitude of the frequency spectrum of $c(R, t)$ in Fig. 2.10. The molecule number is $Q = 5 \times 10^{10}$ and the distance from the transmitter is $R = 100$ μm.

the imperfect transfer function. As the time response of the graphene in Fig. 2.9 is not a closed-form solution, experimental results may introduce variations to the model. One way to minimize this effect is to precisely control the experimental environment and obtain enough data under different conditions. The other way is to get a theoretical relationship between time, molecule concentration and current change.

Fig. 2.12(a) indicates the combined transfer function with a distance of 100 μm. We can see that the signal is delayed about 9 s by the graphene. The maximum current change can be as high as 18%. Note that the variations are introduced by the deviation of the frequency response of the graphene. As a comparison, when the transmitter releases the molecules in a rectangle shape, the final received electrical signal after the current detector is shown in Fig. 2.12(b). The signal has a similar

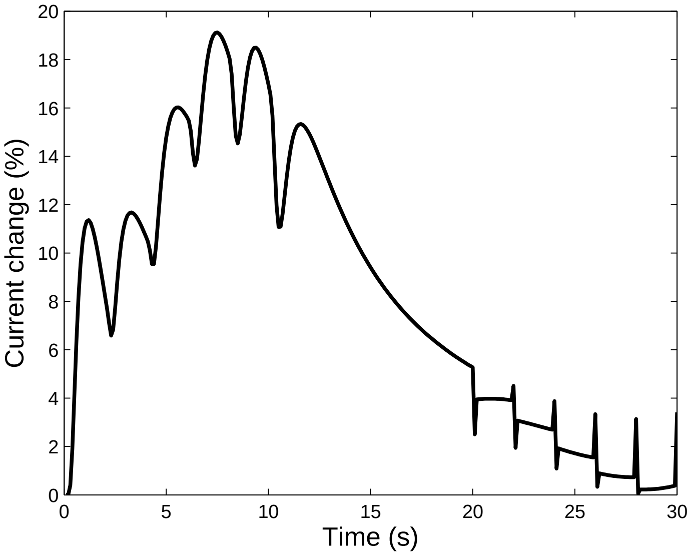

(a)

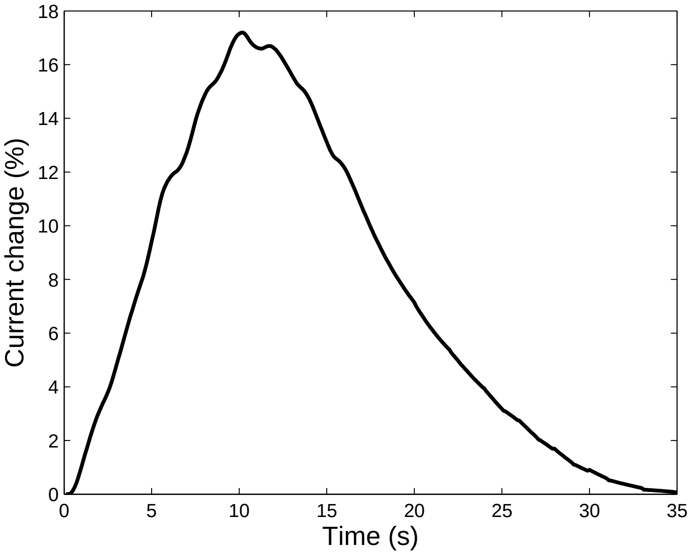

(b)

Figure 2.12: (a) Time response of the MC system with impulse transmit signals, with $Q = 5 \times 10^{10}$ and $R = 100$ μm, and (b) time response of the MC system with rectangular transmit signals, with $Q = 5 \times 10^{10}$ per second and $R = 100$ μm.

shape with that in Fig. 2.12(a), but with a larger delay.

The optimum detector for the electromagnetic signals can be a correlation demodulator or a matched filter demodulator. The output of the optimum detector has the maximum signal-to-noise ratio (SNR). As the noise is additive white

Gaussian noise (AWGN), the output SNR is

$$\mathbf{SNR} = \frac{2}{N_0} \int_0^T y(t)^2 dt = \frac{2E}{N_0}, \tag{2.19}$$

where E is the signal energy and N_0 is the power density spectrum of the noise. Similar to the energy detection in [35], the output SNR only depends on the energy of the signal $y(t)$ but not on the details of $y(t)$.

2.7 Conclusion

This chapter has proposed some graphene-based devices for wireless communications. First, the characteristics of graphene is introduced. Based on the unique properties, three devices have been proposed: CNT-based bundled antennas, graphene-based directional antenna and graphene-based molecule receiver. The SWCNT bundled antenna has many distinctive characteristics because of its unique electrical properties. We have studied the characteristics of SWCNTs and SWCNT bundled antennas and analysed the spectral efficiency of MIMO systems based on SWCNT bundled dipole antennas. There is a trade-off between the efficiency of antennas and the number of antennas as a function of bundle size. Under different scenarios, there exists an optimal bundle size which maximizes spectral efficiency. We showed that, for short range communications, the SWCNT bundled antenna based MIMO system has a higher spectral efficiency than ideal metallic antennas based MIMO systems. Furthermore, we investigated the effect of non-uniform bundle size in the fabrication process and showed that such variation can reduce spectral efficiency.

For the graphene-based directional antenna, the dimension is much smaller than metallic antennas with the resonance frequency. They are supposed to have a dimension on the order of microns. We propose a Yagi-Uda based reconfigurable antenna with m patch elements. The patch in the middle is used as the driven element, the two nearby patches are used as reflectors and all others are used as directors. By keeping some graphene patches ON while others are OFF, different radiation patterns are produced. The ON/OFF states can be conveniently configured by changing the gate voltage. The antenna is highly directional and with a high gain so that it can compensate the high attenuation loss in the THz band. Numerical results show that the dynamic range can be 80°, and the directional gain can be over 10 dB.

A graphene-based molecule receiver has a very high sensitivity. We have proposed a simple and efficient detection method for the molecule receiver based on graphene, which can not only enlarge the communication range, but also has a low complexity. For different kinds of transmit signals (impulse signals and rectangular signals), we have obtained the corresponding curves of the current change. By doing this, we change the molecule concentration into electrical signals, which have well studied algorithms to process. The results show that the delay is about 10 s and the maximum current change is over 20%. The performance of the MC system is also analyzed in this chapter. Numerical result shows that the high sensitivity can increase the data rate considerably.

Chapter 3

Reconfigurable MIMO System in the Terahertz Band

3.1 Introduction

The MIMO antenna technique is well known to increase the spectral efficiency of a wireless communications system [9]. If the amount of scattering and reflections in the multipath environment is large enough, then more transmit and receive antennas result in more data streams and higher spectral efficiency. However, for real MIMO systems with limited area, the antenna size and antenna separation are the main obstacles to increasing the MIMO scale, which is difficult to solve when using traditional omnidirectional antennas. To deal with this problem, graphene-based directional antennas can be promising candidates to decrease the antenna size [24]. Also, high directional antennas can reduce the antenna separation by enlarging the angular spread. Another way to increase spectral efficiency is using reconfigurable antennas. For example, by controlling the antenna length [53, 60] or the states of the antenna array [6, 7], the radiation pattern is changed dynamically, which increases the spectral efficiency by 10% to 70%.

In the long term, the only promising way to meet the demand of ultra high data rate is to shift the carrier frequencies to the THz band. However, the THz channel has many characteristics different from the GHz channel, such as much higher propagation loss and extra molecular absorption loss [42]. Thus, the models for the GHz channel cannot be applied directly to the THz channel. Reference [42] models the THz channel and analyzes the capacity of wireless networks. The results show that the capacity can be as high as 100 Tbit/s but drops quickly because the path loss for long distance is relatively high. To conquer this problem, the authors in [11] suggest to use highly directional antennas at THz frequencies in realistic indoor environments. Besides the path loss, the scattering and reflection behaviours are also different from those in the GHz band [5, 8]. For THz waves, the surfaces of indoor objects must be regarded as rough surfaces instead of smooth surfaces. When the surface is rough enough, the specular reflection may lose its privileged position, and the diffusely scattered paths may be even stronger [3]. Therefore, these unique features lead to new models to characterize the THz channel.

3.2 Related Work

Reference [54] presents a novel linearly polarized pattern reconfigurable microstrip parasitic array. It is able to shift the radiation to any of three angles using only four switched connections, only with a size comparable to a common microstrip patch antenna designed for the same frequency. Reference [53] studies reconfigurable antennas in MIMO communication systems for the purpose of adapting to the changing channel. It analyzes the potential improvements in MIMO system capacity by the use of a small number of pattern reconfigurable antennas. Reference [60] proposes a reconfigurable microstrip dipole antenna solution for MIMO communication systems. Their measurement results show that the reconfigurable antenna solution can provide a considerable improvement in capacity compared with a system which does not have reconfigurable antennas.

3.3 Contribution

In this work, a new reconfigurable MIMO antenna system for THz communications is designed based on graphene Yagi-Uda antennas. The main contributions of this work are summarized as follows:

- Based on the THz channel model, we propose a new MIMO antenna system for THz communications. The transmitter in the system is an array of antennas and each antenna is an array of graphene patches. In our system, each antenna in the antenna array is a graphene-based directional antenna instead of a traditional omnidirectional metallic antenna, which results in a smaller antenna size and separation. Note that employing highly directional antennas in the GHz range would result in unacceptable large devices.
- We apply the designed reconfigurable graphene-based directional antennas to THz MIMO system, and analyse the spectral efficiency of such MIMO

systems under different scenarios. We show that the antenna separation can be tremendously reduced if directional antennas are used. In particular, if the transmitter can obtain the channel side information (CSI) from the receiver, then the optimal radiation pattern of each antenna can be configured; otherwise, the transmitter uses a fixed radiation pattern.

- We investigate the performance of such a reconfigurable MIMO system via simulations. The results are compared between different power allocation schemes as well as with the performance of traditional metallic antenna based MIMO systems. It is shown that by employing the best configuration, our system can considerably increase the spectral efficiency.

3.4 Model of the Terahertz Channel

In order to increase the spectral efficiency to meet the requirements of future wireless communications in current frequency bands, advanced modulation schemes and signal processing technologies are not enough. Therefore, the THz band (0.1 - 10 THz) is regarded as one of the most promising spectrum bands. The THz channel model has been discussed in several recent works [5, 8, 42, 61, 62], and in this work, we use the results in [42]. A signal in the THz band suffers both spreading loss and molecular absorption loss, which is different from that in the GHz band in which molecular absorption loss can be ignored. The total path loss in the THz band is [42]

$$A(f,d) = A_{spread}(f,d) + A_{abs}(f,d), \tag{3.1}$$

where $A_{spread}(f,d)$ is the spreading loss at distance d and frequency f, defined in dB as

$$A_{spread}(f,d) = 20\log(\frac{4\pi f d}{c}), \tag{3.2}$$

where c is the speed of light in free space, and $A_{abs}(f,d)$ is the molecular absorption attenuation denoted in dB as

$$A_{abs} = k(f)d10\log_{10} e, \tag{3.3}$$

where $k(f)$ is the medium absorption coefficient. As the air is the composition of different molecules (e.g., nitrogen, oxygen and water vapor), $k(f)$ is the sum of weighted coefficients of each gas. When the concentration of the water vapor is high, several peaks of attenuation are observed due to the molecular absorption loss, and the total band is segmented into several transmission windows. Except for these peaks, the total path loss only depends on the distance and the frequency, independent of the molecular composition, which is similar to that in the GHz band. Eq. (3.2) indicates that the spreading loss in the THz band is 60 dB higher than that in the GHz band, thus the THz frequency is only suitable for short range communications.

Besides the differences in path loss, the reflection properties are also different from those in the GHz band. For objects (e.g., plaster or wallpaper) in indoor environments, the surface variations are on the order of several hundred microns to millimeters [5, 8], which are comparable to the THz wavelength λ (e.g., wavelength at 1 THz is 300 microns). Therefore, the surfaces of indoor objects, which can be regarded as smooth surfaces at the GHz frequency, are now rough surfaces at the THz frequency. According to the analysis in [3, p.81], the roughness factor is

$$\rho = (\rho_0 + \rho_1)e^{-g/2} \tag{3.4}$$

with

$$g = (\frac{2\pi \cdot \Delta \cdot (cos\theta_1 + cos\theta_2)}{\lambda})^2, \tag{3.5}$$

where ρ_0 is the scattering coefficient corresponding to the specular reflection, and ρ_1 is the corresponding one due to the diffusely scattered field; Δ is the standard deviation of the surface roughness, θ_1 and θ_2 are the angles of incidence and reflection. When $g = 0$ (smooth surface), $g \ll 1$ (slightly rough), $g \geq 1$ (moderately rough) and $g \gg 1$ (very rough), the scattering patterns are shown in Fig. 3.1(a-d) [3]. From the scattering patterns, we know that when the surface is rough enough, the reflection angles can be different from the incident angles, and the receive antennas can get the signals from different positions. Therefore, this effect can lead to many diffusely scattered multipath components [3, 5, 8], and rough surfaces have more reflection spots than smooth surfaces. As shown in Fig. 3.2(a) and (b), when the transmit antenna is an omnidirectional antenna, only one path exists if the surface is smooth while multiple paths exist if the surface is rough. This means that when the transmit antenna is highly directional, it can only radiate signals to one direction

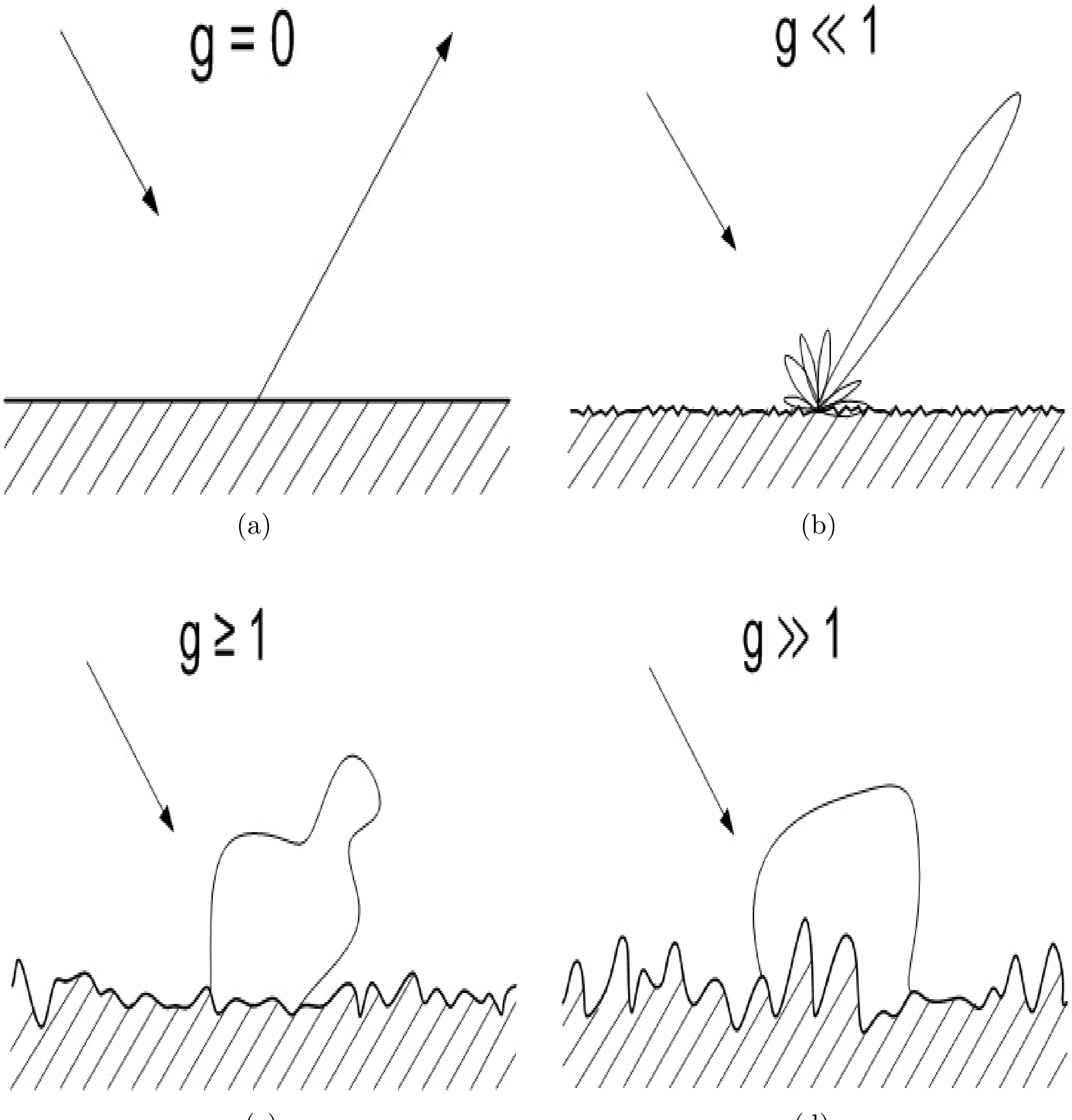

(a) (b) (c) (d)

Figure 3.1: Transition from specular reflection to diffuse scattering. The surfaces are: (a) smooth, (b) slightly rough, (c) moderately rough, and (d) very rough. Data from [3].

(specular reflection direction) if the surface is smooth; on the other hand, if the surface is rough enough, the transmit antenna can send signals in different directions and the receive antenna can still receive them, as the non-specular reflection paths are strong enough to provide stable links.

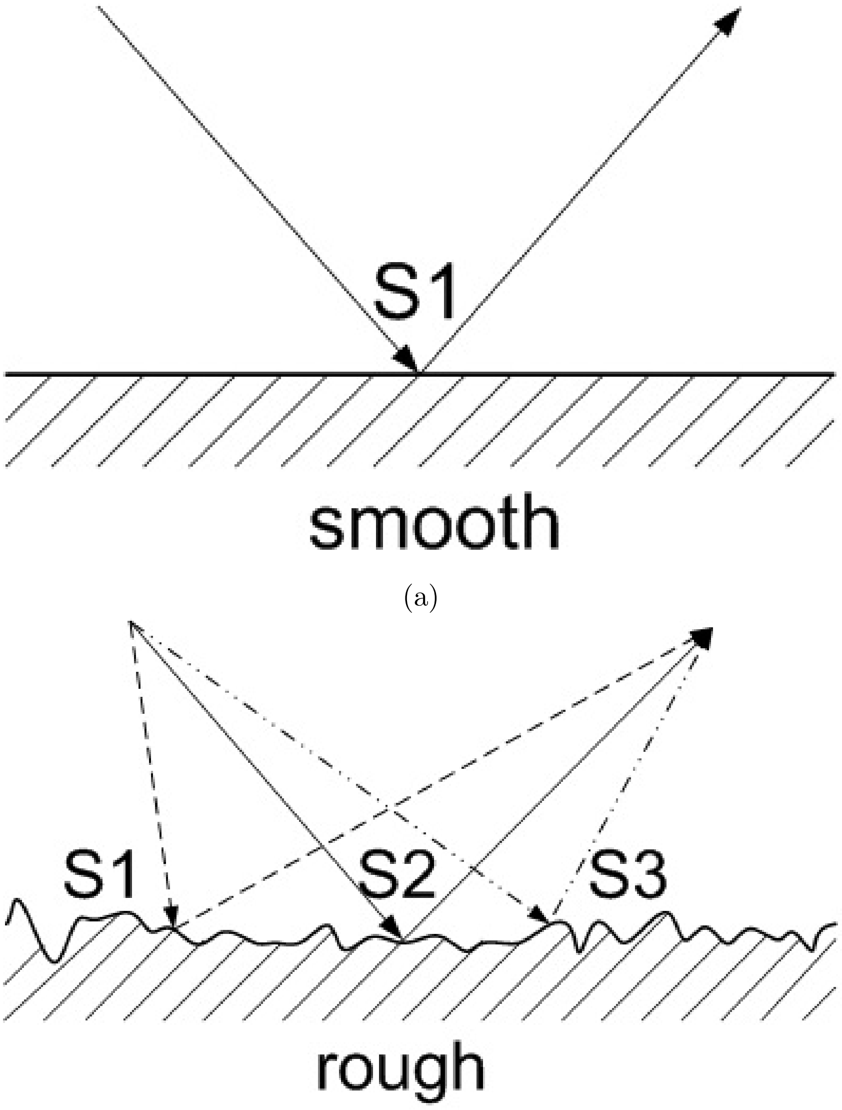

(a)

(b)

Figure 3.2: (a) Single spot reflection from a smooth surface, and (b) multiple spot reflection from a rough surface.

3.5 Reconfigurable MIMO System

3.5.1 Model of the MIMO System

The aforementioned effect makes the THz MIMO model different from that in the GHz band. In this chapter, we consider a system with M transmit antennas and N receive antennas, and the channel can be represented as an $M \times N$ matrix $\mathbf{H}$. The time invariant channel is described as

$$\mathbf{y} = \mathbf{H}\mathbf{x} + \mathbf{w}, \tag{3.6}$$

where $\mathbf{x}$ is the transmit signal, $\mathbf{y}$ is the receive signal and $\mathbf{w}$ is the white Gaussian noise. The capacity of the channel is [9]

$$C = \sum_{i=1}^{n_{min}} \log_2(1 + \frac{P_i \lambda_i^2}{N_0}) \text{ b/s/Hz}, \tag{3.7}$$

where n_{min} is the rank of $\mathbf{H}$, P_i is the transmit power, N_0 is the noise power spectral density and $\lambda_1, \lambda_2, \cdots, \lambda_{n_{min}}$ are the singular values of the channel matrix $\mathbf{H}$. In recent years, much effort has been invested to increase this capacity, such as using optimistic power allocation schemes, increasing the rank of $\mathbf{H}$ [9] or using massive MIMO [63]. For most cases, the limited area on the device is the main concern in increasing the rank of $\mathbf{H}$ and implementing enough antennas. For example, $\mathbf{H}$ is ill-conditioned if the antenna separation is too small. Meanwhile, when the separation is large, the number of antennas on the device will be small. Therefore, there is a tradeoff between the number of antennas and the condition of $\mathbf{H}$. For the GHz MIMO, we know from [9] that the minimum transmit antenna separation normally is $\lambda_c/2$, where λ_c is the wavelength of the signal in free space. If the separation is far less than $\lambda_c/2$, then the signals from two transmit antennas cannot be resolved by the receive antennas, and there is effectively only one degree of freedom. Therefore, it is useless to pack too many antennas in a given amount of space as the angular resolvability does not increase.

However, for the THz MIMO, if all the transmit antennas are highly directional, then the transmit antenna separation can possibly be below $\lambda_c/2$. The reason can be explained as follows. If one directional antenna radiates in a selected direction, because of the rough surfaces, it has high probability that the link is strong enough, as shown in Fig. 3.2(b). It means that in a certain angle range, the highly directional antennas can choose any radiation directions to establish the link. Therefore, two neighbouring antennas can radiate in different directions, and the angular spreads at THz frequencies are larger than those in the GHz range, which means the transmit antenna separation can be smaller than $\lambda_c/2$ in the THz, as shown in Fig. 3.3. On the other hand, as the atmospheric attenuation is quite strong and the free space loss is high, in order to guarantee a better transmission link, it is also a requirement to use high gain directional antennas in the THz band. Therefore, for THz MIMO systems, not only the graphene-based antenna size is extremely small, but also the antenna separation can be much smaller than the free-space wavelength. This phenomenon can allow the device to accommodate more antennas and increase the channel capacity as a result.

Following the aforementioned analysis, we propose a reconfigurable MIMO

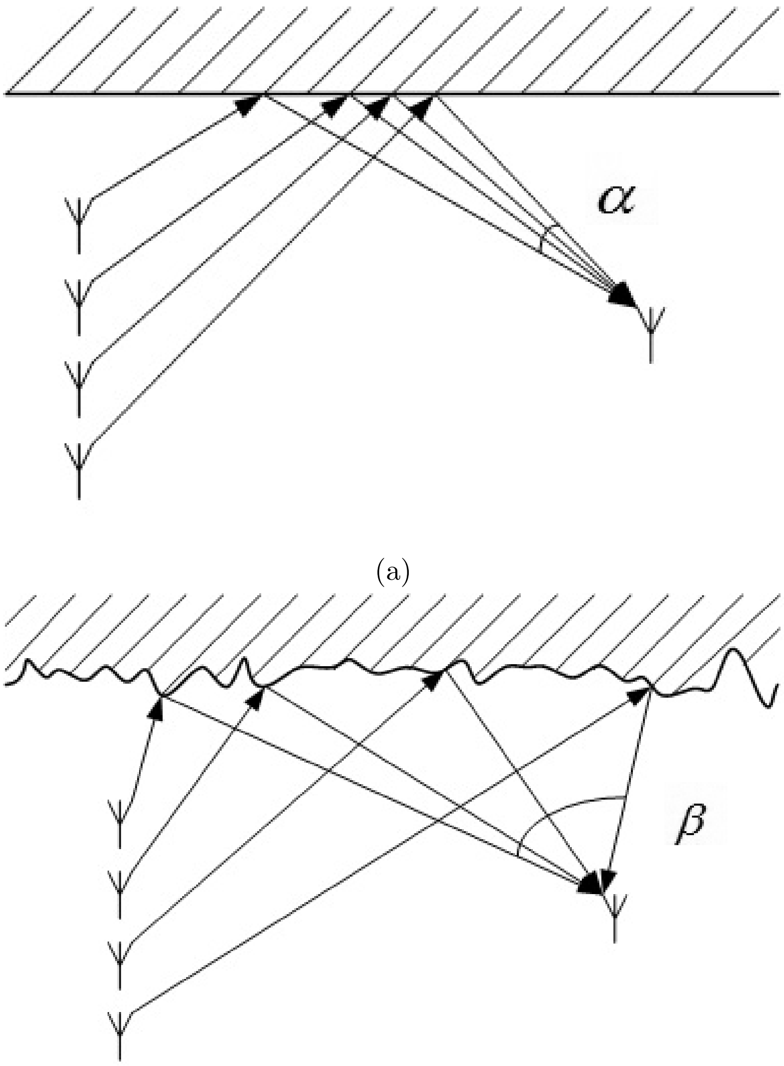

(a)

(b)

Figure 3.3: The angular spreads when the surface is (a) smooth, and (b) rough.

antenna design for THz communications based on graphene antennas. The transmitter in our system has an array of antennas and each antenna is an array of nano-patches. The salient features of the design are as follows:

- The transmit antenna separation is smaller than that in GHz MIMO systems. A separation less than $\lambda_c/2$ can make the transmit antenna array smaller and accommodate more antennas on the same area.
- Each antenna in the MIMO system is a highly directional antenna with different radiation directions, and the directions can be configured dynamically. By changing the radiation directions, the transmit antennas can choose the best paths according to the environment.

- The highly directional antenna is made of an array of nano-patches and its radiation pattern is controlled by the states of each graphene patch. The size of graphene-based nano-patch is much smaller than that of a traditional metallic nano-patch, and the states can be easily changed by the electrostatic bias voltage. The patches in the high resistance state are assumed not to introduce interference to the radiation pattern.

- For all the directional antennas, there exists one best radiation direction set that makes the capacity largest. If the channel side information (CSI) is known at the transmitter side, then such best set can be obtained by solving an optimization problem or rolling all the possible sets.

3.5.2 Formulation for the Optimal Configuration

For the sake of clarity and briefness, we first use a 2 × 2 MIMO system as an example. The model setup is shown in Fig. 3.4. Let h_{ij} denote the channel gain between the ith transmit antenna and the jth receive antenna. Then, we get $[\mathbf{H}]_{i,j} = h_{ij}$ and $h_{ij} = -A_{spread}(f, d) - A_{abs} + \rho \cdot \gamma$, where γ is the Fresnel reflection coefficient for a smooth surface. For fixed positions of transmit and receive antennas, h_{ij} is controlled by the incident angle θ_{Ii}. Once the radiation direction is determined, the path length d, the reflection spot, the roughness factor ρ and the reflection angle θ_{Oij} are all obtained. Therefore, for each direction set $[\theta_{I1}, \theta_{I2}]$, there is one unique channel matrix $\mathbf{H}$. The direction set can influence the spectral efficiency in two ways: on one hand, in order to get the lowest path loss, all transmit antennas need to radiate to the same "optimistic" direction which will certainly increase the received signal power; on the other hand, receive antennas cannot distinguish signals from similar directions, thus the degrees of freedom decrease if the directions of the transmit antennas are the same. Thus there is a tradeoff between the received power and the degrees of freedom. Besides, in our example, if the positions of the transmit and receive antennas are known, then the best direction set can also be

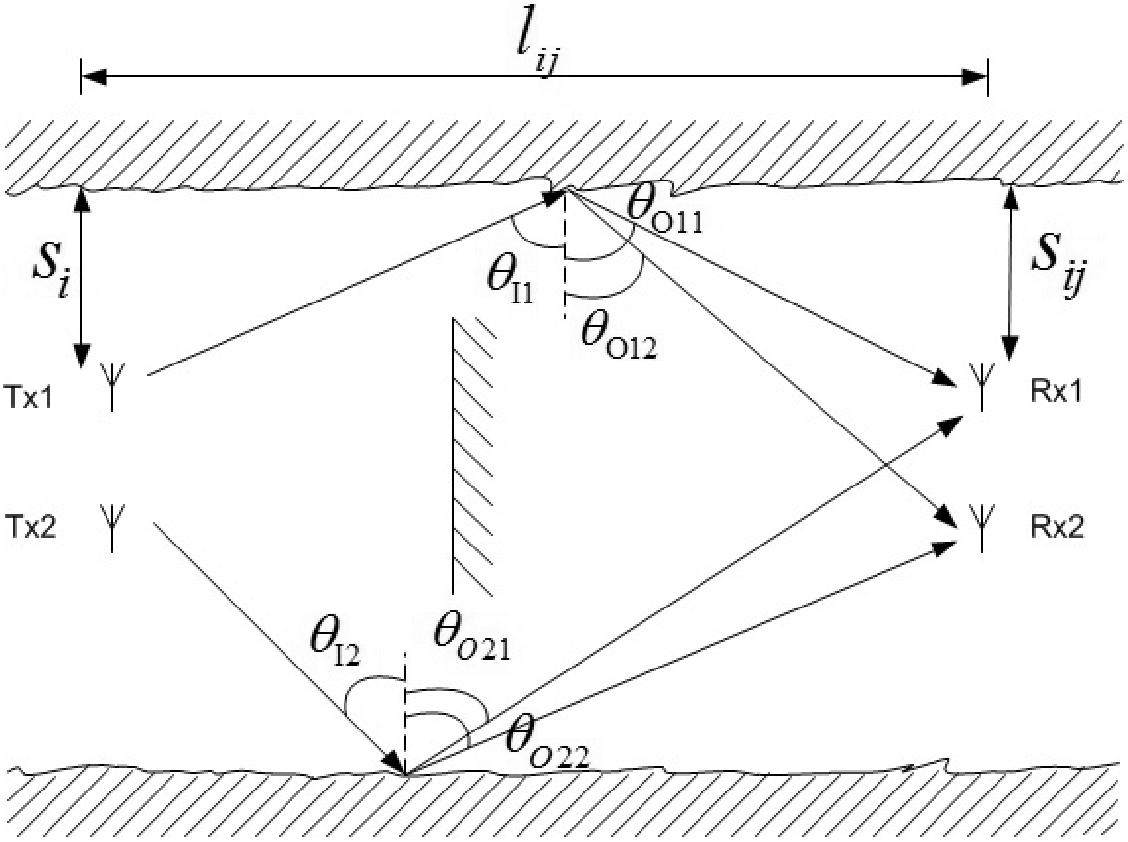

Figure 3.4: A MIMO model based on nano-patch antenna array. s_i is the distance between the ith transmit antenna and its reflecting object, s_{ij} is the distance between the jth receive antenna and the ith transmit antenna's reflecting object, and l_{ij} is the horizontal distance between the ith transmit antenna and the jth receive antenna.

obtained by solving the following optimization problem

$$
\begin{aligned}
\underset{P_i,\theta_{Ii}}{\text{maximize}} \quad & C = \sum_{i=1}^{n_{min}} \log_2\left(1 + \frac{P_i \lambda_i^2}{N_0}\right) \text{ b/s/Hz}, \\
\text{subject to} \quad & \sum_{i}^{n_{min}} P_i \leq P, \\
& \frac{s_i}{cos\theta_{Ii}} + \frac{s_{ij}}{cos\theta_{O}ij} = d_{ij}, \\
& s_i tan\theta_{Ii} + s_{ij} tan\theta_{Oij} = l_{ij}, \\
& h_{ij} = -A_{spread}(f, d_{ij}) - A_{abs} + \rho.
\end{aligned}
\tag{3.8}
$$

where P is the total transmit power, s_i, s_{ij}, l_{ij} are constants shown in Fig. 3.4, and d_{ij} is the path length between the ith transmit antenna and the jth receive antenna.

When the channel condition is known at both transmitter and receiver sides, the main difficulty in realizing our model is solving the aforementioned optimization problem. Consider the limited computing ability and battery power, it is not possible or necessary to get the optimal solutions using mobile devices. In this situation, we can use a sub-optimal scheme instead of the optimal one. Suppose the radiation direction set is denoted as $\mathbf{D} = [\theta_{I1}, \cdots, \theta_{Ii}, \cdots, \theta_{IN}]$. First of all, we design a group of sets $\mathbf{D}$ in which two identical directions are avoided. In theory, the more the two directions separate from each other, the more independent they are. If the transmit antennas can obtain the feedback from the receive antennas, then an optimal direction set can be achieved by polling all the possible candidate sets. For example, the first antenna radiates to $\pm 15^\circ$ and $\pm 30^\circ$ (the line of sight is 0°) and gets 4 feedbacks from each receive antenna. In the same way, the second antenna can also obtain 4 feedbacks. Eliminating some unqualified direction sets, only a few direction sets are possible to get the best $\mathbf{H}$. Here the best means the one with the largest rank and eigenvalues. As the environments change quite slowly for indoor communications due to slowly moving objects, we only need to feedback once in a long time period, thus the entire overload is bearable. Finally, we fix the radiation directions and determine the power allocation scheme using the water-filling algorithm. In this algorithm, the direction and the power are not jointly optimized but treated as two independent factors.

Now we consider the scenarios with larger system scales. When the scale is larger than 2×2, such as 4×4 or 8×8, the process is the same as that of 2×2, but with more complex models and workload. When it comes to the massive MIMO range, graphene-based directional antennas are also more suitable than traditional omnidirectional metallic antennas. For example, our antennas can be applied to the dynamic massive MIMO shown in [10]. As we know, the dimension of the antenna array is one of the main obstacles to implementing massive MIMO. By using highly directional graphene antennas, the antenna size and separation are smaller, and the dimensions of the antenna array can be tremendously reduced. Besides, as all the antennas in the array can freely change their directions, the channel state is more random if the antennas randomly choose their directions. Therefore, the assumption that "the fast fading coefficients are assumed to be zero-mean and unit-variance" in [41, 63] is more reasonable, and the final results could be better. When using a zero forcing (ZF) detector, the channel capacity for massive MIMO with M receive antennas is [41]

$$C = \log_2(1 + p_u(M - K)\beta_k) \text{ b/s/Hz}, \tag{3.9}$$

where K is the number of transmit antennas, p_u is the transmit power and

β_k denotes the large scale fading factor. For other kinds of detectors, we refer readers to [41] for detailed formulas. Regardless of the detectors, the capacity is highly positively correlated to the number of antennas M. Therefore, graphene-based directional antennas can also promote the capacity of massive MIMO by accommodating more antennas in a given area. The exact performance enhancement will be studied in future work.

3.6 Results

3.6.1 Channel Behavior Analysis

In order to get the capacity of the MIMO system, the path loss in the THz band should be studied first. In our simulations, we set the working frequency as 1 THz which is one of the transmission windows [61] and also results in the corresponding size of the nano-antennas being proper for fabrication. We explore the path loss between the first transmit antenna and the first receive antenna, as shown in Fig. 3.4. Based on the aforementioned channel model, we know that the path loss is a function of radiation direction and distance. For indoor environments with objects and moving people, we can assume there is no line-of-sight between the transmit and receive antennas [8]. Besides, we can ignore the multi-bounce reflected rays as they are much weaker than single-bounce reflected rays [8]. Therefore, the connections between the transmit and receive antennas are rays with one single-bounce reflection. As discussed in Section 3.3, the path loss in our scenario is contributed by spreading loss, molecular absorption loss and reflection loss. The spreading loss and molecular loss are determined by the transmission distance d while the reflection loss is controlled by the radiation direction. Comparing the wavelength of the signal (300 nm at 1 THz) with the variations of different surfaces (88 nm for plaster and 90 nm for wallpaper [8]), g is on the order of unity and thus the surfaces can be considered as moderately rough.

We first fix the positions of all antennas and reflection objects. The parameters in Fig. 3.4 are set as follows: $s_1 = 1$ m, $s_{11} = 1$ m and $l_{11} = 2$ m. By increasing the incident angle from 30° to 60°, the spreading loss and the molecular loss vary due to the change of the transmission distance, as shown in Fig. 3.5(a). The minimum spreading loss is achieved when the incident angle is 45°, as the specular reflection has the shortest transmission distance. However, the other incident angles only slightly increase the spreading loss. The loss due to the roughness factor is obtained using Eq. (3.4), as shown in Fig. 3.5(b). Interestingly, in this case, the minimum loss is achieved when the incident angle is around 54°, rather than 45°. This means the specular reflection path is not always the best path when the surface is rough enough. Therefore, the total path loss shown in Fig. 3.5(c) is the combination of the lines in Fig. 3.5(a) and Fig. 3.5(b). From Fig. 3.5(c), we can get the conclusion that the best path between the transmit and receive antennas is near the specular reflection path, yet other paths are also strong enough to provide stable connections.

3.6.2 Channel Capacity Analysis

The channel capacity for 2 × 2 MIMO with different transmit power is shown in Fig. 3.6. The parameter setup is the same as that in Fig. 3.5 with $s_2 = 1$ m, $s_{12} = 1.5$ m, $s_{21} = 1$ m, $s_{22} = 0.5$ m, and $l_{ij} = 2$ m, $i, j \in \{1, 2\}$. The separation of the two transmit antennas is 0.1 mm (one third of the wavelength) while the separation of the two receivers is 0.5 m (usually the separation of different receivers is on the order of meters). In this simulation, the spectral efficiency is determined by the radiation directions, the transmit power and the noise power. The dotted line (isotropic antennas, Rx CSI) shows the spectral efficiency of the traditional MIMO system model with omnidirectional metallic antennas and smooth surface. The links between the transmitters and the receivers are all specular reflected rays. As a comparison, the circled line (directed antennas, Rx CSI) shows the spectral efficiency of the MIMO system with directional antennas. The spectral efficiency is higher than the dotted line which is more obvious when the transmit power is large. The reason is that under our assumptions, the system can fully use all of the degrees of freedom even if the antenna separation is small and the scattered rays are limited. Furthermore, the solid line (directed antennas, Rx and Tx CSI) is the spectral efficiency of the system with the best power allocation scheme. In this example, we assume the CSI is known by the transmit antennas and the water-filling power allocation scheme is used. The advantage of the water-filling scheme is more obvious in the low transmit power range. When the transmit power is high, the difference between the schemes with and without power allocation is negligible.

Fig. 3.7 shows the channel capacity for a 4 × 4 MIMO system. The distance between the transmitter and the receiver is 2 m. In this case, each of the antennas radiates in different directions, making the paths independent of each other. As in Fig. 3.6, the dotted line is the capacity (isotropic antennas, Rx CSI) of a traditional MIMO system with omnidirectional antennas. The spectral efficiency is less than 4 times that of 1 × 1 system (the solid line) [9, p.399]. This is because there are not enough scattered rays between the transmitters and the receivers. As a result, the transmit antennas with limited separation cannot be distinguished by the receive antennas, and the channel matrix $\mathbf{H}$ is ill-conditioned. Compared with the dotted line in Fig. 3.6, we can see that doubling antennas does not double the channel capacity, but only increases it by 1 bit/s/Hz. It indicates that more antennas only provide diversity instead of degrees of freedom if they are too close to each other. The circle line is the capacity of our proposed system with 4 antennas. The capacity is almost 4 times that of 1 × 1 system (the solid line). This means the system can benefit from all the degrees of freedom. The capacity is a little lower than that of the traditional MIMO systems with full scattering [9, Fig. 8.2] as the non-specular reflections can introduce some loss. For other different antenna positions, systems dimensions, and propagation environments, the optimal allocated power and the best antenna configurations can be obtained by solving Eq. (3.8).

3.7 Conclusion

This work has modeled the THz channel considering rough surfaces. With the particular characteristics of the THz channel, we have proposed a new MIMO system with graphene-based directional antennas. Besides, the capacity of the channel has been analysed. In maximizing the capacity, the methods of obtaining the best configuration have been given. We have found that the proposed MIMO system has a higher spectral efficiency than the traditional MIMO systems with omnidirectional metallic antennas. By using the water-filling power allocation scheme, the spectral efficiency increases to an even higher level. The main difficulty in our model is solving the optimization problem considering the limited computing ability of the devices. Therefore, a sub-optimal solution has been presented as a supplement to the optimal one, providing a tradeoff between complexity and accuracy.

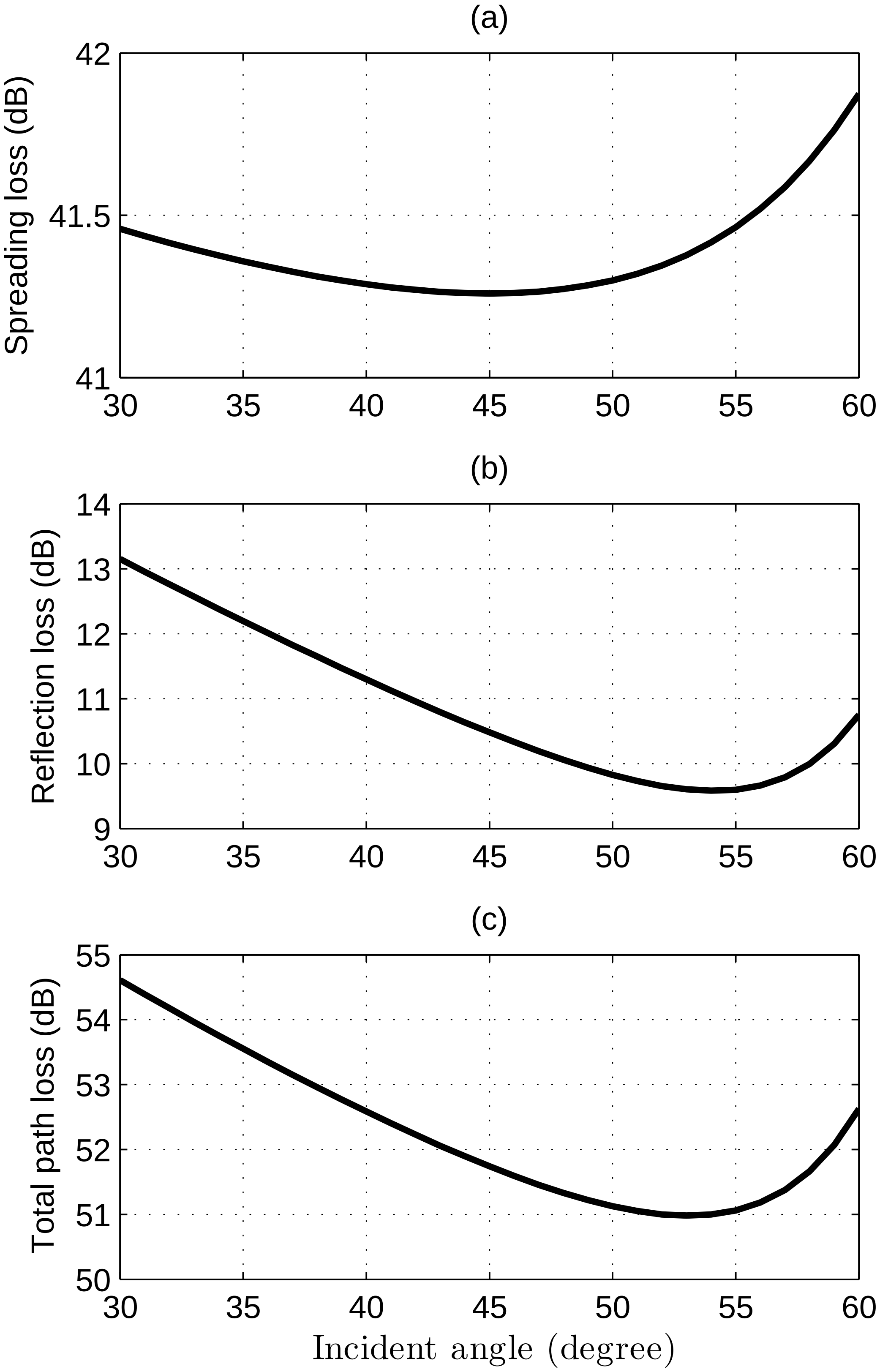

Figure 3.5: Path loss between the 1st transmit antenna and the 1st receive antenna with different incident angles.

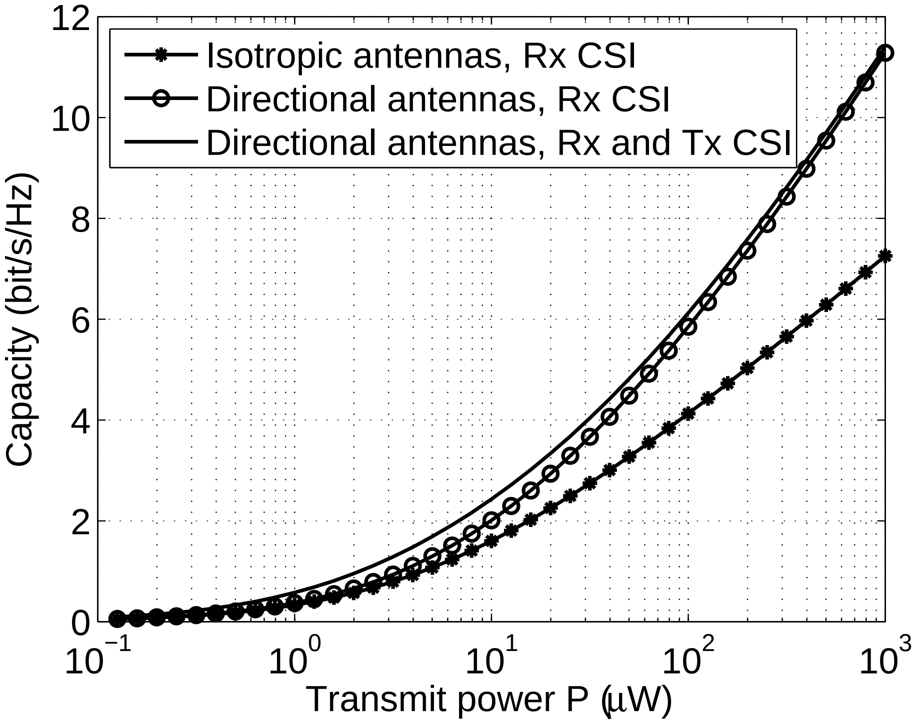

Figure 3.6: Capacity of MIMO systems with a size of 2×2. The noise power is 0.01 nW.

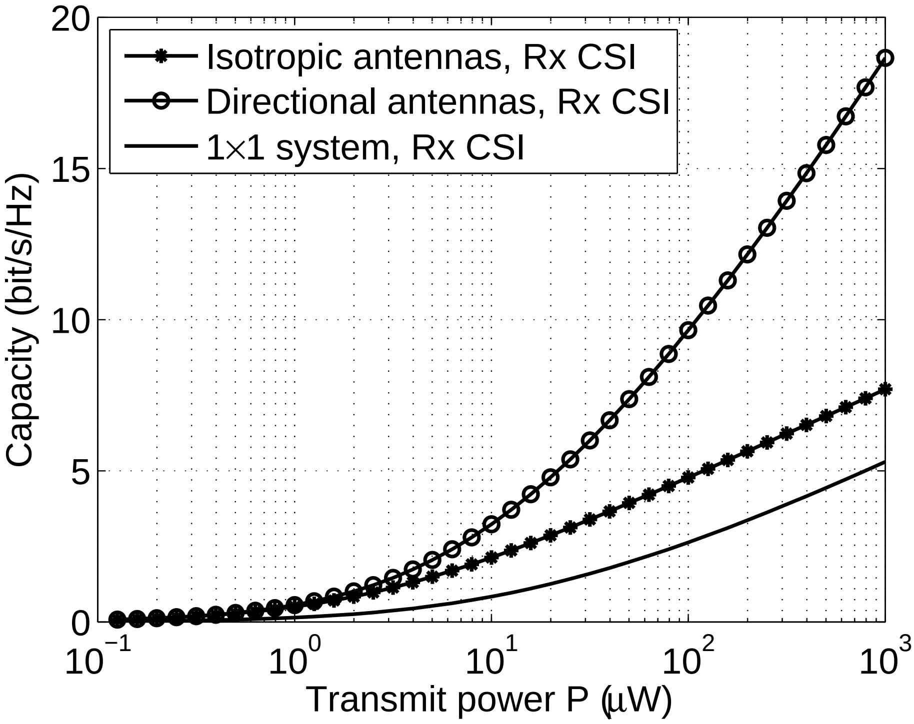

Figure 3.7: Capacity of MIMO systems with a size of 4×4. The noise power is 0.01 nW.

Chapter 4

A Statistical Model for the MIMO Channel with Rough Reflection Surfaces in the THz Band

4.1 Introduction

The THz band (0.1 THz - 10 THz) is one of the most promising bands that will satisfy the demand for higher data rates in wireless communications. It has been shown that about 47 GHz of unregulated bandwidth is available around 350 GHz with low atmospheric absorption [11], and that for short transmission distances, the capacity can even be higher than 1 Tbit/s when the frequency is over 1 THz. When the frequency increases and the devices size scales down, wireless communications will fall into the range of nano-scale communications. Recently, many nano-scale devices have been designed for nanocommunications in the THz band, such as graphene based nano transceivers [52] and antennas [6, 7, 23, 24, 26, 64, 65]. Some nanocommunication THz channel models have been proposed in the literature. For example, reference [42] analyzes the capacity of a THz channel. References [10, 61, 62, 66] review the background knowledge and recent research progress in THz technology, and they reveal that some electrical components for THz frequencies are already commercially available.

On the other hand, the MIMO antenna technique is well known to increase the data rate of a wireless communication system [9]. MIMO theory and precoding schemes in the GHz band have already been well presented in the literature. In a GHz channel, it is usually assumed that the elements of a fading channel matrix $\mathbf{H}$ are independent and identically distributed (i.i.d.), which is based on the assumption of a rich scattering environment that has many multipaths. Under this assumption, the physical channel can be viewed as several parallel sub-channels, and the total capacity scales up linearly with the MIMO dimension. However, for some scenarios in the THz channel and with increasing MIMO dimension, MIMO systems show only beamforming gain but limited multiplexing gain improvement. This is due to the fact that the number of multipaths in the THz channel is limited since the path loss and reflection loss are so large that only the single bounce reflection rays are strong enough to link transmitters with receivers. Therefore, the models of the GHz channel cannot directly be applied to the THz channel, and new models for THz MIMO systems must be developed. It is generally agreed that THz MIMO systems have the following characteristics:

- The scenarios are mainly applied to indoor environments, for example, office buildings or malls [10]. For long distance outdoor communications, smart antennas with high power amplifiers must be applied [11].
- For indoor THz MIMO channels, few multipaths exist between the transmitting and receiving antennas if all the surfaces are smooth [12, 13]. The correlations between the received signals on different receive antennas are significantly higher than those in the GHz band.

Therefore, the multiplexing gain will be low, and correlated signals have low diversity gain. This situation is very similar to the sparse MIMO channel that has been studied in some theoretical investigations [14, 15] as well as in experiments [16].

4.2 Related Work

The THz band is one of the most promising bands that attracts much research interest. References [10, 61, 62, 66] review the background knowledge and recent research progress. Most of the publications are about THz device designs and THz channel modeling. For example, references [6, 7, 23, 24, 26, 52] give some THz antenna designs and concepts based on graphene while [42] analyzes the capacity of the THz channel. As one of the aspects of channel analysis, scattering analysis is much more important than that in the GHz range. In [4, 5, 8, 11–13, 67], the scattering from rough surfaces is thoroughly studied for the THz channel.

4.3 Contributions

Most of the existing works on MIMO system models are in the GHz band and no one studied the differences between the GHz and the THz MIMO. As discussed in Section 4.2, most of the publications in the THz are about devices and channel models, but very few are about THz MIMO systems. In Chapter 3, we have addressed one of the main differences of the reflection characteristics in the THz band. When the carrier frequency is very high, the surfaces of the reflection objects cannot be regarded as smooth surfaces, but must be treated as rough surfaces. For the THz frequency, the surfaces of indoor objects, such as wallpaper, carpet, are all rough enough and the rough scattering cannot be ignored. In [8, 12], the authors studied the scattered power with different reflection angles at 300 GHz. Based on their work, we can investigate the reflection properties at even higher frequency and propose a new MIMO model for the THz frequency. In the new MIMO model, the scattered rays are also considered and become more and more important when the frequency increases. When the frequency is high enough, the specular reflection begins to lose its privileged position and becomes an ordinary ray with very low power gain. With the capacity theories, we can divide the channel capacity into two parts, one is the capacity introduced by the specular reflection, and the other is the capacity introduced by the scattered rays. Thus, our goal is to analyse the relationship between the capacity and the roughness factor, as well as the capacities introduced by different rays. Besides, the final results will also be compared with those in the GHz band. From the comparisons, we will find out whether it is necessary to use multi antennas in the THz band, and the tradeoff between the costs and gains with different rough surfaces. Finally, we will study the precoding schemes for the THz MIMO systems, including baseband precoding design, RF phase shifter, and directional antenna design.

The main contributions of this chapter are summarized as follows:

- We propose a THz MIMO system model based on rough surface reflection theories and point out the importance of rough surfaces to THz MIMO systems.
- We analyse the relationship between the capacity and the roughness factor, as well as the capacities introduced by different rays.
- We compare the results with those in the GHz band. From the comparisons, one can determine whether it is necessary to use multiple antennas in the THz band, and the tradeoff between costs and gains under different roughness scenarios.

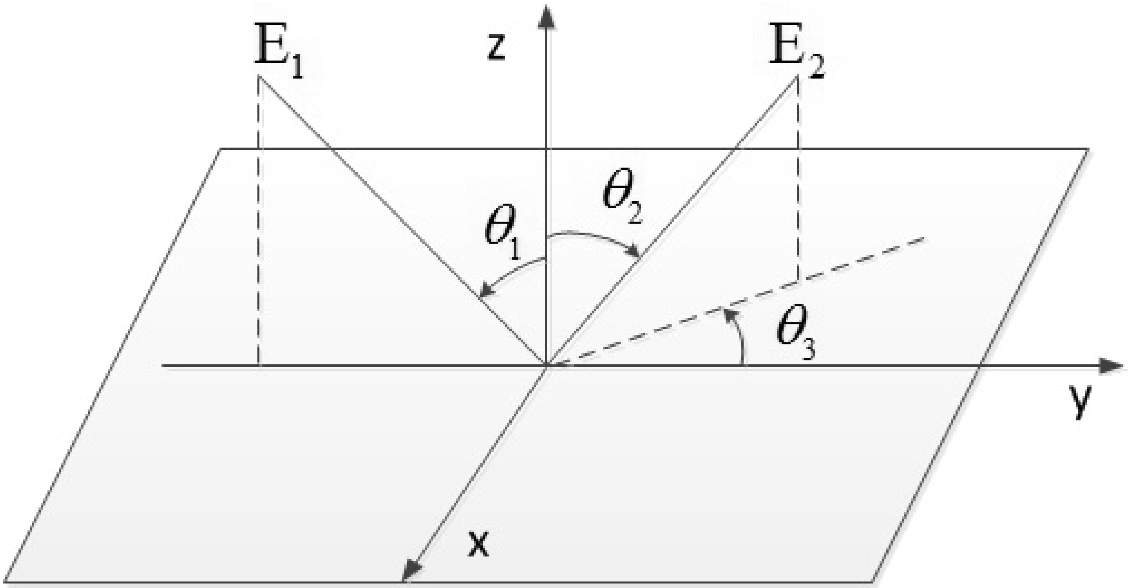

Figure 4.1: The scattering reflection geometry.

4.4 Reflection in the THz band

4.4.1 Scattering from a Small Rough Surface

Reflections in the GHz band seldom consider the surface roughness, and simply treat it as a smooth surface. C. Jansen et. al. [29] measured the roughness of some common indoor materials, such as plaster and wallpaper. Their results show that the deviation of the surface height is about $\sigma_h = 88$ nm for plaster, and $\sigma_h = 90$ nm for wallpaper. Compared with the wavelength of the GHz frequency (e.g., the wavelength is 300 mm for 1 GHz wave), these deviations are rather small, and can be ignored safely. However, for THz frequency waves, the wavelength is on the order of several hundred micrometers, which is comparable to the surface deviation. In such situation, we must take the roughness into consideration and use a new method to model the reflection property.

Suppose the incident field $\mathbf{E}_1$ is a harmonic plane wave of unit amplitude. We denote the angle of incidence (the angle between $\mathbf{E}_1$ and the $\mathbf{z}$ axis) as θ_1 and the angles of reflection (the angles between the reflected field $\mathbf{E}_2$ and the $\mathbf{z}$ and $\mathbf{y}$ axes) as θ_2 and θ_3, respectively (Fig. 4.1). Let $\mathbf{P}$ be the point of observation and r the distance from $\mathbf{P}$ to a point (x, y) on the reflection surface. The scattered field $\mathbf{E}_2$ is given by the Helmholtz integral [3]

$$\mathbf{E}_2(P) = \frac{1}{4\pi}\int\int_S (\mathbf{E}_1\frac{\partial\psi}{\partial\mathbf{n}} - \psi\frac{\partial\mathbf{E}_1}{\partial\mathbf{n}})\mathrm{d}S, \tag{4.1}$$

where S is the reflection surface, $\mathbf{n}$ is a vector normal to the surface, and ψ is a continuous scalar function denoted as

$$\psi = \frac{e^{ik_2 r}}{r} \tag{4.2}$$

where k_2 is the wavenumber of the reflected wave. The scattering coefficient ρ is defined as

$$\rho(\theta_1, \theta_2, \theta_3) = \frac{E_2}{E_{sr}}, \tag{4.3}$$

where E_2 is the amplitude of $\mathbf{E}_2$, and E_{sr} is the field specularly reflected by a smooth and ideally conducting surface.

For a rectangular surface with random height and area of $A = l_x l_y$, the average scattering power coefficient is expressed as [3]

$$< \rho\rho^* >= e^{-g}\rho_0 + \frac{\pi T^2 F^2 e^{-g}}{A} \sum_{m=1}^{\infty} \frac{g^m}{m!m} e^{-v_{xy}^2 T^2/4m}. \tag{4.4}$$

Eq. (4.4) consists of two terms: the first term corresponds to the specular reflection, and the second term corresponds to the scattered field. When the reflection surface becomes rougher, the significance of the second term increases. For Eq. (4.4), $k = \frac{2\pi}{\lambda}$ is the wavenumber, T is the surface correlation length, ρ_0 is the scattering coefficient of a plain surface of area A, g is the Rayleigh roughness factor, and v_x, v_y, v_{xy}, and F are notations used to simplify the expression of Eq. (4.4). These symbols are given by

$$v_x = k(\sin(\theta_1) - \sin(\theta_2)\cos(\theta_3)), \tag{4.5}$$

$$v_y = k(-\sin(\theta_2)\sin(\theta_3)), \tag{4.6}$$

$$v_{xy} = \sqrt{v_x^2 + v_y^2}, \tag{4.7}$$

$$\rho_0 = \mathrm{sinc}(v_x l_x)\mathrm{sinc}(v_y l_y), \tag{4.8}$$

$$g = k^2\sigma_h^2(\cos(\theta_1) + \cos(\theta_2))^2, \tag{4.9}$$

and

$$F = \frac{1 + \cos(\theta_1)\cos(\theta_2) - \sin(\theta_1)\sin(\theta_2)\cos(\theta_3)}{\cos(\theta_1)(\cos(\theta_1) + \cos(\theta_2))}, \tag{4.10}$$

It is evident from Eq. (4.9) that the roughness factor g is dependent on frequency, the surface derivation, the incident angle θ_1 and the angle of reflection θ_2. Fig. 3.1

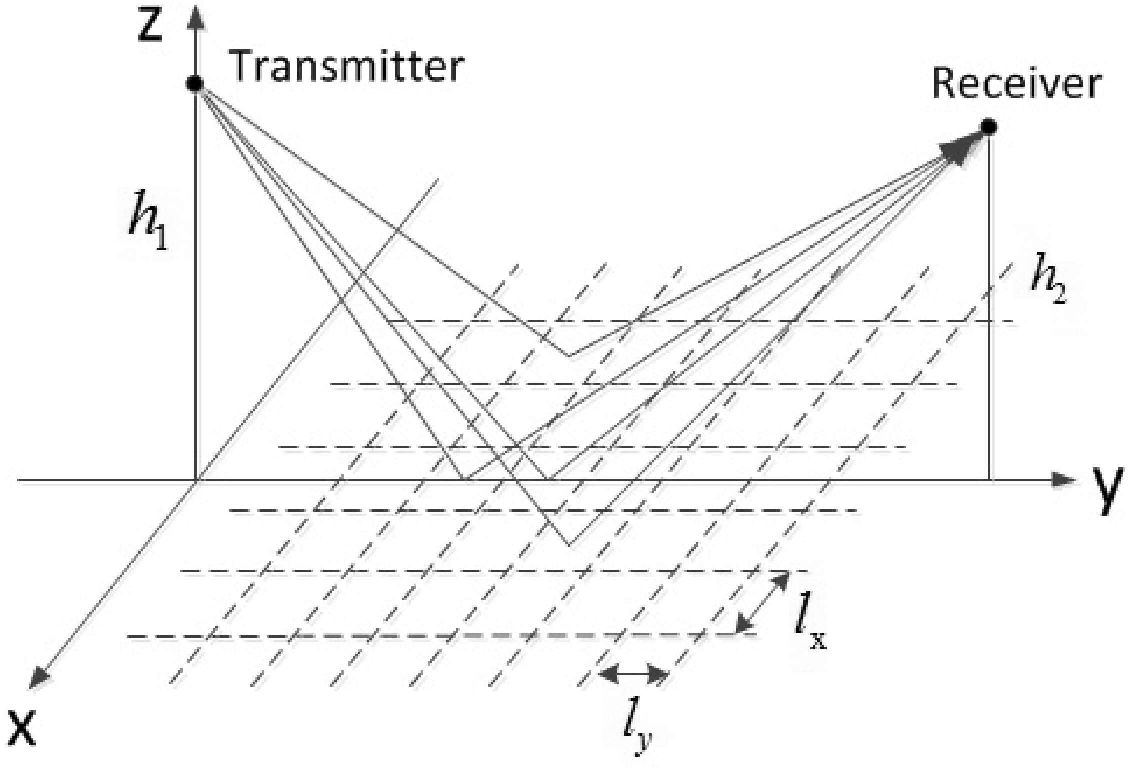

Figure 4.2: The large surface is divided into many small sub-tiles.

shows the reflection patterns of different roughnesses, from a smooth surface ($g = 0$) to a very rough surface ($g \gg 1$).

4.4.2 Scattering from a Large Rough Surface

The discussion in the previous section holds only when the surface area A is small. When the dimensions of the reflecting surface are comparable with the distance between the transmitter and receiver, the total field at **P** is the accumulation of many rays with different angles of reflection. Therefore, treating the surface as a single tile and using a single angle of reflection will introduce tremendous error. To remedy this situation, we use the method presented in [4] and divide the surface into small sub-tiles.

Suppose the surface is in the x-y plane, the transmitter is on the z axis, and the receiver is in the y-z plane, as shown in Fig. 4.2. The entire surface is divided into many sub-tiles of the same size. Each sub-tile has its own incident/reflection angles which can be obtained by geometrical calculations. The scattering coefficient using sub-tiles is shown in Fig. 4.3. Note that the amplitude of each sub-tile is highly correlated with the size of the sub-tile. If we use small sub-tiles, the surface can be divided into even more sub-tiles and the power has a smaller amplitude. Vice versa,

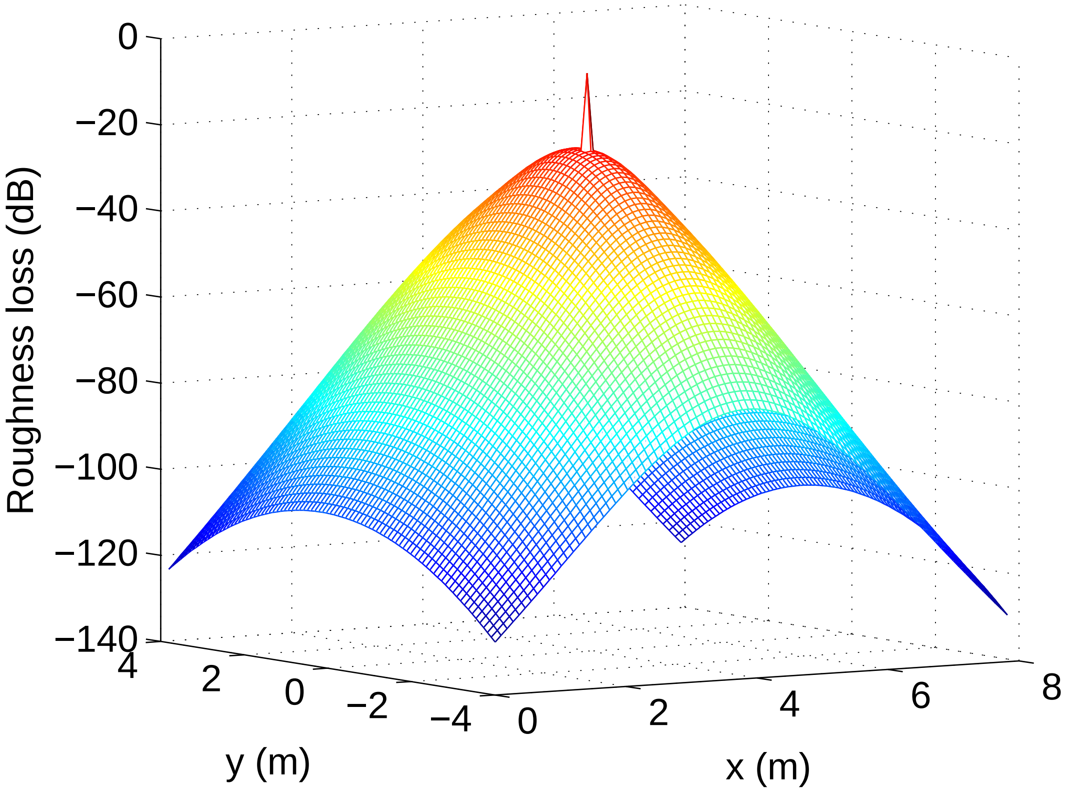

Figure 4.3: The scattering coefficient of a rough surface. The positions of the transmitter and receiver are (0,0,4) and (8,0,4) respectively. The frequency is 300 GHz, $T = 2.3$ mm, $l_x = l_y = 40T$, and $\sigma_h = 0.13$ mm [4, 5].

a larger sub-tile size will result in fewer sub-tiles with larger amplitude. Fig. 4.3 shows the combination effect of the specular term and the diffuse scattering term in Eq. (4.4). The specular term has a very narrow peak around the specular reflection point with a relatively large amplitude. The diffuse scattering terms are much wider around the specular point, but with smaller amplitudes. In our model, the specular reflected power is constant with respect to different division methods. That means that independent of the size of a sub-tile, the specular reflected power and the total scattered power are all constant. The total power arriving at the receiver is the summation of the specular reflection power and the power from all other possible sub-tiles. It is obvious that the size of the sub-tiles only slightly influences the precision of the total power. Fig. 4.4 shows the effect of frequency on the specular and diffuse scattered fields. The figure presents the ratio of the diffuse scattered power to the total received power. The total power is composed of the diffuse scattered power and the specular reflection power. As the frequency increases, the surface changes from smooth to very rough. Then more power is diffuse scattered and the specular reflection power is no longer dominating. As a result, the ratio of

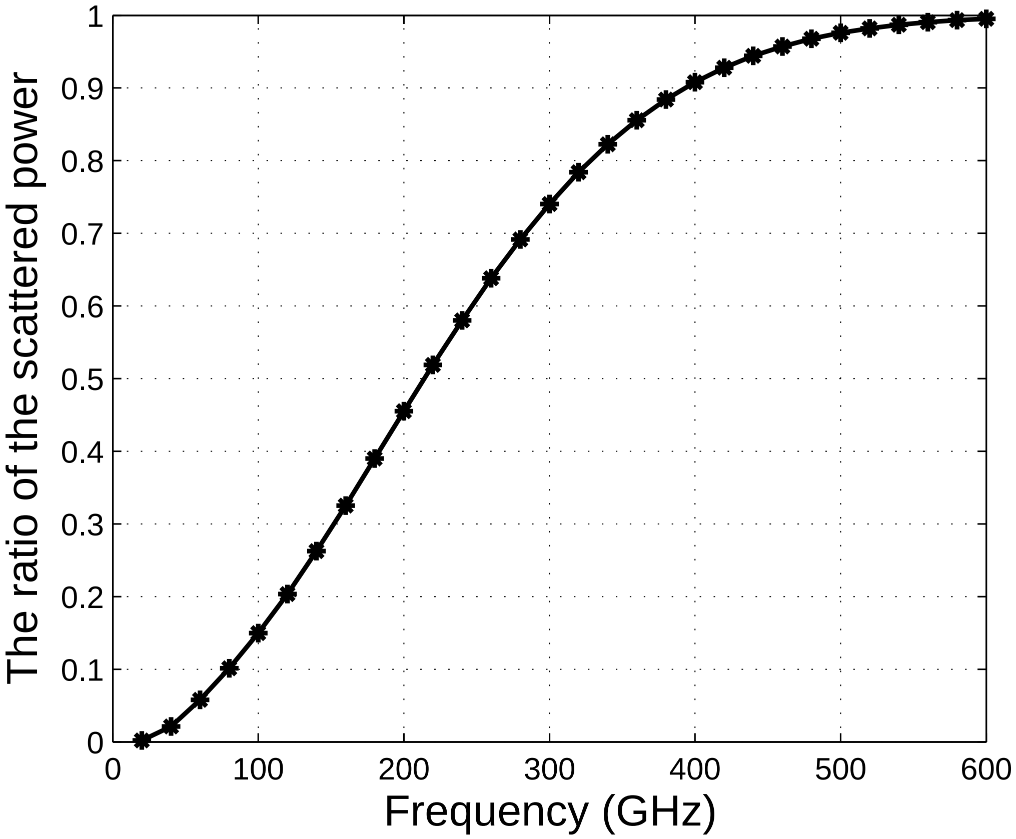

Figure 4.4: The ratio of the scattered power to the total power. The parameters are the same as in Fig. 4.3.

the diffuse scattered power to the total power increases from very low to unity.

4.5 System Model

4.5.1 MIMO Model in the GHz Band

Consider a MIMO system with N_t transmitting antennas and N_r receiving antennas, and suppose that both transmit and receive arrays are uniform linear arrays (ULAs). The channel matrix $\mathbf{H}$ is the summation of N multipaths as shown in Fig. 4.5. The discrete-time response of the channel can be written as

$$\mathbf{H} = \sum_{i=1}^{N} \beta_i \mathbf{e}_r(\Omega_{ri}) \mathbf{e}_t^*(\Omega_{ti}), \tag{4.11}$$

where β_i is the complex gain of the ith path, Ω_{ri} and Ω_{ti} are angles of arrival and departure of the ith path, respectively, $\mathbf{e}_r(\Omega_{ri})$ and $\mathbf{e}_t(\Omega_{ti})$ are the receive and

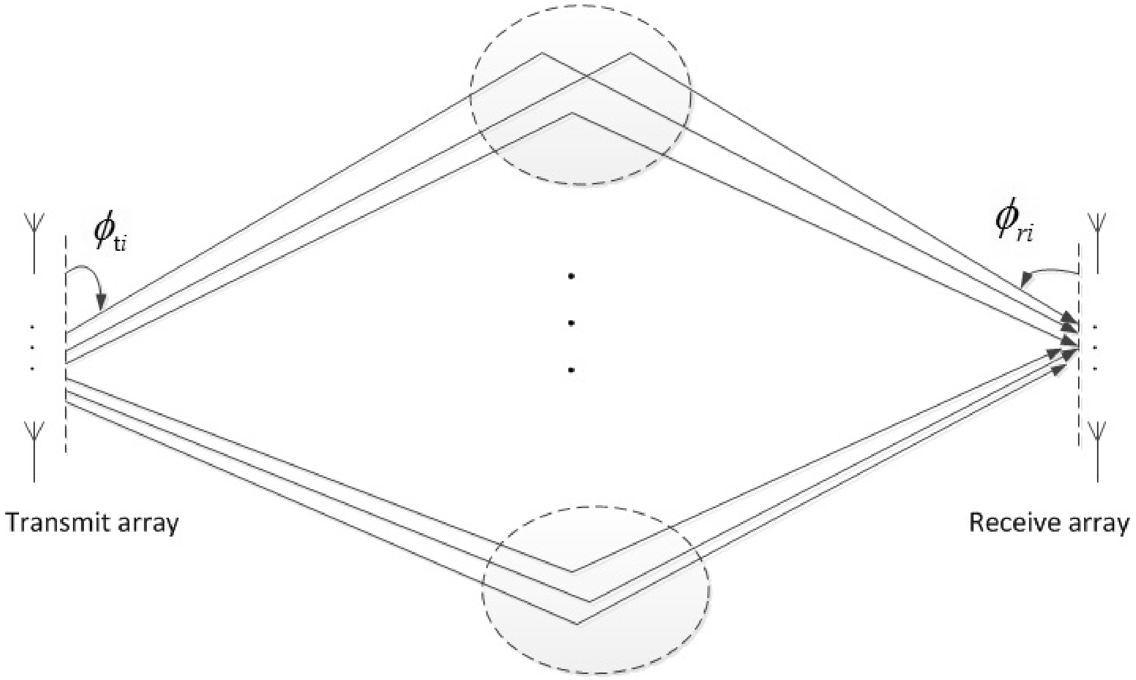

Figure 4.5: MIMO model in a multipath environment.

transmit array response vectors, respectively [9, p.349], and the asterisk denotes conjugate transposed. In a rich scattering environment, many independent rays exist in the channel. Statistically, in the GHz band, the amplitude of each ray is random, and the phase is uniformly distributed between 0 and 2π. Therefore, β_i are i.i.d. complex random variables with zero mean and unit variance. From the structure of $\mathbf{H}$, we know that with only one path (line of sight or a single reflected ray) between the transmitter and the receiver, a MIMO channel provides only a power gain but no degree of freedom gain [9, p.351], because the channel coefficients are highly dependent, and the rank of $\mathbf{H}$ is 1. When multipaths exist, the signals from different paths can be regarded as from virtual "relays" which are geographically far apart. Therefore, a MIMO system can have multiplexing gain when the rays have different departure/arrival angles [9, p.363]. However, the degree of freedom gain cannot exceed the number of multipaths. It is useless to utilize too many antennas if there are not enough scatterers in the channel. In fact, the channel may still be sparse under some conditions even if the MIMO scale is small, e.g., 8×8. Only when the number of multipaths is very large can the channel gains be regarded as Rayleigh distributed random variables. In this situation, the channel's degrees of freedom scale linearly with the channel dimension. In the GHz band, many models adopt this assumption. However, this is not the case in the THz band with smooth surfaces, as the number of multipaths are likely smaller than those in the GHz band.

4.5.2 MIMO Model in the THz Band with Rough Surfaces

For the indoor channel, the multipaths originate from a few clusters, and each cluster is composed of many scattered rays. Based on the work of Saleh and Valenzuela [68], we propose a MIMO model in the THz band with rough surfaces. In this model, we assume the walls, ceiling, floor, and large surfaces of furniture to be reflection surfaces. For the THz band, the number of clusters is usually small due to high path loss. As discussed in the previous section, each large surface results in many scattered sub-rays around the specular reflection point. The exact number of sub-rays is determined by the geometry of the room, the positions of antennas and the roughness of the surfaces. The impulse response of the THz channel can be written as

$$h(t) = \sum_{l=1}^{N_C} \sum_{k=1}^{N_L} \beta_{lk} \delta(t - T_l - \tau_{lk}), \tag{4.12}$$

where l represents the cluster number, k represents the sub-ray number in the cluster, and β_{lk} is the amplitude of each ray. T_l is the time delay of the lth cluster and τ_{lk} is the time delay of the kth ray in the lth cluster. In [13], the authors obtain the angular power profile by the ray-tracing method and experiments. Both results show that there are six main clusters and each of them has hundreds of multipaths, which validates our aforementioned statements.

Next we will determine the properties of clusters and sub-rays. In this work, we assume the indoor scenario to be the same as in [13], using some large flat surfaces (walls or furniture) which act as reflection surfaces. On each large surface, a cluster of rays exist around the specular reflection point [13]. Note that in some other scenarios, for one reflection surface, the specular reflection ray might not exist and only diffuse scattering components are received. In our scenario, the angles of arrival/departure, the time of arrival and the normalized amplitude of each cluster in the THz band have the same distribution (normalized to the large scale fading path loss) as those at GHz frequencies. Unlike the statistical distribution of sub-rays in the GHz band, the sub-rays in each cluster at THz frequencies are determined, and can be obtained from the surface roughness theory. Here, we use the results in [69]. The amplitudes of the N_C first sub-rays in the N_C clusters follow the Rayleigh distribution, with a mean square value

$$\overline{\beta_{l0}^2} = \overline{\beta_{00}^2} e^{-T_l/\Gamma}, \tag{4.13}$$

where $\overline{\beta_{00}^2}$ is the mean power of the first ray in the first cluster, and Γ is the cluster decay parameter. As discussed in Section II, the first sub-ray in each cluster is usually the ray with the largest power. For our indoor scenario, the specular reflection ray is the first sub-ray. We have not taken into consideration clusters without specular reflection rays as their power is very small. Note that $\overline{\beta_{l0}^2}$ is the power without considering the scattering coefficient. For a rough surface, the power of each sub-ray in the cluster can be obtained by multiplying each scattering coefficient with the first sub-ray. Mathematically, the power of the sub-rays is denoted as

$$\overline{\beta_{lk}^2} = \overline{\beta_{l0}^2} < \rho\rho^* >_{lk} = \overline{\beta_{00}^2} e^{-T_l/\Gamma} < \rho\rho^* >_{lk}, \tag{4.14}$$

where $< \rho\rho^* >_{lk}$ is the average scattering power coefficient of the kth sub-ray in the lth cluster. In [4], the measured results coincide with the simulation results which validates the suitability of using a rough surface scattering model to obtain sub-rays in each cluster.

For the angles of arrival/departure of the clusters, a uniform distribution on the interval $[0, 2\pi)$ is a good fit for experimental results [69]. This also coincides with our intuition, as the reflection surface can be any part of the surface of a room. The ray angles within a cluster are not random. As shown in Fig. 4.2, the sub-rays all originate from the small sub-tiles, thus the angle of each sub-ray within a cluster is deterministic. Once the geometry is determined, the angles of arrival/departure can be calculated by the ray-tracing method. In fact, as we only consider single bounce rays, the angles of arrival are not independent of the angles of departure.

The time of arrival of clusters is described by a Poisson process. The distribution of the arrival time is given by

$$p(T_l|T_{l-1}) = \Lambda e^{-\Lambda(T_l - T_{l-1})}, \tag{4.15}$$

where Λ is the cluster arrival rate. The time of arrival of rays in each cluster can also be obtained by calculation. Therefore, τ_{kl} is fixed by the geometry of each ray.

The channel matrix $\mathbf{H}$ for the THz band has a form similar to Eq. (4.11), whose baseband equivalent model is written as

$$\mathbf{H} = \sum_{l=1}^{N_c} \sum_{k=1}^{N_l} \hat{\beta}_{lk} \mathbf{e}_r(\Omega_{rlk}) \mathbf{e}_t^*(\Omega_{tlk}). \tag{4.16}$$

where $\hat{\beta}_{lk}$ is the complex gain of the kth path in the lth cluster. The phase of $\hat{\beta}_{lk}$ is uniformly distributed between $[0, 2\pi)$, and the amplitude follows a Rayleigh distribution with a mean value of $\bar{\beta}_{lk}$. Note that the rays belong to several clusters, and the number of sub-rays in each cluster might not be the same. Based on this discussion, we reach the conclusion that the number of multipaths will influence the randomness of the channel matrix $\mathbf{H}$. When we have only a few clusters and each surface is smooth, there will be only a few rays, which results in the columns of $\mathbf{H}$ to be highly correlated.

4.5.3 The Capacity of the MIMO Channel in the THz Band

The ergodic MIMO capacity is given by the following well-known formula

$$C = \mathbf{E}[\sum_{i=1}^{n_{min}} \log_2(1 + \frac{P_i \lambda_i^2}{N_0})] \text{ b/s/Hz}, \tag{4.17}$$

where $\mathbf{E}[\cdot]$ is the expectation, n_{min} is the rank of the random matrix $\mathbf{H}$, P_i is the transmit power of the ith stream, N_0 is the noise power spectral density, and $\lambda_1, \lambda_2, \cdots, \lambda_{n_{min}}$ are the singular values of the random channel matrix $\mathbf{H}$. The capacity is influenced by the specular reflection ray and the scattered rays. When the surfaces are very smooth, the model reduces to that of GHz MIMO. In our model, there are fewer rays if the surfaces are very smooth, but the number of rays increases with surface roughness. Next we will analyze the MIMO capacity in the angular domain based on the work of Sayeed *et. al.* [70–72].

Suppose all antennas are critically spaced at half the wavelength ($\Delta = 0.5$, where Δ is the receive antenna separation normalized to the carrier wavelength), $L_t = N_t\Delta$ and $L_r = N_r\Delta$ are the normalized lengths of the transmit and receive antenna arrays, respectively. From [9] we know that the system of N_r fixed vectors

$$\{\mathbf{e_r}(0), \mathbf{e_r}(\frac{1}{L_r}), \cdots, \mathbf{e_r}(\frac{N_r - 1}{L_r})\}, \tag{4.18}$$

can be one of the orthonormal basis sets for the received signal space. As the transmit antenna array has the same structure as the receive antenna array, the basis for the transmit signal space has exactly the same structure. Transforming the signals in the spatial domain into the angular domain, we can obtain the equivalent representation of the channel in the angular domain [9, p.370]

$$\mathbf{H^a} = \mathbf{U_r^* H U_t}, \tag{4.19}$$

where $\mathbf{U_r}$ and $\mathbf{U_t}$ are the base of the received and transmit signal spaces taking the form of Eq. (4.18), with dimensions of $N_r \times N_r$ and $N_t \times N_t$, respectively.

Based on the previous discussion, we partition the physical paths into $L_r \times L_t$ resolvable bins, each with an angular width $\frac{1}{L_r} \times \frac{1}{L_t}$, as shown in Fig. 4.6. We project each ray into the angle lattice, and the results reveal the quality of the channel.

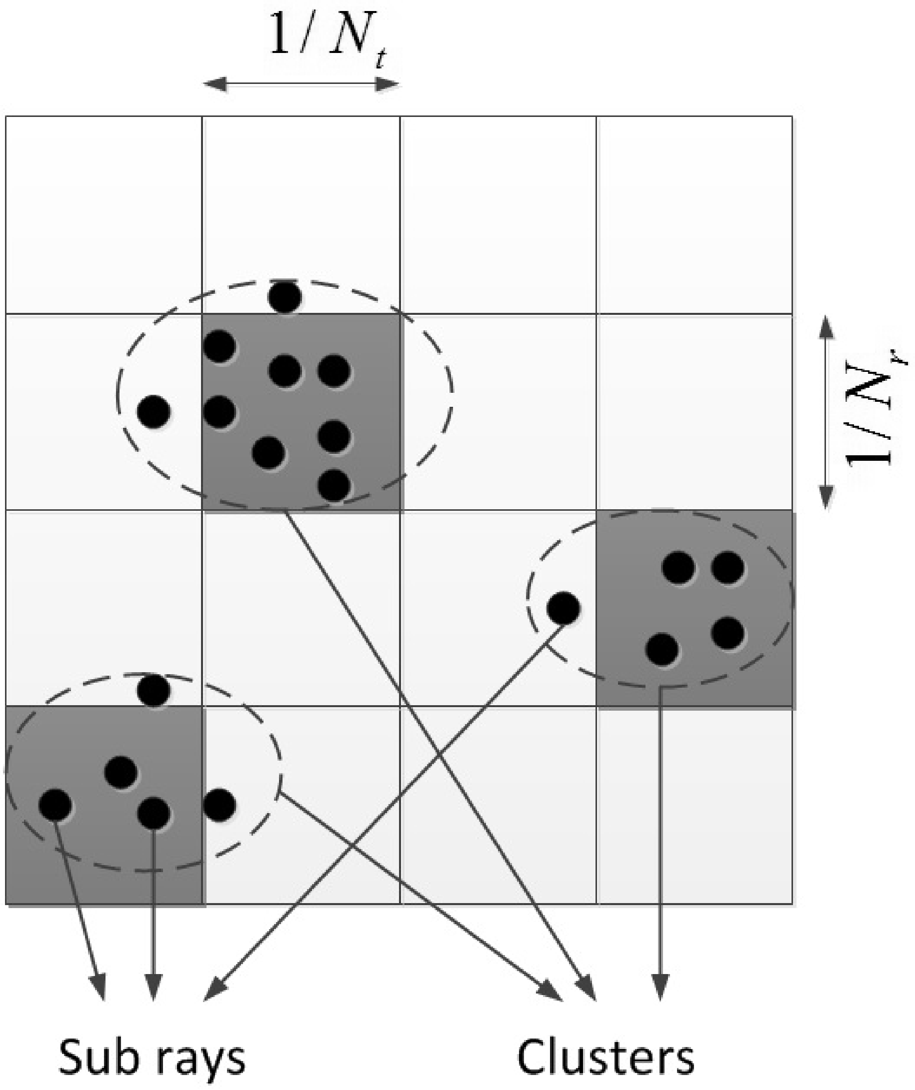

Figure 4.6: Angular domain representation of the channel. Each square represents a resolution bin with a width of $1/L_r \times 1/L_t$. The shaded squares are the clusters and the dots are the sub-rays.

For example, in [13], the authors measure the relative received power of different angles of arrival/departure reflected from moderately rough surfaces ($\sigma_h = 0.15$ mm and $f = 300$ GHz). Their figures show that there are several clusters randomly distributed on the lattice, and each cluster has a narrow angle spread. By observing the lattice structure (Fig. 4.6), we comment as follows:

- The amount of diversity equals the number of non-zero entries in the lattice, and the amount of degrees of freedom equals the amount of different angles. Since the THz MIMO channel in smooth surface (or slightly rough) environments usually has few clusters with narrow beams, both the diversity gain and the multiplexing gain are small, which results in a sparse MIMO channel. However, small scale MIMO systems usually have a full multiplexing gain.

- When the surfaces are rough, the beam reflected from one surface grows wider, and more resolution bins have sub-rays. Therefore, the rougher the surfaces, the more degrees of freedom the channel has. This will be shown in Fig. 4.7 in the result Section.
- The channel capacity of the MIMO system can be divided into two parts: one is for the specular, the other for scattering reflections. With the increase of surface roughness, the specular capacity will decrease while the scattering capacity will increase.
- The roughness of a surface can play a positive role in increasing the MIMO capacity in the THz band. When the surface is very smooth, there only exist few very strong specular reflection rays. A rough surface gives rise to many scattered rays in addition to the specular reflected rays. The power of each ray (specular or scattered) is smaller for rough surfaces than for smooth ones, yet the number of rays is much higher. As the multiplexing gain depends primarily on the angular spreads (the number of multipaths), and the power gain depends on the connectivity between the transmitting and receiving antennas (the power of rays), the roughness factor reduces the power gain but increases the multiplexing gain. Therefore, there may exist a tradeoff between the capacity and surface roughness.
- The surface roughness is especially essential for massive MIMO systems in the THz band. As the MIMO scale is extremely large and each resolvable bin is very narrow, only a few bins are non-zero if the surfaces are smooth. Therefore, the benefits of massive MIMO can be realized only with rough surfaces.

4.6 Results

In this section, we first study the distribution of the rays in clusters via Monte Carlo methods. Then we numerically evaluate the channel capacity with different roughness factors. Finally, the effect of different MIMO scales is analyzed.

4.6.1 Power Distribution in the Angular Domain

In our simulations, we set the frequency to $f = 300$ GHz and select $\gamma = 20$ ns, $\Gamma = 60$ ns, and $\Lambda = 20$ ns. The distance between the transmitter and receiver is $r = 20$ m. The experimental results in [13] show that there are only 6-8 clusters in one simply decorated room. Therefore, we set the number of clusters as $N_c = 6$. In each cluster, we assume that the first sub-ray is the specular reflection ray which is reasonable for an indoor scenario [13]. The height deviations of the surfaces are $\sigma_h = 0.03$, 0.13 and 0.23 mm, and $l_x = l_y = 10T$ to get a higher precision. $T = 2.3$ mm, and $\sigma_h = 0.13$ mm are the parameters used in Fig. 4.3. The procedure of generating clusters is the same as in [69]. Once the clusters are determined, the sub-rays are generated by geometrical calculations.

Fig. 4.7(a) shows the power distribution in the angular domain with a surface height deviation of $\sigma_h = 0.03$ mm (g is in the order of 0.1). The MIMO scale is 64×64, and each dot represents one of the 4096 bins. This slight roughness can scatter the rays only in a narrow angle, and the specular reflection ray carries significantly higher power than the scattered rays. This coincides with our conclusion in Section III-C. When the roughness increases to $\sigma_h = 0.13$ mm (g is in the order of 1) and $\sigma_h = 0.23$ mm (g is in the order of 10), the number of non-zero dots becomes larger while the amplitude of each ray reduces, as shown in Fig. 4.7(b) and (c).

4.6.2 Channel Capacity Analysis

The channel capacity for a 4×4 MIMO system with different surface roughness is shown in Fig. 4.8. Other parameters are as in Fig. 4.7. The solid line, which is used as a benchmark, shows the spectral efficiency of a MIMO system with ideally smooth reflection surfaces. It is obtained by setting the roughness factor to zero while other parameters remain unchanged. The result agrees with that in [9, p.400]. The dashed line shows the spectral efficiency of a system with the surface height deviation of $\sigma_h = 0.03$ mm. The result is close to that with smooth surfaces. When the roughness increases to $\sigma_h = 0.13$ and $\sigma_h = 0.23$, the spectral efficiency is shown by the lines with circles and stars, respectively. Since the MIMO scale is relatively small, six clusters can provide full degrees of freedom; the spectral efficiency with rough surfaces is only slightly larger than that with smooth ones. Therefore, we can conclude that the roughness has little influence on the capacity of small scale MIMO systems in the THz band.

When the MIMO scale is large, however, we encounter a sparse fading channel due to the small number of clusters. Fig. 4.9 shows the capacity of a 64×64 MIMO system with other parameters is as in Fig. 4.8. Comparing the two solid lines in Fig. 4.9 and Fig. 4.8, we observe that more antennas contribute to a relatively small capacity increase in smooth environments. However, the capacity increase is obvious even when the surfaces are only slightly rough ($\sigma_h = 0.03$). When $\sigma_h = 0.13$ (the surface height deviation of some common materials are in this order), the capacity can be as high as 4-5 times of that with a smooth surface. If we further increase the roughness, the capacity continues to increase. This implies that rough surfaces are important in enlarging the capacity of large scale MIMO systems.

As discussed in Section II, the roughness factor g is controlled by the deviation of surfaces σ_h, the incident/reflected angles and the frequency f. For the same surface, g quadratically increases with f according to Eq. (4.9). In the above simulations, we fixed the frequency at 300 GHz and obtained different results by varying σ_h. Obviously, once the environment is determined, different frequencies can introduce different spectral efficiency. Without considering large-scale fading, we can conclude from Fig. 4.9 that a higher frequency will result in higher spectral efficiency for large scale MIMO systems.

4.6.3 The Importance of the MIMO Scale

In this section, we analyze the significance of the MIMO scale. We examine two groups: an $N \times N$ and an $8 \times N$ scale. Other parameters are as in Fig. 4.7. In each group, the surface height deviation increases from ideally smooth to very rough. The spectral efficiency versus the MIMO scale N is shown in Fig. 4.10. The squared solid line shows the spectral efficiency with a very rough surface ($\sigma_h = 0.23$ mm). The line is almost linear which indicates that more antennas introduce higher degrees of freedom. When the surface is slightly rough ($\sigma_h = 0.03$ mm), the line is also linear with N but with a gentler slope, as shown by the diamond solid line. This means that only a portion of degrees of freedom is used under this scenario. The result for an ideally smooth surface is shown by the circled solid line. The spectral efficiency increases very slowly with the increase of N. For comparison, the dashed lines show the spectral efficiencies of the $8 \times N$ system. No matter how rough the surface is, the spectral efficiency increases only slowly with N. Note that, when the surface is ideally smooth, $N \times N$ and $8 \times N$ systems have almost the same spectral efficiency, which means that multiple antennas only provide power gain. Therefore, we can conclude that more transmitting antennas do not introduce multiplexing but only power gain when the surfaces are very smooth. Only with rough surfaces can we obtain the benefits from large scale MIMO systems.

4.7 Conclusion

A new MIMO system model for THz and nanocommunications is proposed that includes the effects of rough reflection surfaces. The results show that the MIMO channel in the THz band is very sparse if the reflecting surfaces are ideally smooth, and that with the increase of the MIMO scale, the sparsity becomes even more severe. When the surfaces are rough, the spectral efficiency of the MIMO system is higher than that with smooth surfaces, which is more pronounced with a larger MIMO scale. We show that surface roughness has a positive effect on increasing the spectral efficiency. Finally, numerical results reveal when it is necessary to use a large MIMO scale in the THz band. We hope that the results presented in this chapter will aid future implementations of nanocommunication systems.

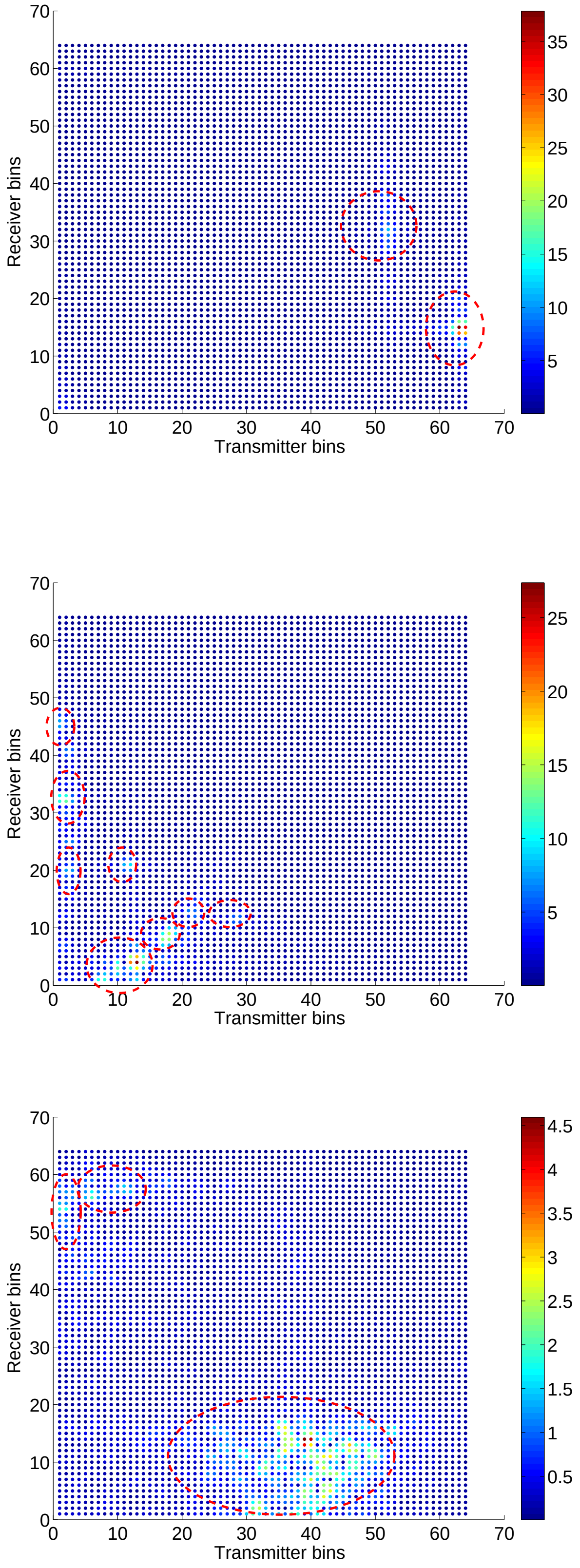

Figure 4.7: Channel matrix in angular domain, with (a) $\sigma_h = 0.03$ mm, (b) $\sigma_h = 0.13$ mm, and (c) $\sigma_h = 0.23$ mm.

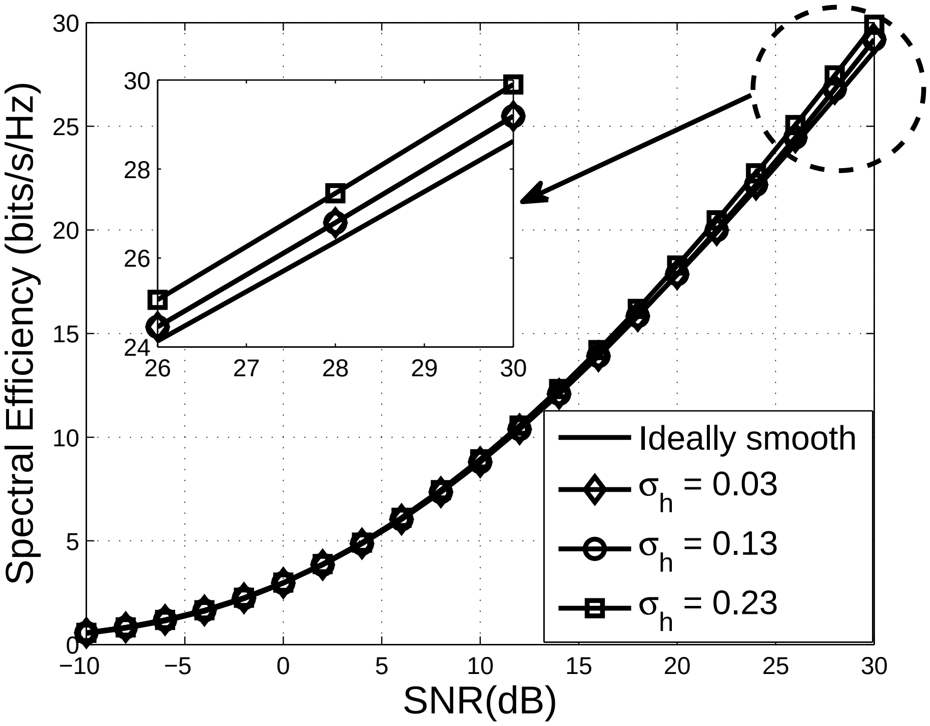

Figure 4.8: The spectral efficiency of the 4 × 4 MIMO system. The parameters are the same as those in Fig. 4.3, with $\sigma_h = 0.03$, 0.13 and 0.23, respectively.

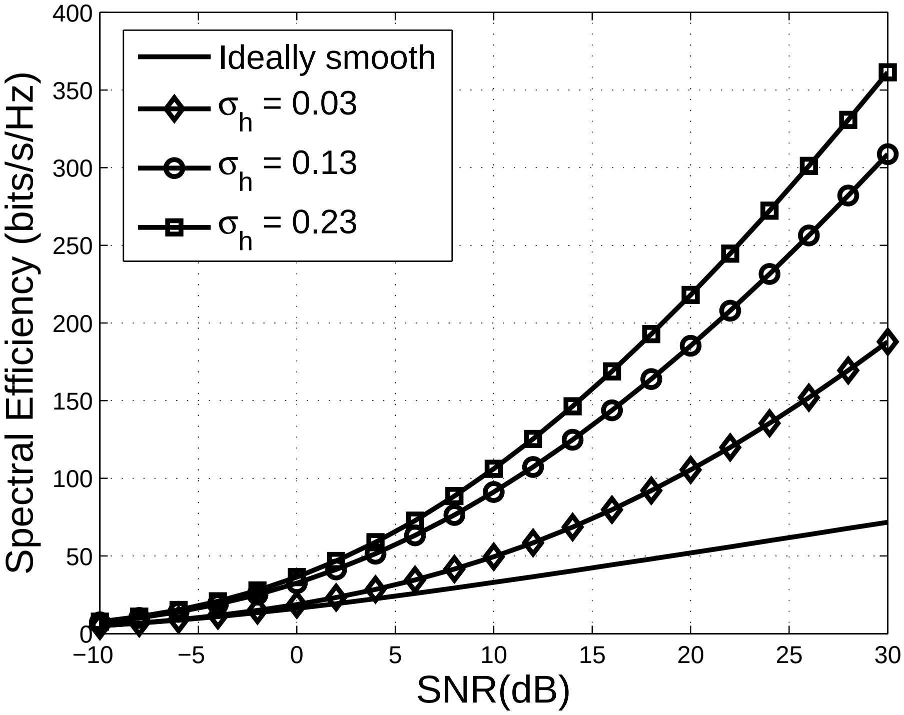

Figure 4.9: The spectral efficiency of the 64 × 64 MIMO system. The parameters are the same as those in Fig. 4.3, with $\sigma_h = 0.03$, 0.13 and 0.23.

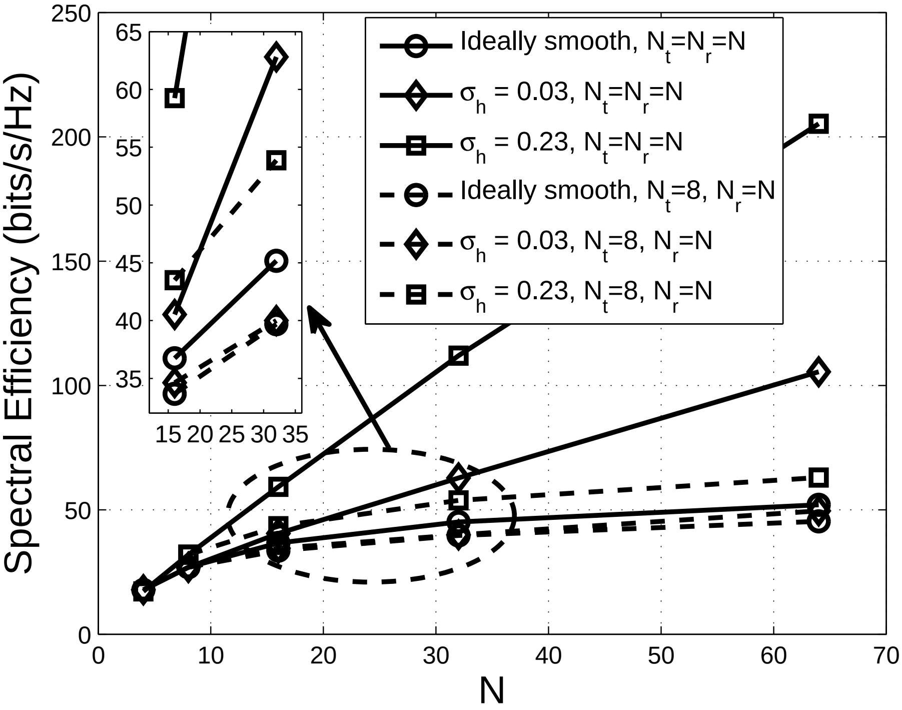

Figure 4.10: The spectral efficiency of different MIMO scales. The SNR is 20 dB and the other parameters are the same as those in Fig. 4.3, with $\sigma_h = 0$, 0.03 and 0.23.

Chapter 5

Performance of Distributed Antenna Systems in the THz Band for Indoor Communications

5.1 Introduction

To relieve the high path loss problem and increase channel capacities, many antenna designs and channel models are proposed in the literature. For example, innovative THz antennas are designed with graphene in [24]. Graphene based antennas have a much smaller size than traditional metallic antennas, which means more antennas can be placed on the same antenna array and higher capacity can be achieved. Besides, directional antennas can be used to increase the received power [65]. The other factor that influences the capacity is the multipath phenomenon. Reference [8] models and verifies reflection characteristics in the THz. The author's results show that the reflection results in a cluster of sub rays around the specular reflection point. References [11–13] study the THz channel model of indoor environments with experiments, and their experiments find that there are very limited clusters of multipaths, and the outage probability due to blockage and less multipath is high.

With an aim of covering the dead spots in indoor wireless communication systems, distributed antenna systems (DAS) are considered as one of the promising architectures for future wireless communications. A basic architecture of DAS is shown in Fig. 5.1. The BS is with a central antenna unit (CAU) and $N_u - 1$ distributed antenna units (DAU). $N_u - 1$ distributed antenna units are all connected to the central antenna unit via wires. When implemented in cellular networks, they can not only improve cell coverage, but also improve the spectral efficiency and

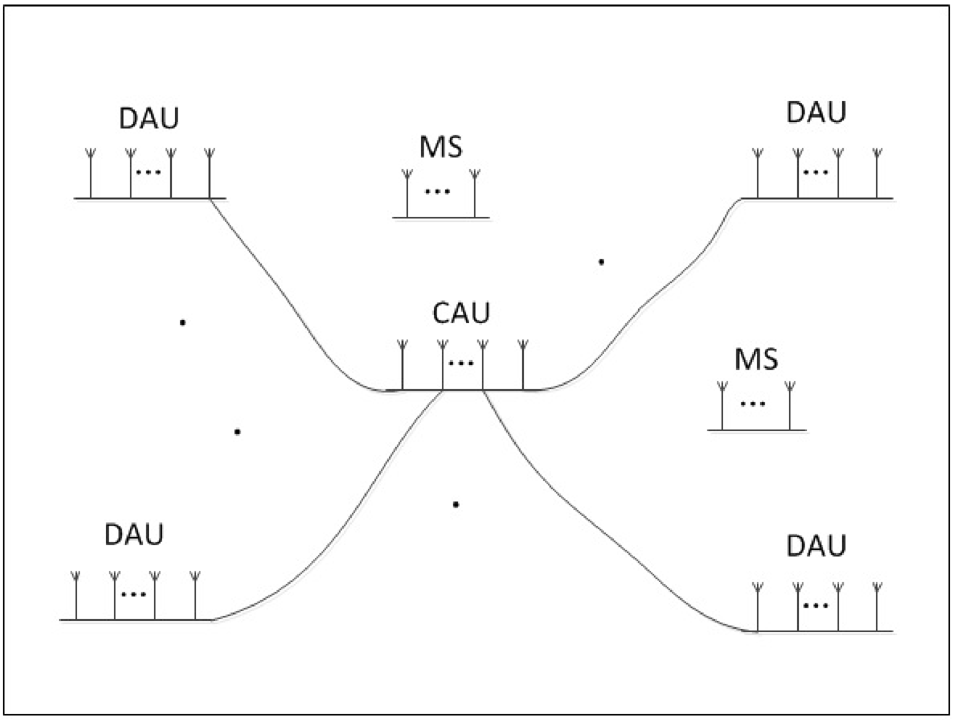

Figure 5.1: A distributed antennas system structure in the indoor environment.

power efficiency [73]. In DAS, the basic idea is to divide centralized antennas into distributed antennas modules. One of the modules plays the role of central unit and all other distributed antenna modules are physically connected to the central unit. Different from centralized antenna systems, DAS has a short distance between user equipment (UE) and base station (BS) (as antennas are evenly distributed in the cell). Therefore, it can mitigate shadowing effects and path loss, and can reduce the interference by minimizing the transmit power.

5.2 Related Work

Saleh et. al. proposed the first distributed antenna systems in 1987. In recent years, distributed antenna systems have attracted much attention due to their ability to satisfy the capacity demand of future wireless communication networks. Soon after the invention, the idea was used in cellular networks to improve cell coverage [74–77]. Besides that benefit, other advantages such as increasing the capacity by reducing transmit power and co-channel interference, and reducing the access distance are also studied in recent work [78–81]. The spectral efficiency of DAS has been studied in [82]. References [83] and [84] give very detailed analyses for multi-cell environments.

5.3 Contributions

As a efficient solution of solving the coverage problem, we apply DAS in THz indoor communications. In this chapter, we analyze the performance of DAS in the THz band for indoor communications. For the GHz DAS, the traditional channel models all include a large scale fading model and a Rayleigh fading model. However, this is not the case in the THz channel. As the number of multipaths is very limited in the THz band, we cannot simply assume that the small scale fading is a Rayleigh distribution. We fully consider the number of multipaths and propose a model suitable for THz DAS. The main contributions of this chapter are summarized as follows:

- We first model the DAS in the THz frequency, which has fewer multipaths than in the GHz band. To the best of our knowledge, no one has studied the performance of the THz DAS before.
- We analyze the characteristics of the DAS channel and point out that the channel is very sparse if the number of antennas on the BS is very large. Besides, we provide the reason for the fact that DAS can have a larger number of degrees of freedom.
- We compare the capacity of MIMO systems with DAS and without DAS. The results show that for the THz channel, increasing the number of antenna units (AUs) is much more important that increasing the number of antennas in one AU.
- We propose an antenna selection scheme which has a very low complexity.

5.4 System Model

5.4.1 The THz Channel

The THz band comprises frequencies between 300 GHz and 10 THz. As the free space attenuation is proportional to the square of the wavelength, THz propagating waves suffer a severe path loss compared to GHz waves. In theory, THz waves have at least 60 dB higher path loss than GHz waves. However, this attenuation level is not a problem for indoor short range communications. For example, the attenuation is only about 0.1 dB at 300 GHz when the transmission distance is less than 1 meter, which can be neglected [83]. Another path loss is due to molecular absorption. Different kinds of molecules and concentrations can introduce various absorbtion loss. The absorption from one kind of molecule spreads over a range of frequencies and leaves thousands of windows [42]. This is one of the main different characteristics from those in the GHz channel, in which molecular absorbtion loss is slight and can be safely ignored. Although the absorbtion loss is very high, however, when it comes to indoor communications, in which the transmission distance is only several meters, and the humidity of water is usually very constant, there exist some transmission windows where the absorbtion loss is lower and can be used for communications [42].

Besides the differences in path loss, reflections are also different from those in the GHz band. As the wavelength of the THz wave can be in the same order of the deviations of reflection surfaces' heights, reflections cannot be treated simply as specular reflections. When the surface is rough, the specular reflection is the same as that in the GHz, but with a relatively larger roughness factor, and reflections from other directions cannot be ignored anymore. In some extreme cases, when the surfaces are very rough, the specular ray may lose its privileged position and be even weaker than other rays. In this situation, even if the incident ray is very narrow, the reflection beam can be wide and radiate in all directions [65].

To compensate for all the above mentioned path losses, using directional antennas can be one of the promising approaches. A high gain directional antenna cannot only increase the received power, but also can dynamically choose the best radiation rays and avoid signal interference [65]. The received power P_r at the receiver is given by

$$P_r = P_t + G_t + G_r + 20\log(\frac{\lambda_c}{4\pi d}) - a(f,c) \cdot d - \alpha \cdot L_r, \tag{5.1}$$

where P_t is the transmitting power, G_t and G_r are antenna gains of the transmitting and receiving antennas, d is the distance, and λ is the wavelength. $a(f,c)$ is the atmospheric attenuation determined by frequency f and molecular concentration c, L_r is the reflection loss, $\alpha = 0$ when the ray is LOS and $\alpha = 1$ when the ray is NLOS.

For the indoor environment, the channel model can be derived from the work of Saleh and Valenzuela [68]. There are a few clusters and many sub multipaths in each cluster. The impulse response of the channel is written as

$$h(t) = \sum_{l}^{N_c} \sum_{k}^{N_s} \beta_{lk} \delta(t - T_l - \tau_{kl}), \tag{5.2}$$

where l represents the cluster number, k represents the sub-ray number in a cluster, and β_{kl} is the amplitude of each ray. T_l is the time delay of the lth cluster, and τ_{kl} is the time delay of the kth ray in the lth cluster. In [13], it was shown by experimental results that there are very limited numbers of clusters in indoor environments in the THz band. This is because the path loss of multi-bounce reflections of THz waves is so high that only LOS path and one-bounce reflections can be received at the receiver. Usually the multipaths in the THz may come from the LOS path and the paths reflected by ceiling, ground, walls, and furniture. Within a cluster, the number of sub-rays is highly correlated to the roughness of the reflection surface. When the surface is smooth, only the specular reflection exists. When the surface is rough, there are several multipaths in the cluster. However, the width of each cluster is usually narrow in the THz range. The beamwidths in some clusters are less than 10°, which results in only one effective path in these clusters.

5.4.2 Distributed Antenna Systems Architecture

Consider the architecture shown in Fig. 5.1. We assume that the capacity of the wires connecting these antenna units are very large and treat it as infinity. There are also k mobile stations (MS), each with N_r antennas. The room is a typical office room with desks and cabinets, and the dimension is 20 m×20 m. Usually all antenna units should be placed evenly in the whole room, as they can cover all the area of the room without any dead spots. In practice, we can modify positions of the antenna units according to the layout of the room. Each antenna unit is an array with N_t antennas. All the antennas are THz antennas with very small size, and the size could be even smaller if novel materials, such as graphene or carbon nanotubes are used [64, 65]. We set the antenna separation on each antenna unit as half a wavelength. The transmit power of the ith antenna on the hth antenna unit is P_{hi}. The total transmit power of the entire DAS is $P = \sum_{h=1,i=1}^{N_u,N_t} P_{hi}$. We assume that the room is an isolated system with no interferences from outside. This assumption holds because the penetration loss of the THz wave is extremely high.

We first consider the scenario that one user has one antenna. For the downlink channel, the link between one transmit antenna and one receive antenna is shown by (5.2). Note that in the THz band, both N_c and N_s are very small. The multi-input-single-output (MISO) channel matrix has the following form

$$\mathbf{H} = [\sum_{i=1}^{N_c*N_s} \beta_{1i}\mathbf{e}_t^*(\Omega_{1i}), ..., \sum_{i=1}^{N_c*N_s} \beta_{ni}\mathbf{e}_t^*(\Omega_{ni}), ..., \sum_{i=1}^{N_c*N_s} \beta_{N_u i}\mathbf{e}_t^*(\Omega_{N_u i})], \tag{5.3}$$

where β_{ni} is the complex gain of the ith path between the receiver and the nth antenna unit, $\mathbf{e}_t(\Omega_{ni})$ is the transmit array response vector [9, p.349], and $\mathbf{X}^*$ is the conjugate transpose of $\mathbf{X}$. The dimension of $\mathbf{H}$ is $1 \times N_u N_t$.

When the user has N_r antennas on the device, the MIMO channel matrix has the following expression

$$\begin{aligned}\mathbf{H} = [&\sum_{i=1}^{N_c * N_s} \beta_{1i}\mathbf{e}_r(\Omega_{1i})\mathbf{e}_t^*(\Omega_{1i}), ..., \sum_{i=1}^{N_c * N_s} \beta_{ni}\mathbf{e}_r(\Omega_{ni})\mathbf{e}_t^*(\Omega_{ni}), ..., \\ &\sum_{i=1}^{N_c * N_s} \beta_{N_u i}\mathbf{e}_r(\Omega_{N_u i})\mathbf{e}_t^*(\Omega_{N_u i})],\end{aligned} \tag{5.4}$$

where $\mathbf{e}_r(\Omega_{ni})$ is the receive array response vectors. $\mathbf{H}$ is a matrix with a dimension of $N_r \times N_u N_t$. As N_c and N_s are very small numbers, columns of $\mathbf{H}$ in Equ. (5.4) are highly correlated, which makes $\mathbf{H}$ a very ill-conditioned matrix.

5.4.3 DAS with Graphene Based Antenans

Graphene can be used as a novel material for THz antennas. Due to its special electrical properties, the size of graphene based antennas is much smaller than that of metallic antennas. Research on graphene based antennas shows that they are 50 times smaller than traditional antennas, thus we can place significantly more graphene based antennas on one AU.

Suppose we place N_g graphene based antennas on one AU, which occupy the space of a single metallic antenna (for ULA). In Fig. 5.1, each antenna is replaced with N_g (can be up to 50) graphene based antennas, thus there are effectively $N_u N_t N_g$ antennas at the base station. Therefore, even for a very small space, we can place hundreds or even thousands of antennas on the base station. Unlike the traditional massive MIMO in the GHz range, which assume that all antennas are critically spaced and have no correlation, the graphene based antennas in our system are quite close (N_g antennas in one wavelength) and have very high correlation. However, we can still obtain benefits by dividing one antenna into several antennas for several reasons. One is that more antennas can bring some multiplexing gains, although not too much when the channel is sparse. Another reason is that it is quite easy to modulate graphene based anntennas. By simply applying a bias voltage, the phase shift of one graphene antenna is changed. Thus, we can obtain very high beamforming gain with large numbers of antennas (see Section 2.5).

In order to reduce the hardware complexity, we would like to use as few RF chains as possible. One promising way to solve this problem is to do hybrid precoding, as shown in [85]. In our scheme, we have N_u RF chains in the central unit which are connected to N_u distributed antenna units, and the number of data streams equals the number of RF chains. We use a traditional precoding scheme in the baseband and phase shifters in the RF. That means for all the AUs, we have N_u RF chains to process the data in the baseband. For each AU, we use a phase shift to process the data. By doing this, we can obtain the benefit of beamforming without too many RF chains or complex structures. The received signal is

$$\mathbf{y} = \mathbf{H}\mathbf{F}_{RF}\mathbf{F}_{BB}\mathbf{s} + \mathbf{n}, \tag{5.5}$$

where $\mathbf{y}$ is the $N_r \times 1$ received vector, $\mathbf{F}_{BB}$ is the $(N_c \cdot N_s) \times N_c$ baseband precoder, $\mathbf{F}_{RF}$is the $(N_c \cdot N_s) \times (N_c \cdot N_s)$ RF precoder, and $\mathbf{n}$ is the Gaussian noise vector.

5.5 The Performance Analysis of the DAS in the THz Band

5.5.1 The Universal DAS Capacity

When there is only one receive antenna, as the rank of $\mathbf{H}$ is only one, there are only diversity and beamforming gains to the capacity. The capacity of this MISO system is

$$C = \mathbf{E}[\log_2(\mathbf{I} + \frac{\sum_i P_i h_i}{\sigma_0^2})] \text{ b/s/Hz}, \tag{5.6}$$

where $\mathbf{E}[\cdot]$ is the expectation, P_i is the transmit power of the ith stream, h_i is the ith element of $\mathbf{H}$, and N_0 is the noise power spectral density. In this situation, more transmit antennas in the DAS can guarantee the received power at the receiver.

When there are N_r receive antennas, the ergodic MIMO capacity is given by the following well-known formula [9, p.400]

$$C = \mathbf{E}[\log_2 \det(1 + \frac{P_i \mathbf{H}\mathbf{H}^*}{\sigma_0^2})] \text{ b/s/Hz}, \tag{5.7}$$

where the asterisk denotes conjugate transpose.

Equ. (5.6) and (5.7) are two universal MIMO capacity formulas, regardless of the channel condition and the frequency band. In the case of an environment with rich scatters, the columns of the channel matrix $\mathbf{H}$ are modeled as zero-mean, independent and identically distributed random variables. In the next section, we

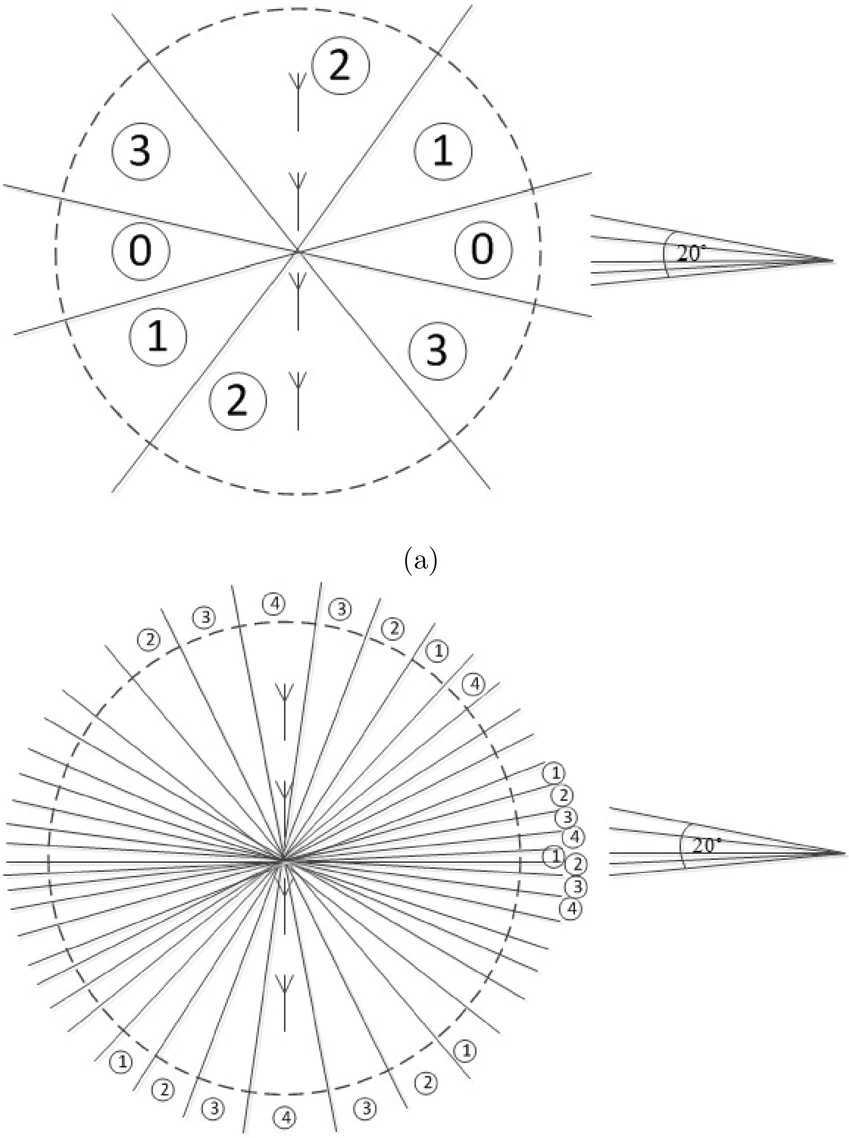

(a)

(b)

Figure 5.2: (a) When antennas are critical spaced and the angular spread is narrow, all the sub rays in one cluster will fall into one angular window. (b) When the antennas are sparsely spaced, each angular window is very narrow, thus the sub rays in one cluster can fall in several angular windows.

will analyze the THz DAS capacity considering the particular characteristics of the THz channel.

5.5.2 The Number of Degrees of Freedom in THz DAS

The model of the DAS MIMO channel can be regarded as a traditional MIMO system, except that the separation between antenna units are large. We consider a MIMO system with N_t transmit antennas. Let the normalized length of the antenna array be $L_r = N_t\triangle$, where $\triangle$ is the antenna separation normalized to the wavelength. For traditional MIMO, all the antennas are evenly spaced on a device and usually have separations of half a wavelength ($\triangle = \frac{1}{2}$). For the DAS, if considering the extreme case that each DAU has only one antenna, antenna separations are much greater than the wavelength ($\triangle \gg \frac{1}{2}$). Theoretically, the antenna array can divide the entire space into L_r parts, each with a cosine width of $2/L_r$. With such an array, two signals from angle differences larger than $2/L_r$ can be seperated.

As elaborated from Fig. 5.2, for traditional MIMO systems, as all antennas are critically spaced (with a separation of $\frac{1}{2}\lambda$) in an array, one bin has only two angular windows of paths (angle windows with the same index belong to the same bin). As shown in Fig. 5.2 (a), the entire space is divided into eight windows of paths by four antennas. Signals departing from/arriving at the same window cannot be resolved. For a very narrow cluster of sub rays, they are treated as one bin as they are likely in the same window. In the meanwhile, when the antennas are sparsely spaced on an array, each bin contains several angular windows of paths. Although for the same number of antennas, the width of each bin remains the same regardless of how sparse the array is, the narrow clusters of sub rays are likely in several different windows. In the THz band, the number of clusters are usually very few and the width of each cluster is very narrow. In this situation, the array with sparse separation makes it much different from that with critical separation. For a critically spaced array, all the sub rays in one narrow cluster can be confined in one bin. While for a sparsely spaced array, more bins can have sub rays, as can be seen in Fig. 5.2 (b).

In [85], the authors use a Laplacian distribution to fit the angles of the sub rays in one cluster. Mathematically, the angles of sub rays in the cluster has a probability density function of

$$f(x) = \frac{1}{2b}\exp(-\frac{|x-\mu|}{b}), \tag{5.8}$$

where μ is the cluster angle and b is the angular spread. As mentioned in [68], the angles of all the clusters are uniformly distributed in the space. Therefore, the relationship between the number of multipaths and the degrees of freedom can be calculated as below.

For the angle spread range, suppose there are $N_b = 4L_r$ angle windows. For the first sub ray, the probability to be in window i is

$$P(i) = \int_{\theta_{i-1}}^{\theta_i} \frac{1}{2b} \exp(-\frac{|x-\mu|}{b}). \tag{5.9}$$

where θ_i is the boundary between window i and $i+1$.

For the remaining sub rays, each has the same probability as the first one. Therefore, the number of occupied windows by all N_s sub-rays is the number of degrees of freedom. Note that in the above model, for discussion simplicity, we assume the width of one cluster is the same as the width of N_r angular windows. The theory is the same when these two angles are different. Obviously, when all the antennas are critically spaced, all the sub rays in one cluster are in one or two bins, which results in lower multiplexing gain.

When the number of transmitting antennas is larger than the number of receiving antennas, by precoding, we can obtain a power gain of n_t/n_r. The capacity is

$$C = \mathbf{E}[\log_2 \det(1 + \frac{P\mathbf{H}\mathbf{H}^*}{n_r \sigma_0^2})] \text{ b/s/Hz}. \tag{5.10}$$

When graphene based antennas are used, we can pack several tens times of more antennas on the transmit array. We only use Nu RF chains on the central unit and all other units only have antennas. Before one RF chain sending signal to antennas, we use phase shifters to change the phase for each antenna. We use fewer RF chains, thus the precoding scheme has a low complexity and the performance can be near optimal.

5.5.3 Antenna Selection for the DAS

Suppose we choose some of the antennas from each unit and form a new transmit antenna array with fewer antennas than before. The new antenna array has a much larger antenna separation. The best antenna selection scheme can use fewer antennas and RF chains without impairing the performance too much. Once we get the entire channel matrix, the best antenna selection scheme can be obtained by the following problem.

$$\begin{aligned} \underset{P_i, N_i}{\text{maximize}} \quad & C = \log_2 \det(1 + \frac{P_i}{\sigma_n^2}\mathbf{H}\mathbf{R}\mathbf{R}^*\mathbf{H}^*) \text{ b/s/Hz}, \\ \text{subject to} \quad & \sum_{i=1}^{N_t} P_i < P, \\ & \sum_{i=1}^{N_u} N_i \leq N_t, \end{aligned} \tag{5.11}$$

where diagonal matrix $\mathbf{R}$ is the antenna selection matrix. There are N_t non-zero diagonal values in $\mathbf{R}$ and all other values are zero.

The antenna selection scheme shown in (5.11) is the optimal selection algorithm, which has a high computational complexity. Several low complexity algorithms have been proposed. For example, the norm based selection method selects the group of antennas with the largest receiving power, the correlation based selection algorithm considers the correlation between the columns of the channel matrix. In [86], a new low complexity method is proposed. The first antenna is the one with the largest norm, and the next antenna is the one with a high channel gain and maximum level of uncorrelation with the previously selected antennas. In the future work, we will examine the performance of antenna selection in the THz with a suboptimal selection scheme.

From the above discussion, we can figure out the potential advantages of DAS in the THz band:

- DAS can increase the separation between antennas by allocating antenna arrays to different physical locations. Such an extremely large separation (compared to the wavelength) is essential to the capacity of the MIMO system, as the spatial correlation between antennas is severe in the THz due to the lack of scatterings.

- When there are many blockages, DAS can provide diversity gain to the system. As THz waves have a low penetration ability and fewer multipaths, the link is more likely to be blocked than in the GHz band.

- Adopting antenna selection, we can use less RF chains to achieve a high capacity. As for THz DAS, the correlation between AUs is very small, but the correlation between antennas on the same AU is relatively large, we can infer that antenna selection is more necessary in the THz band.

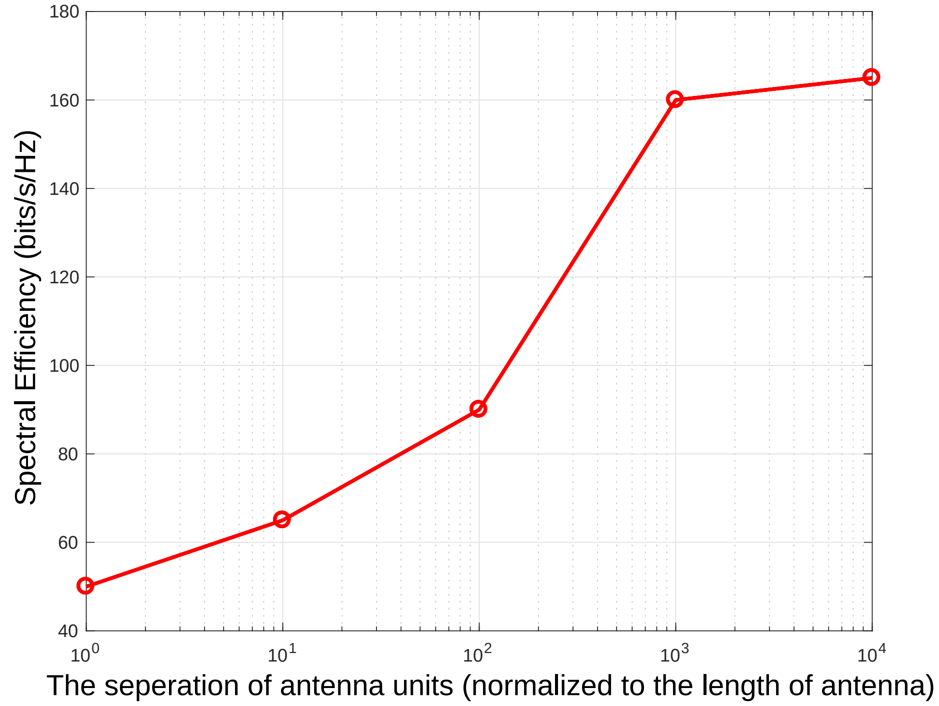

Figure 5.3: Spectral efficiency of $8 \times 8 \times 64$ MIMO versus separations of antenna units.

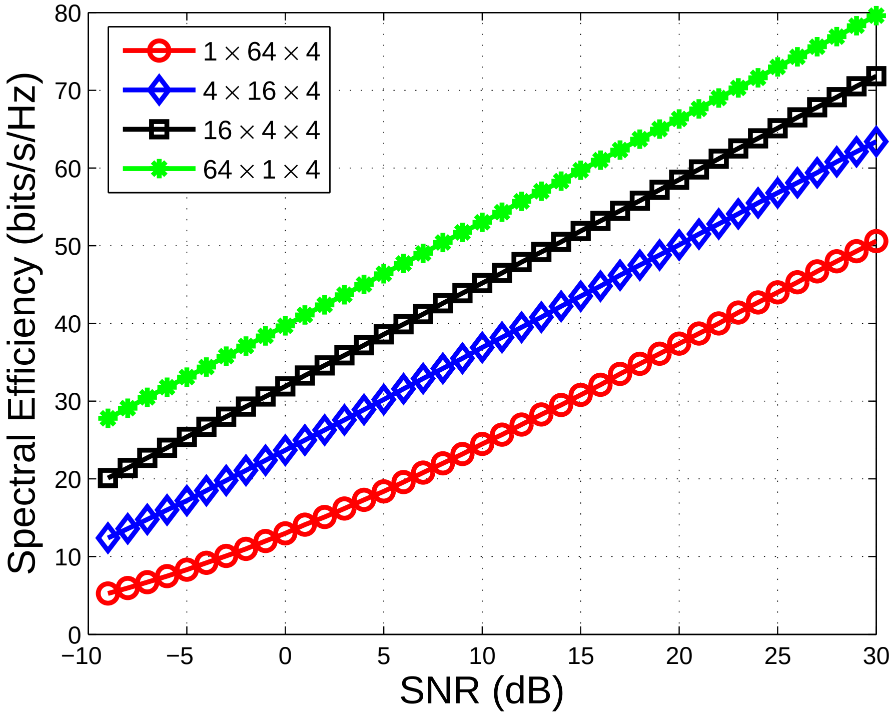

Figure 5.4: Spectral efficiency of 64×4 MIMO with different DAS configuration.

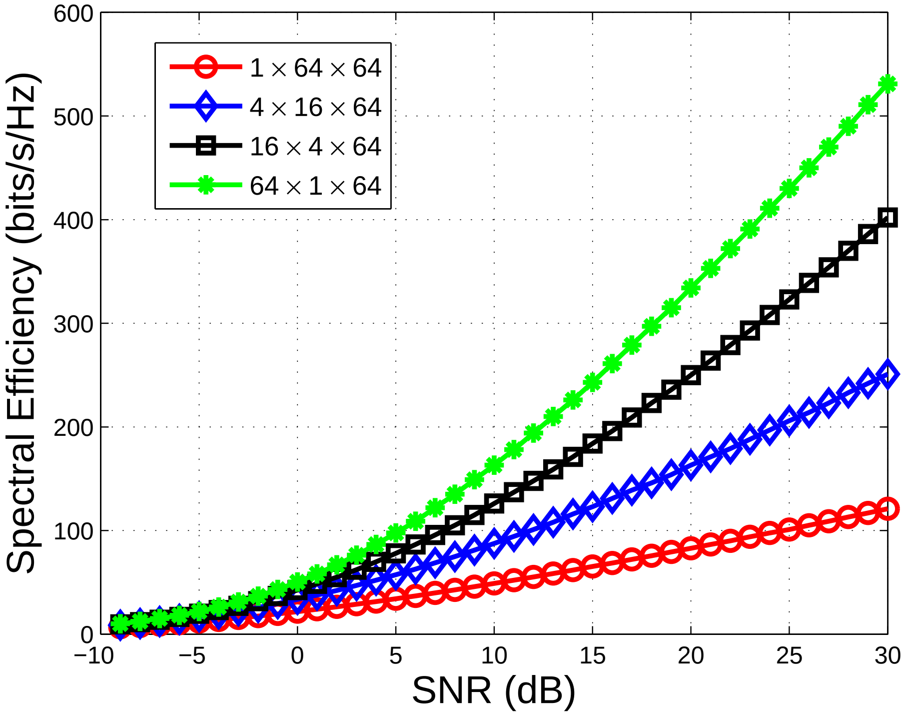

Figure 5.5: Spectral efficiency of 64 × 64 MIMO with different DAS configuration.

5.6 Simulation Results of the THz DAS

We first examine the effect of antenna separations on the capacity of MIMO systems. We set the number of antenna units as eight with eigth antennas on each unit. Antenna unit separations are 1 to 10000 times of the wavelength. The antenna separation on each unit is half a wavelength. We assume that there are four clusters and four sub-rays in each cluster. The sub-rays' spread in each cluster is 7.5°. In order to fully obtain all the degrees of freedom, we set the number of receive antennas the same as the number of transmit antennas. See Table 5.1 for simulation parameters and assumption details.

The number of degrees of freedom is shown in Table 5.2. As can be seen from this table, the number of degrees of freedom is larger when the antenna separation is large, which implies that the effect on multiplexing gain of distributed antennas is larger. Note that when the antenna unit separation is half a wavelength (0.5), it is the result of a conventional antenna system (CAS). When the antenna unit separation is larger than 1000 times of the wavelength (for 1 THz wave, 1000 times of the wavelength is about 0.3 m which is quite easy to implement in DAS), the number of degrees of freedom does not increase too much with the increase of the antenna unit separation, which means that DAS can easily obtain its full benefits

Table 5.1: Simulation Parameters

Parameters	Setting
Transmit/Reveive antenna form	uniform linear array
Number of units	8
Number of transmit antennas in a unit	8
Number of receivers	64
Cell radius	10 m
Number of clusters	4
Number of rays in a cluster	4
Azimuth angle width of the transmitter	60°
Elevation angle width of the transmitter	20°
Azimuth angle width of the receiver	360°
Elevation angle width of the reciever	360°
Elevation/azimuth angle spread	7.5°
Received SNR	10 dB

without very large antenna unit separations. The effect of antenna separation on the capacity is shown in Fig. 5.3. We assume that all the antennas have the same power and the signal-to-noise ratio is defined as **SNR** = 10 dB. The capacity has the same trend of the number of degrees of freedom. Table 5.2 and Fig. 5.3 indicate that large antenna separations can improve the MIMO capacity.

Table 5.2: Number of degrees of freedom

Unit separation	1	10	100	1000	2000
Number of degrees of freedom	10	14	22	40	42

Next we compare the performance of the DAS and CAS. The system setup is the same as in Fig. 5.3. For DAS, N transmit antennas are grouped into N_u antenna units and each has $N_t = N/N_u$ antennas. For CAS, all the N transmit antenna are built on one device which is a special case of DAS. Fig. 5.4 shows the capacity of the MIMO system with 64 transmit antennas. The circle line shows the performance of the CAS ($N_u \times N_t \times N_r = 1 \times 64 \times 4$), the diamond line shows the capacity of the DAS with $4 \times 16 \times 4$, the square line shows the capacity of a $16 \times 4 \times 4$ MIMO system, and the asterisk line shows the capacity of a $64 \times 1 \times 4$ MIMO system. It indicates that when receive antennas are few, the capacity does not increase much. For example, when the SNR is 30 dB, the capacity of 64 antennas on 64 units outperforms the capacity of 64 antennas on one unit by only 60 percent. When there are 64 receive antennas, the performance is shown in Fig. 5.5. The four lines have the same meaning as those in Fig. 5.4. Unlike the capacity in Fig. 5.4, more antenna units can introduce high system capacity. There are several reasons for this difference.

When all the antennas are located in one place, the rank of the channel matrix **H** is no more than the number of multipaths. As the number of multipaths is very small in the THz band, the capacity of CAS is not high in this situation, no matter how large the MIMO scale is. When the units are separated physically in different locations, the number of multipaths is artificially increased. The more the units and the antennas separate, the more multipaths exist between the transmitter and the receiver. Ideally, each unit has one antenna and all the units randomly distributed in the entire space can introduce the maximum capacity. These two figures verify our aforementioned analysis.

5.7 Conclusion

In this chapter, a distributed antenna system model in the THz band is proposed. We have provided theoretical analysis of the channel capacity of DAS. From the results, we can conclude that the channel is very sparse if the number of antennas on the base station is very large. Also, DAS can have larger numbers of degrees of freedom than CAS. Due to the particular characteristics of THz channels, increasing the number of antenna units has more obvious benefits than increasing the number of antennas on one antenna unit. Besides, we have proposed an antenna selection and precoding scheme, which has a very low complexity.

Chapter 6

Conclusions and Further Research Issues

In this dissertation, we have investigated nano device designs, channel modeling with reconfigurable antennas and rough reflection surfaces, and distributed antenna system in THz bands. The conclusions are drawn as follows:

- **Design of THz Devices**

  We have proposed some graphene-based devices for wireless communications. First, the characteristics of graphene is introduced. Based on the unique properties, three devices have been proposed: the CNT-based bundled antenna, the graphene-based directional antenna and the graphene-based molecule receiver. The SWCNT bundled antenna has many distinctive characteristics because of its unique electrical properties. We have studied the characteristics of SWCNTs and SWCNT bundled antennas and analysed the spectral efficiency of MIMO systems based on SWCNT bundled dipole antennas. There is a trade-off between the efficiency of antennas and the number of antennas as a function of bundle size. Under different scenarios, there exists an optimal bundle size which maximizes spectral efficiency. We showed that, for short range communications, the SWCNT bundled antenna based MIMO system has a higher spectral efficiency than ideal metallic antennas based MIMO systems. Furthermore, we investigated the effect of non-uniform bundle size in the fabrication process and showed that such variation can reduce spectral efficiency. For the graphene-based directional antenna, the dimension is much smaller than metallic antennas with the same resonance frequency. The dynamic range can be 80°, and the directional gain can be over 10 dB. Besides, the antenna is reconfigurable and the pattern can be easily controlled by the bias voltage. A graphene-based molecule receiver has a very high sensitivity. We have proposed a simple and efficient detection method for the molecule receiver based on the graphene, which can not only enlarge the communication range, but also has a low complexity. For different kinds of transmit signals (impulse signals and rectangular signals), we have obtained the corresponding curves of the current change. By doing this, we change the molecule concentration into electrical signals, which have well studied algorithms to process. The results show that the delay is about 10 s and the maximum current change is over 20%. The performance of the MC system is also analyzed in this chapter. Numerical results show that the high sensitivity can increase the data rate considerably.

Future work in this direction might be focused on fabricating the high quality graphene and studying the interactions between molecules and the graphene. Thus, a closed-form transfer function may eliminate the variations in the model. Moreover, more sensitive graphene with short response time may be realized in academic and industrial fields which can promote the communication distance up to 1 mm and reduce the delay.

- **Reconfigurable MIMO System in the Terahertz Band**

  We have proposed a reconfigurable MIMO antenna system based on graphene for THz communication with rough surfaces. First, the effect of the roughness factor is analyzed. We revealed that there are many scattered links between the transmitter and the receiver besides the specular rays if the reflection surfaces are very rough. Then, we have designed a reconfigurable directional antenna with graphene. The antenna has a small size and a high directional gain and can be easily controlled by a bias voltage. Finally, we have evaluated the performance of MIMO systems with directional antennas. We have shown that the antenna separation can be smaller than half a wavelength if we use directional antennas in a roughness environment. The results show that the proposed MIMO system has a higher spectral efficiency than the traditional MIMO systems with omnidirectional metallic antennas. By using the water-filling power allocation scheme, the spectral efficiency increases to an even higher level. The main difficulty in our model is solving the optimization problem considering the limited computing ability of the devices. Therefore, a sub-optimal solution has been mentioned as a supplement to the optimal one. The tradeoff between complexity and accuracy has also been considered in our work.

- **A Statistical Model for the MIMO Channel with Rough Reflection Surfaces in the THz Band**

  We have studied the effect of rough surfaces to THz MIMO systems. The relationship between specular capacity and scattered capacity is analyzed, as well as the optimal precoding scheme and smart antenna design for massive MIMO. A new MIMO system model for THz and nanocommunications is proposed that includes the effects of rough reflection surfaces. The results show that the MIMO channel in the THz band is very sparse if the reflecting surfaces are ideally smooth, and that with the increase of the MIMO scale, the sparsity becomes even more severe. When the surfaces are rough, the spectral efficiency of the MIMO system is higher than that with smooth surfaces, which is more pronounced with a larger MIMO scale. We show that surface roughness has a positive effect on increasing the spectral efficiency. Finally, numerical results on the performance of different MIMO scales reveal when it is necessary to use a large MIMO scale in the THz band. We hope that the results presented in this chapter will aid future implementations of nanocommunication systems.

- **Performance of Distributed Antenna Systems in the THz Band for Indoor Communications**

  We have proposed a distributed antenna system model in the THz band. We have provided theoretical analysis of the channel capacity of DAS. From the results, we can conclude that the channel is very sparse if the number of antennas on the base station is very large. Also, DAS can have a larger number of degrees of freedom than CAS. Due to the particular characteristics of THz channels, increasing the number of antenna units has more obvious benefits than increasing the number of antennas in one antenna unit. Besides, we have proposed an antenna selection and precoding scheme, which has a very low complexity.

Publications

Published papers:

Z. Xu, X. Dong, and J. Bornemann, “Spectral efficiency of carbon nanotube antenna based MIMO systems in the terahertz band”, *IEEE Wireless Communications Letters*, vol. 2, no. 6, pp. 631–634, December 2013.

Z. Xu, X. Dong, and J. Bornemann , “Design of a reconfigurable MIMO system for THz communications based on graphene antennas”, *IEEE Transaction on Terahertz Science and Technology*, vol. 4, no. 5, pp. 609–617, September 2014.

Z. Xu, X. Dong, and J. Bornemann , “A statistical model for the MIMO channel with rough reflection surfaces in the THz band”, *Nano Communication Networks*, vol. 8, pp. 25–34, 2016.

Bibliography

[1] J. J. Plombon, K. P. O'Brien, F. Gstrein, V. M. Dubin, and Y. Jiao, "High-frequency electrical properties of individual and bundled carbon nanotubes," *Appl. Phys. Lett.*, p. 063106, Feb. 2007.

[2] H. J. Yoon, D. H. Jun, J. H. Yang, Z. Zhou, S. S. Yang, and M. M. Cheng, "Carbon dioxide gas sensor using a graphene sheet," *Sens. and Actuators B: Chem.*, vol. 157, pp. 310–313, Mar. 2011.

[3] P. Beckmann and A. Spizzichino, *The scattering of electromagnetic waves from rough surfaces.* New York, USA: The Macmillan Company, 1963.

[4] S. Priebe, M. Jacob, C. Jansen, and T. Kurner, "Non-specular scattering modeling for THz propagation simulations," *in Proc. 5th EuCAP*, pp. 1–5, Apr. 2011.

[5] R. Piesiewicz, C. Jansen, D. Mittleman, T. K. Ostmann, M. Koch, and T. Kurner, "Scattering analysis for the modeling of THz communication systems," *IEEE Trans. Antennas Propag.*, vol. 55, pp. 3002–3009, Nov. 2007.

[6] M. Dragoman, A. A. Muller, D. Dragoman, F. Coccetti, and R. Plana, "Terahertz antenna based on graphene," *J. Appl. Phys.*, vol. 107, p. 104313, 2010.

[7] Y. Huang, L. Wu, M. Tang, and J. Mao, "Design of a beam reconfigurable THz antenna with graphene-based switchable high-impedance surface," *IEEE Trans. Nanotechnol.*, vol. 11, pp. 836–842, July 2012.

[8] C. Jansen, S. Priebe, C. Moller, M. Jacob, H. Dierke, M. Koch, and T. Kurner, "Diffuse scattering from rough surfaces in THz communication channels," *IEEE Trans. Terahertz Sci. Technol.*, vol. 1, pp. 462–472, Nov. 2011.

[9] D. Tse and P. Viswanath, *Fundamentals of Wireless Communication.* Cambridge, U.K.: Cambridge Univ. Press, 2005.

[10] I. F. Akyildiz, J. M. Jornet, and C. Han, “Terahertz band: next frontier for wireless communications,” *Phycical Commun.*, vol. 12, pp. 16–32, Sep. 2014.

[11] R. Piesiewicz, M. Jacob, M. Koch, J. Schoebel, and T. Kurner, “Performance analysis of future multigigabit wireless communication systems at THz frequencies with highly directive antennas in realistic indoor environments,” *IEEE J. Sel. Topics in Quantum Electron.*, vol. 14, pp. 421–430, Mar. 2008.

[12] S. Priebe, C. Jastrow, M. Jacob, T. K. Ostmann, T. Schrader, and T. Kurner, “Channel and propagation measurements at 300 GHz,” *IEEE Trans. Antennas Propag.*, vol. 59, pp. 1688–1698, May 2011.

[13] S. Priebe, M. Jacob, and T. Kurner, “AoA, AoD and ToA characteristics of scattered multipath clusters for THz indoor channel modeling,” *European Wireless*, pp. 188–196, Apr. 2011.

[14] A. Sayeed and V. Raghavan, “Maximizing MIMO capacity in sparse multipath with reconfigurable antenna arrays,” *IEEE J. Special Topics in Sig. Proc.*, vol. 1, no. 1, pp. 156–166, June 2007.

[15] V. Raghavan, G. Hariharan, and A. Sayeed, “Capacity of sparse multipath channels in the ultrawideband regime,” *IEEE J. Special Topics in Sig. Proc.*, vol. 1, no. 5, pp. 357–371, Oct. 2007.

[16] W. Weichselberger, M. Herdin, H. Ozcelik, and E. Bonek, “A stochastic MIMO channel model with joint correlation of both link ends,” *IEEE Trans. Wirel. Commun.*, vol. 5, no. 1, pp. 90–100, Jan. 2006.

[17] K. S. Novoselov, A. K. Geim, S. V. Morozov, D. Jiang, Y. Zhang, S. V. Dubonos, I. V. Grigorieva, and A. A. Firsov, “Electric field effect in atomically thin carbon films,” *Science*, vol. 306, pp. 666–669, Oct. 2004.

[18] Y. M. Lin, C. Dimitrakopoulos, K. A. Jenkins, D. B. Farmer, H. Y. Chiu, A. Grill, and P. Avouris, “100-GHz transistors from wafer-scale epitaxial graphene,” *Science*, vol. 327, pp. 662–662, Feb. 2010.

[19] R. Murali, K. Brenner, Y. Yang, T. Beck, and J. D. Meindl, “Resistivity of graphene nanoribbon interconnects,” *IEEE Electon Device Lett.*, vol. 30, pp. 611–613, June 2009.

[20] K. I. Bolotin, K. J. Sikes, Z. Jiang, M. Klima, G. Fudenberg, J. Hone, P. Kim, and H. L. Stormer, “Ultrahigh electron mobility in suspended graphene,” *Solid State Commun.*, vol. 146, pp. 351–355, June 2008.

[21] X. Du, I. Skachko, A. Barker, and E. Y. Andrei, “Approaching ballistic transport in suspended graphene,” *Nat. Nanotechnol.*, vol. 3, pp. 491–495, Aug. 2009.

[22] F. Schedin, A. K. Geim, S. V. Morozov, E. W. Will, P. Blake, M. I. Katsnelson, and K. S. Novoselov, “Detection of individual gas molecules absorbed on graphene,” *Nature Materials*, vol. 6, pp. 652–655, Sep. 2007.

[23] I. Llatser, C. Kremers, D. N. Chigrin, J. M. Jornet, M. C. Lemme, A. C. Aparicio, and E. Alarcon, “Characterization of graphene-based nano-antennas in the terahertz band,” *in Proc. 6th EuCAP*, pp. 194–198, 2012.

[24] J. M. Jornet and I. F. Akyildiz, “Graphene-based nano-antennas for electromagnetic nanocommunications in the terahertz band,” *in Proc. 4th EuCAP*, pp. 1–5, Apr. 2010.

[25] I. Llatser, C. Kremers, A. C. Aparicio, J. M. Jornet, E. Alarcon, and D. N. Chigrin, “Graphene-based nano-patch antenna for terahertz radiation,” *Photon Nanostruct: Fundam Appl.*, vol. 4, pp. 353–358, 2012.

[26] M. Tamagnone, J. S. Gomez-Diaz, J. R. Mosig, and J. Perruisseau-Carrier, “Reconfigurable terahertz plasmonic antenna concept using a graphene stack,” *Appl. Phys. Lett.*, p. 214102, 2012.

[27] P. J. Burke, S. Li, and Z. Yu, “Quantitative theory of nanowire and nanotube antenna performance,” *IEEE Trans. Nanotechnol.*, pp. 314–334, July 2006.

[28] C. Rutherglen and P. Burke, “Nanoelectromagnetics : Circuit and electromagnetic properties of carbon nanotubes,” *Small*, pp. 884–906, Apr. 2009.

[29] Y. Huang, W. Yin, and Q. Liu, “Performance prediction of carbon nanotube bundle dipole antennas,” *IEEE Trans. Nanotechnol.*, pp. 331–337, May 2008.

[30] G. W. Hanson, “Fundamental transmitting properties of carbon nanotube antennas,” *IEEE Trans. Antennas Propag.*, pp. 3426–3435, Nov. 2005.

[31] M. Pierobon and I. F. Akyildiz, “A physical end-to-end model for molecular communication in nanonetworks,” *IEEE J. Sel. Areas Comm.*, vol. 28, pp. 602–611, May 2010.

[32] L. P. Gine and I. F. Akyildiz, “Molecular communication options for long range nanonetworks,” *Comput. Netw.*, vol. 53, pp. 2753–2766, Aug. 2009.

[33] D. Arifler, “Capacity analysis of a diffusion-based short-range molecular nano-communication channel,” *Comput. Netw.*, vol. 55, pp. 1426–1434, Apr. 2011.

[34] M. Pierobon and I. F. Akyildiz, “Capacity of a diffusion-based molecular communication system with channel memory and molecular noise,” *IEEE Trans. Inf. Theory*, vol. 59, pp. 942–954, Feb. 2013.

[35] I. Llatser, A. C. Aparicio, M. Pierobon, and E. Alarcon, “Detection techniques for diffusion-based molecular communication,” *IEEE J. Sel. Areas Comm.*, vol. 31, pp. 726–734, Dec. 2013.

[36] I. S. Gregory, C. Baker, W. R. Tribe, I. V. Bradley, M. J. Evans, E. H. Linfield, A. G. Davies, and M. Missous, “ Optimization of photomixers and antennas for continuous-wave terahertz emission,” *IEEE J. Quantum Electron.*, vol. 41, pp. 717–728, may 2005.

[37] G. Georgiou, H. K. Tyagi, P. Mulder, G. J. Bauhuis, J. J. Schermer, and J. G. Rivas, “Photo-generated THz antennas,” *Sci. Rep.*, p. 3584, Jan. 2014.

[38] I. F. Akyildiz, F. Brunetti, and C. Blazquez, “Nanonetworks: A new communication paradigm,” *Computer Netw.*, vol. 52, pp. 2260–2279, Apr. 2008.

[39] P. J. Burke, “An RF circuit model for carbon nanotubes,” *IEEE Trans. Nanotechnol.*, pp. 55–58, Mar. 2003.

[40] Y. Tu, Z. P. Huang, D. Z. Wang, J. G. Wen, and Z. F. Ren, “Growth of alignd carbon nanotubes with controlled site density,” *Appl. Phys. Lett.*, pp. 4018–4020, May 2002.

[41] H. Q. Ngo, E. G. Larsson, and T. L. Marzetta, “Energy and spectral efficiency of very large multiuser MIMO systems,” *IEEE Trans. Commun.*, vol. 61, pp. 1436–1449, Apr. 2013.

[42] J. M. Jornet and I. F. Akyildiz, “Channel modeling and capacity analysis for electromagnetic wireless nanonetworks in the Terahertz band,” *IEEE Trans. Wireless Commun.*, vol. 10, pp. 3211–3221, Oct. 2011.

[43] D. Correas-Serrano, J. S. Gomez-Diaz, and A. Alvarez-Melcon, “On the influence of spatial dispersion on the performance of graphene-based plasmonic devices,” *IEEE Trans. Antennas Wirel. Propag. Lett.*, vol. 13, pp. 345–348, feb 2014.

[44] G. Lovat, G. W. Hanson, R. Araneo, and P. Burghignoli, “Semiclassical spatially dispersive intraband conductivity tensor and quantum capacitance of graphene,” *Phys. Rev. B*, vol. 87, p. 115429, 2013.

[45] V. P. Gusynin, S. G. Sharapov, and J. P. Carbotte, “Magneto-optical conductivity in graphene,” *J. Phys.: Cond. Matter*, vol. 19, p. 026222, 2007.

[46] G. W. Hanson, “Dyadic green’s function and guided surface waves for a surface conductivity model of graphene,” *J. Appl. Phys.*, vol. 103, p. 064302, 2008.

[47] A. Y. Nikitin, F. Guinea, F. J. Garca-Vidal, and L. Martn-Moreno, “Edge and waveguide terahertz surface plasmon modes in graphene microribbons,” *Phys. Rev. B*, vol. 84, p. 161407, 2011.

[48] J. S. Gomez-Diaz, M. Esquius-Morote, and J. Perruisseau-Carrier, “Plane wave excitation-detection of non-resonant plasmons along finite-width graphene strips,” *Opt. Express*, vol. 21, p. 24856, Oct. 2013.

[49] K. S. Kim, Y. Zhao, H. Jang, S. Y. Lee, J. M. Kim, K. S. Kin, J. H. Ahn, P. Kim, J. Y. Choi, and B. H. Hong, “Large-scale pattern growth of graphene films for stretchable transparent electrodes,” *Nature*, vol. 457, pp. 706–710, Feb. 2009.

[50] P. Chen and A. Alu, “A terahertz photomixer based on plasmonic nanoantennas coupled to a graphene emitter,” *Nanotechnology*, vol. 24, p. 455202, 2013.

[51] T. Otsuji, T. Watanabe, S. A. B. Tombet, A. Satou, W. M. Knap, V. V. Popov, M. Ryzhii, and V. Ryzhii, “Emission and detection of Teraherz radiation using two-dimensional electrons in III-V semiconductors and graphene,” *IEEE Trans. Terahertz Sci. Technol.*, vol. 3, pp. 63–71, Jan. 2013.

[52] J. M. Jornet and I. F. Akyildiz, “Graphene-based plasmonic nano-transceiver for terahertz band communication,” *in Proc. 8th EuCAP*, Apr. 2014.

[53] J. D. Boerman and J. T. Bernhard, “Performance study of pattern reconfigurable antennas in MIMO communication systems,” *IEEE Trans. Antennas Propag.*, vol. 56, pp. 231–236, Jan. 2008.

[54] S. Zhang, G. H. Huff, J. Feng, and J. T. Bernhard, “A pattern refonfigurable microstrip parasitic array,” *IEEE Trans. Antennas Propag.*, vol. 52, pp. 2773–2776, Oct. 2004.

[55] I. F. Akyildiz, F. Brunetti, and C. Blazquez, "Nanonetworks: A new communication paradigm," *Comput. Netw.*, vol. 52, pp. 2260–2279, Apr. 2008.

[56] F. Schedin, A. K. Geim, S. V. Morozov, E. W. Hill, P. Blake, M. I. Katsnelson, and K. S. Novoselov, "Detection of individual gas molecules absorbed on graphene," *Nature*, vol. 6, pp. 652–655, Sep. 2007.

[57] M. A. Meitl, Z. T. Zhu, V. Kumar, K. J. Lee, X. Feng, Y. Y. Huang, I. Adesida, R. G. Nuzzo, and J. A. Rogers, "Transfer printing by kinetic control of adhesion to an elastomeric stamp," *Nat. Mater.*, vol. 5, pp. 33–38, Jan. 2006.

[58] M. J. Allen, V. C. Tung, L. Gomez, Z. Xu, L. Chen, K. S. Nelson, C. Zhou, R. B. Kaner, and Y. Yang, "Soft transfer printing of chemically converted graphene," *Adv. Mater.*, vol. 21, pp. 2098–2102, Mar. 2009.

[59] W. H. Bossert and E. O. Wilson, "The analysis of olfactory communication among animals," *J. Theoret. Biol.*, vol. 5, pp. 443–469, 1963.

[60] D. Piazza and K. R. Dandekar, "Reconfigurable antenna solution for MIMO-OFDM systems," *Electron. Lett.*, vol. 42, pp. 446–447, Apr. 2006.

[61] K. Huang and Z. Wang, "Terahertz terabit wireless communication," *IEEE Microwave Mag.*, pp. 108–116, June 2011.

[62] H. Song and T. Nagatsuma, "Present and future of terahertz communications," *IEEE Trans. Terahertz Sci. Technol.*, vol. 1, pp. 256–263, Sep. 2011.

[63] T. L. Marzetta, "Noncooperative cellular wireless with unlimited numbers of base station antennas," *IEEE Trans. Wireless Commun.*, vol. 9, pp. 3591–3600, Nov. 2010.

[64] Z. Xu, X. Dong, and J. Bornemann, "Spectral efficiency of carbon nanotube antenna based mimo systems in the terahertz band," *IEEE Wireless Commun. Lett.*, vol. 2, pp. 631–634, Dec. 2013.

[65] ——, "Design of a reconfigurable MIMO system for THz communications based on graphene antennas," *IEEE Trans. Terahertz Sci. and Technol.*, vol. 4, pp. 609–617, Sep. 2014.

[66] T. K. Ostmann and T. Nagatsuma, "A review on terahertz communications research," *J. Infrared Milli. Terahz Waves*, pp. 143–171, 2011.

[67] R. Piesiewicz, C. Jansen, D. Mittleman, T. K. Ostmann, M. Koch, and T. Kurner, "Scattering analysis for the modelign of THz communication systems," *IEEE Trans. Antennas Propag.*, vol. 55, pp. 3002–3009, Nov. 2007.

[68] A. Saleh and R. Valenzuela, "A statistical model for indoor multipath propagation," *IEEE J. Sel. Areas Comm.*, vol. SAC-5, no. 2, pp. 128–137, Feb. 1987.

[69] Q. Spencer, M. Rice, B. Jeffs, and M. Jensen, "A statistical model for angle of arrival in indoor multipath propagation," *IEEE Trans. Veh. Tech.*, vol. 3, pp. 1415–1419, 1997.

[70] A. Sayeed, "Deconstructing multiantenna fading channels," *IEEE Trans. Signal Processing*, vol. 50, no. 10, pp. 2563–2579, Oct. 2002.

[71] W. Bajwa, A. Sayeed, and R. Nowak, "Sparse multipath channels: modeling and estimation," *in Proc. 13th IEEE Digital Signal Processing Workshop*, pp. 4–7, Jan. 2009.

[72] M. Matthaiou, A. Sayeed, and J. Nossek, "Sparse multipath MIMO channels: performance implications based on measurement data," *in Proc. IEEE 10th Workshop Signal Process. Adv. Commun.*, pp. 364–368, June 2009.

[73] X. You, D. Wang, B. Sheng, X. Gao, X. Zhao, and M. Chen, "Cooperative distributed antenna systems for mobile communications," *IEEE Wireless Commun.*, vol. 17, pp. 35–43, June 2010.

[74] K. Morita and H. Ohtsuka, "The new generation of wireless communications based on fiber-radio technologies," *IEICE Trans. Commun.*, vol. 9, pp. 1061–1068, Sep. 1993.

[75] K. J. Kerpez, "A radio access system with distributed antennas," *IEICE Trans. Veh. Technol.*, vol. 45, pp. 265–275, May 1996.

[76] H. H. Xia, A. B. Herrera, S. Kim, and F. S. Rico, "A cdma-distributed antenna system for in-building personal communications services," *IEEE J. Sel. Areas Commun.*, vol. 14, pp. 644–650, May 1996.

[77] M. V. Clark, T. M. W. III, L. J. Greenstein, A. J. R. Jr., V. Erceg, and R. S. Roman, "Distributed versus centralized antenna arrays in broadband wireless networks," *in Proc. 2001 IEEE VTC*, pp. 33–37.

[78] L. Dai, S. Zhou, and Y. Yao, "Capacity analysis in CDMA distributed antenna systems," *IEEE Trans. Wireless Commun.*, vol. 4, pp. 2613–2620, Nov. 2005.

[79] H. Zhuang, L. Dai, L. Xiao, and Y. Yao, "Spectral efficiency of distributed antenna systems with random antenna layout," *Electronics Lett.*, vol. 39, pp. 495–496, Mar. 2003.

[80] W. Choi and J. G. Andrews, "Downlink performance and capacity of distributed antenna systems in a multicell environment," *IEEE Trans. Wireless Commun.*, vol. 6, pp. 69–73, Jan. 2007.

[81] J. G. Andrews, W. Choi, , and R. W. Heath, "Overcoming interference in spatial multiplexing MIMO cellular networks," *IEEE Wireless Communi. Magazine*, vol. 14, pp. 95–104, Dec. 2007.

[82] S.-R. Lee, S.-H. Moon, J.-S. Kim, and I. Lee, "Capacity analysis of distributed antenna systems in a composite fading channel," *IEEE Trans. Wireless Commun.*, vol. 11, pp. 1076–1086, May 2012.

[83] L. Dai, "An uplink capacity analysis of the distributed antenna system (das): from cellular das to das with virtual cells," *IEEE Trans. Wireless Commun.*, vol. 11, pp. 2717–2731, May 2014.

[84] H. Zhu, "Performance comparison between distributedantenna and microcellular systems," *IEEE J.Sel. Areas Commun.*, vol. 29, pp. 1151–1163, June 2011.

[85] S. Rajagopal, S. Sbu-Surra, Z. Pi, and R. W. Heath, "Spatially sparse precoding in millimeter wave mimo systems," *IEICE Trans. Wireless Commun.*, vol. 13, pp. 1499–1513, Jan. 2014.

[86] S. Jung and B. W. Kim, "Near optimal low complexity antenna selection scheme for energy efficient correlated distributed MIMO systems," *International J. Electronics Commun.*, vol. 69, pp. 1039–1046, July 2015.